[AMERICAN JOURNAL OF SCIENCE, VOL. 306, MARCH, 2006, P. 135–190]

American Journal of Science

*MARCH 2006*

# MAGic: A PHANEROZOIC MODEL FOR THE GEOCHEMICAL CYCLING OF MAJOR ROCK-FORMING COMPONENTS

ROLF S. ARVIDSON*, FRED T. MACKENZIE** and MICHAEL GUIDRY**

**ABSTRACT. A dynamical model (MAGic) is presented that describes the elemental cycling of sedimentary materials involving sodium, potassium, calcium, magnesium, chloride, carbon, oxygen, iron, sulfur and phosphorous through much of the Phanerozoic. The model incorporates the basic reactions controlling atmospheric carbon dioxide and oxygen concentrations, continental and seafloor weathering of silicate and carbonate rocks, net ecosystem productivity, basalt-seawater exchange reactions, precipitation and diagenesis of chemical sediments and authigenic silicates, oxidation-reduction reactions involving carbon, sulfur, and iron, and subduction-decarbonation reactions. Although MAGic contains feedback and forcing functions adapted from the GEOCARB models (Berner, 1991, 1994; Berner and Kothavala, 2001), these functions are incorporated in a reservoir-reaction scheme that is considerably more detailed. Coupled reservoirs include shallow and deep cratonic silicate and carbonate rocks and sediments, seawater, atmosphere, oceanic sediments and basalts, and the shallow mantle. Model results are reasonably consistent with recently published constraints provided by fluid inclusion, isotopic, floral, and mineralogical records. We have used these results to evaluate sensitivity to uncertainties in the history of the earth-ocean-atmosphere system over the past 500 Ma: the advent of pelagic carbonate sedimentation, the importance of burial versus early diagenetic dolomite formation, the importance of reverse weathering, and the relationship of these processes to seafloor spreading rates. Results include a general pattern of dolomite abundance during periods of elevated seafloor spreading and alkalinity production, elevated atmospheric $CO_2$ concentrations for most of the Phanerozoic similar to those predicted by GEOCARB, and covariance of seawater sulfate to calcium ratios with magnesium to calcium ratios. These trends are broadly consistent with proxies for seawater composition and the mass-age data of the rock record itself.**

## INTRODUCTION

In the early seventies, Garrels and Mackenzie published a model describing the steady state cycling of eleven elements involved in the formation and destruction of sedimentary rocks: Al, C, Ca, Cl, Fe, K, Mg, Na, S, Si, and Ti (Garrels and Mackenzie, 1972). This model, incorporating much of the basic thinking previously set forth in "The Evolution of Sedimentary Rocks" (Garrels and Mackenzie, 1971), derived a steady state mass balance consistent with the observed composition of the atmosphere, ocean, stream, and groundwater reservoirs, as well as the ages and average composition of sedimentary rocks. One of the guiding concepts was the recognition that sediments cycle at different rates and that these differences in renewal or residence time are tied to variations in the probability of post-depositional chemical changes, giving rise to differences in overall bulk composition. They thus distinguished between primary sedimentary materials ("new" rocks of Mesozoic to Cenozoic age with an average renewal time of 150 Ma) and secondary materials ("old"

---

*Department of Earth Science MS-126, Rice University, P.O. Box 1892, Houston, Texas 77251-1892 USA; Rolf.S.Arvidson@rice.edu

**Department of Oceanography, School of Ocean and Earth Science and Technology, University of Hawaii at Manoa, Honolulu, Hawaii 96822 USA

rocks with ages of Paleozoic and older, with an average renewal time of 600 Ma). A basic model result was the tabulation of the residence times for the above elements. The model also showed that on geologic time scales, the oceans as a whole are generally a net heterotrophic system with the sum of aerobic and anaerobic respiration exceeding the gross production of organic carbon (Smith and Mackenzie, 1987; Smith and Hollibaugh, 1997). Garrels and Mackenzie also argued that their assumption of a steady state system was valid, at least for the last ~ 2 Ga of earth history. This steady state could be summarized as (1) the deposition of "new" authigenic, biogenic, and detrital sediments, that thereafter serve as the major source of significant fluxes; (2) the release of dissolved components during early diagenetic stabilization, subsequent burial, uplift and direct weathering. The residues that remain after diagenetic processes have extracted soluble components are stable mineral assemblages composed of quartz, illite, chlorite, dolomite, and evaporites that have avoided dissolution. The subsequent weathering (3) of these "old" materials changes their relative fractions but not their composition. This model was thus secular and cannibalistic, and did not include processes that serve to reconstitute primary igneous crystalline phases and volatile acids (for example, $CO_2$, $SO_2$, HCl, *et cetera*) from sediments, organic matter, and dissolved components. The model presented in this paper, referred to hereafter as MAGic (an acronym denoting the authors, Mackenzie, Arvidson, Guidry interactive cycles), uses Garrels and Mackenzie (1972) as a point of departure, incorporating the improved understanding in geochemical processes and cycling acquired over the subsequent forty years. These processes include the interaction between seawater and oceanic crust, the cycling between oxygen, iron, phosphorous, and organic matter, and the complex feedback relationships between atmospheric $CO_2$, global temperature, terrestrial vegetation, and the rate of chemical weathering.

Because it can take advantage of an improved observational record, MAGic is also less constrained by simplifying assumptions made in Garrels and Mackenzie (1972). For example, the original model assumed that the major ion chemistry of seawater had not varied substantially. Recent work on the chemistry of evaporite fluid inclusions has revealed significant changes in seawater composition (Hardie, 1996; Lowenstein and others, 2001), and MAGic has used these major ion ratio data to provide a reasonable constraint. This has allowed us to tie the basic chemistry of the atmospheric cycles of oxygen and carbon with those of the ocean. In a similar way, the dependencies between carbonate mineral saturation state, atmospheric $CO_2$ tension, and precipitation rate permit analysis of the relationship between seawater chemistry and secular changes in sedimentation. It has also allowed us to compare the relative fluxes of seawater magnesium and potassium in both high temperature (hydrothermal basalt-seawater exchange) and low temperature ("reverse weathering") reactions.

However, we must emphasize that it is not our intention merely to add to the rather large number of existing models. Rather, we wish to refocus attention on the sedimentary rock cycle itself, whose fundamental details have taken a back seat to the compositional history of the oceans (Hardie, 1996; Stanley and Hardie, 1998; Lowenstein and others, 2001; Dickson, 2002; Horita and others, 2002) and the atmosphere (Berner and others, 1983; Berner and Kothavala, 2001; Berner and others, 2003). Because of the complexity inherent in coupling large geochemical systems operating over a wide span of time scales, we have also tried to adhere closely to ideas and approaches that are now generally accepted. MAGic borrows extensively from these approaches, and thus it is in large part an eclectic and synthetic approach. We feel this approach is a useful one given the large number of new proxy data available in increasing resolution and detail (for atmospheric $CO_2$, pH, seawater $Mg^{2+}/Ca^{2+}$ ratio, *et cetera*). In summary, we view a model of this type as an ideal way to investigate the consistency of diverse constraints, fundamental geophysical assumptions (for example, Wallmann, 2001; Rowley, 2002; Rothman, 2002; Shaviv and Veizer, 2003; Hansen and Wallmann, 2003), and current overall understanding. The

TABLE 1

*Weathering Reactions*

Carbonates, per mole cation released

$$CaCO_3 + H_2CO_3 = 2\ HCO_3^- + Ca^{2+} \tag{59}$$

$$CaMg(CO_3)_2 + 2\ H_2CO_3 = 4HCO_3^- + Ca^{2+} + Mg^{2+} \tag{60}$$

$$CaCO_3 + {}^{1}\!/_{2}\ H_2SO_4 = Ca^{2+} + HCO_3^- + {}^{1}\!/_{2}\ SO_4^{2-} \tag{61}$$

$$CaMg(CO_3)_2 + H_2SO_4 = Ca^{2+} + Mg^{2+} + 2\ HCO_3^- + SO_4^{2-} \tag{62}$$

Silicates, per mole cation released

$$KAlSi_3O_8 + H_2CO_3 + {}^{1}\!/_{2}\ H_2O = K^+ + HCO_3^- + {}^{1}\!/_{2}\ Al_2Si_2O_5(OH)_4 + 2\ SiO_2 \tag{63}$$

$$\begin{aligned} &{}^{5}\!/_{4}\ NaAlSi_3O_8 + H_2CO_3 + {}^{5}\!/_{24}\ H_2O = Na^+ + HCO_3^- + \\ &\qquad {}^{5}\!/_{8}\ Na_{(2/5)}Al_{(28/15)}Si_4O_{10}(OH)_2 + {}^{1}\!/_{24}\ Al_2Si_2O_5(OH)_4 + {}^{7}\!/_{6}\ SiO_2 \end{aligned} \tag{64}$$

$$MgSiO_3 + 2\ H_2CO_3 = +\ 2\ HCO_3^- + Mg^{2+} + SiO_2 + H_2O \tag{65}$$

$$Ca_2Al_2Si_2O_8 + 2\ H_2CO_3 + H_2O = +\ 2\ HCO_3^- + Ca^{2+} + Al_2Si_2O_5(OH)_4 \tag{66}$$

$$KAlSi_3O_8 + {}^{1}\!/_{2}\ H_2SO_4 + {}^{1}\!/_{2}\ H_2O = K^+ + {}^{1}\!/_{2}\ Al_2Si_2O_5(OH)_4 + 2\ SiO_2 + {}^{1}\!/_{2}\ SO_4^{2-} \tag{67}$$

$$\begin{aligned} &{}^{5}\!/_{4}\ NaAlSi_3O_8 + {}^{1}\!/_{2}\ H_2SO_4 + {}^{5}\!/_{24}\ H_2O = Na^+ + {}^{1}\!/_{2}\ SO_4^{2-} + \\ &\qquad {}^{5}\!/_{8}\ Na_{(2/5)}Al_{(28/15)}Si_4O_{10}(OH)_2 + {}^{1}\!/_{24}\ Al_2Si_2O_5(OH)_4 + {}^{7}\!/_{6}\ SiO_2 \end{aligned} \tag{68}$$

$$MgSiO_3 + H_2SO_4 = Mg^{2+} + SiO_2 + SO_4^{2-} + H_2O \tag{69}$$

$$CaAl_2Si_2O_8 + H_2SO_4 + H_2O = SO_4^{2-} + Ca^{2+} + Al_2Si_2O_5(OH)_4 \tag{70}$$

purpose of this paper is to provide an overview of our overall approach and some standard model results and comparisons.

## MODEL ORGANIZATION

In this model, we have broadly partitioned material between the atmosphere, seawater, oceanic crust, and upper mantle. The continents (cratons) are subdivided into surface (including continental shelf and shallow subsurface) and deeper burial reservoirs that cycle at different rates. The following reactions govern transfers and transformations of material within each reservoir (sediments, dissolved components, gases, and crystalline rock): (1) weathering, (2) precipitation, diagenetic, and reduction-oxidation reactions, and (3) hydrothermal-magmatic reactions. Weathering reactions (table 1) consume primary crystalline Na-, K-, Ca-, and Mg-silicates and Ca- and Mg-carbonates through attack by both carbonic and sulfuric acids and produce clay minerals and dissolved cations, bicarbonate, sulfate, and dissolved silica. Simple dissolution of evaporites is also included in this group. Precipitation reactions (table 2) include formation of primary and secondary carbonate (calcite and dolomite) and evaporite (anhydrite, epsomite, halite and sylvite) phases. Low temperature diagenetic and redox reactions include the dissolution of these carbonates, the formation of aluminosilicate phases through so-called "reverse weathering" reactions, formation of organic matter and its subsequent oxidation by oxygen and sulfate, and the oxidation of sulfide (represented as pyrite) by oxygen. Hydrothermal-metamorphic-magmatic reactions (table 3) include reconstitution of primary silicates by reaction of carbonate minerals with clays, decarbonation of calcium and magnesium carbonates, dolomite formation by reaction of calcium carbonate with Mg-aluminosilicates (the ultimate source of Mg for dolomitization), seawater-basalt high and low temperature alteration reactions, and thermogenic sulfate reduction to form pyrite, which ultimately returns the oxygen originally consumed in pyrite oxidation. The latter process is problematic and discussed in more detail below. These reactions are written using normative

Table 2

*Low Temperature Precipitation, Diagenetic and Redox Reactions*

Carbonate and hydroxyapatite precipitation (no SR, per mole mineral)

$$2\ HCO_3^- + Ca^{2+} = CaCO_3 + CO_2 + H_2O \tag{71}$$

$$4\ HCO_3^- + Ca^{2+} + Mg^{2+} = CaMg(CO_3)_2 + 2\ CO_2 + 2\ H_2O \tag{72}$$

$$Ca_5(PO_4)_3OH + H^+ = 5\ Ca^{2+} + 3\ PO_4^{3-} + H_2O \tag{73}$$

Reverse weathering (RW) – aluminosilicate diagenesis

$$Mg^{2+} + {}^1/_5\ Al_2Si_2O_5(OH)_4 + 2\ HCO_3^- + {}^1/_5\ SiO_2 = {}^1/_5\ Mg_5Al_2Si_3O_{10}(OH)_8 + 2\ CO_2 + {}^3/_5\ H_2O \tag{74}$$

$$K^+ + {}^5/_4\ Na_{(2/5)}Al_{(28/15)}Si_4O_{10}(OH)_2 + {}^1/_4\ Al_2Si_2O_5(OH)_4 + {}^1/_2\ HCO_3^- = {}^5/_4\ K_{(4/5)}Al_{(34/15)}Si_{(18/5)}O_{10}(OH)_2 + {}^1/_2\ Na^+ + {}^1/_2\ CO_2 + SiO_2 + {}^3/_4\ H_2O \tag{75}$$

Sulfate reduction/carbonate precipitation (per mole S)

$${}^1/_4\ Fe_2O_3 + SO_4^{2-} + {}^{15}/_8\ CH_2O + Ca^{2+} = {}^1/_2\ FeS_2 + {}^7/_8\ CO_2 + {}^{15}/_8\ H_2O + CaCO_3 \tag{76}$$

Simple organic matter fixation/oxic oxidation

$$CO_2 + H_2O = O_2 + CH_2O \tag{77}$$

Pyrite oxidation

$${}^{15}/_8\ O_2 + {}^1/_2\ FeS_2 + H_2O = {}^1/_4\ Fe_2O_3 + 2\ H^+ + SO_4^{2-} \tag{78}$$

mineral phases or components to represent overall reaction stoichiometry. These simplifications ignore many intermediate weathering and alteration products, but preserve an overall mass balance during model operation.

### *Steady State Fluxes*

Because the number of coupled reservoirs and components is large, the model can be best understood in terms of principal subcycles that are themselves linked through transfers of carbon dioxide and oxygen: (1) Calcium-Magnesium-Silicate-Carbonate-$CO_2$, (2) Sodium-Potassium-Silicate-Carbonate-Chloride-$CO_2$, (3) Organic Carbon, (4) Sulfur, and (5) Iron and Phosphorous. These subcycles are illustrated in figures 1 through 5, respectively. Quaternary-averaged steady-state fluxes for these subcycles are tabulated in Appendix table A1; net atmospheric carbon dioxide and oxygen fluxes are provided in table A2.

To provide reasonable constraint on initial conditions for MAGic, we first calculated average Quaternary fluxes by assuming a balanced steady-state condition for all reservoirs. This assumption does not limit the overall operation of the model but merely provides a starting point and allows estimation of rate coefficients when appropriate. Values for reservoir masses and fluxes, reported in units of $10^{18}$ mols and $10^{18}$ mols/Ma, respectively, were obtained from searches of a large and diverse literature (for example, Garrels and Mackenzie, 1971; Garrels and Perry, 1974; Meybeck, 1979; Ronov, 1982; Berner and others, 1983; Holland, 1984; Lasaga and others, 1985; Gregor and others, 1988; Mackenzie, 1992; Compton and others, 2000). The initial model values are based on pre-anthropogenic estimates. These estimates are consistent with the composition of the dissolved load and the mineral and rock sources of individual dissolved components of rivers, the composition of materials

TABLE 3

*Hydrothermal-Magmatic Reactions*

Subduction-decarbonation

$$CaCO_3 + Al_2Si_2O_5(OH)_4 = CaAl_2Si_2O_8 + CO_2 + 2\ H_2O \tag{79}$$

Alteration reactions involving weathered silicates

$$^{1}/_{5}\ Mg_5Al_2Si_3O_{10}(OH)_8 + 2\ CaCO_3 + {}^{4}/_{5}\ Al_2Si_2O_5(OH)_4 = CaMg(CO_3)_2 + CaAl_2Si_2O_8 + {}^{1}/_{5}\ SiO_2 + {}^{12}/_{5}\ H_2O \tag{80}$$

$$^{1}/_{5}\ Mg_5Al_2Si_3O_{10}(OH)_8 + {}^{4}/_{5}\ SiO_2 = MgSiO_3 + {}^{1}/_{5}\ Al_2Si_2O_5(OH)_4 + {}^{2}/_{5}\ H_2O \tag{81}$$

$$^{5}/_{2}\ Na_{(2/5)}Al_{(28/15)}Si_4O_{10}(OH)_2 + {}^{7}/_{6}\ H_2O = NaAlSi_3O_8 + {}^{11}/_{6}\ Al_2Si_2O_5(OH)_4 + {}^{10}/_{3}\ SiO_2 \tag{82}$$

Seawater-basalt reactions

$$Mg^{2+} + CaAlSi_2O_8 + {}^{12}/_{5}\ H_2O + {}^{1}/_{5}\ SiO_2 = Ca^{2+} + {}^{1}/_{5}\ Mg_5Al_2Si_3O_{10}(OH)_8 + {}^{4}/_{5}\ Al_2Si_2O_5(OH)_4 \tag{83}$$

$$(Na^+,K^+) + HCO_3^- + CaAl_2Si_2O_8 + {}^{1}/_{2}\ H_2O + 2\ SiO_2 = (Na^+,K^+)AlSi_3O_8 + CaCO_3 + Al_2Si_2O_5(OH)_4 \tag{84}$$

$$^{5}/_{4}K_{(4/5)}Al_{(34/15)}Si_{(18/5)}O_{10}(OH)_2 + {}^{7}/_{12}\ H_2O + {}^{1}/_{3}\ SiO_2 = KAlSi_3O_8 + {}^{11}/_{12}\ Al_2Si_2O_5(OH)_4 \tag{85}$$

Net hydrothermal sulfate and iron reduction (balances $O_2$ consumed in pyrite oxidation)

$$SO_4^{2-} + {}^{11}/_{2}\ Fe_2SiO_4 + CO_2 + Ca^{2+} = {}^{1}/_{2}\ FeS_2 + {}^{7}/_{2}\ Fe_3O_4 + {}^{11}/_{2}\ SiO_2 + CaCO_3 \tag{86}$$

$$^{1}/_{4}\ Fe_2O_3 + 2\ H^+ + SO_4^{2-} = {}^{15}/_{8}\ O_2 + {}^{1}/_{2}\ FeS_2 + H_2O \tag{87}$$

cycled from sea to land through the atmosphere, the average and individual lithic compositions of sedimentary rocks, modern marine sediment compositions, and the composition of the geologically more recent ocean and atmosphere. Values consistent with these estimates were also adopted for the existing mass of sedimentary rocks, of oceanic salts, and of the total annual flux of elements through the oceanic environment. In order to close the cycles, best estimates were made of submarine basalt-seawater exchange fluxes and of fluxes involving diagenesis and alteration (so-called "reverse weathering" reactions, denoted RW in tables 2 and A2) of buried sediments (Martin and Sayles, 1994). Many of the assumptions made in the original quantitative model of the sedimentary rock cycle by Garrels and Mackenzie (1972), as well as those made in BLAG (Berner and others, 1983; Lasaga and others, 1985) and GEOCARB (Berner 1991, 1994, 1998, 1999; Berner and Kothavala, 2001), are valid for our model of the sedimentary rock cycle as linked to cycling processes involving submarine basalt alteration and subduction.

Following the approach given in BLAG, GEOCARB, and other related models, many of the fluxes are estimated by first computing a first order coefficient using average Quaternary ($t = 0$) values for the flux $f$ and mass M:

$$k_0 = (f/M)|_{t=0} \tag{1}$$

with the resulting flux computed as a function of time by

$$f(t) = kM(t) \tag{2}$$

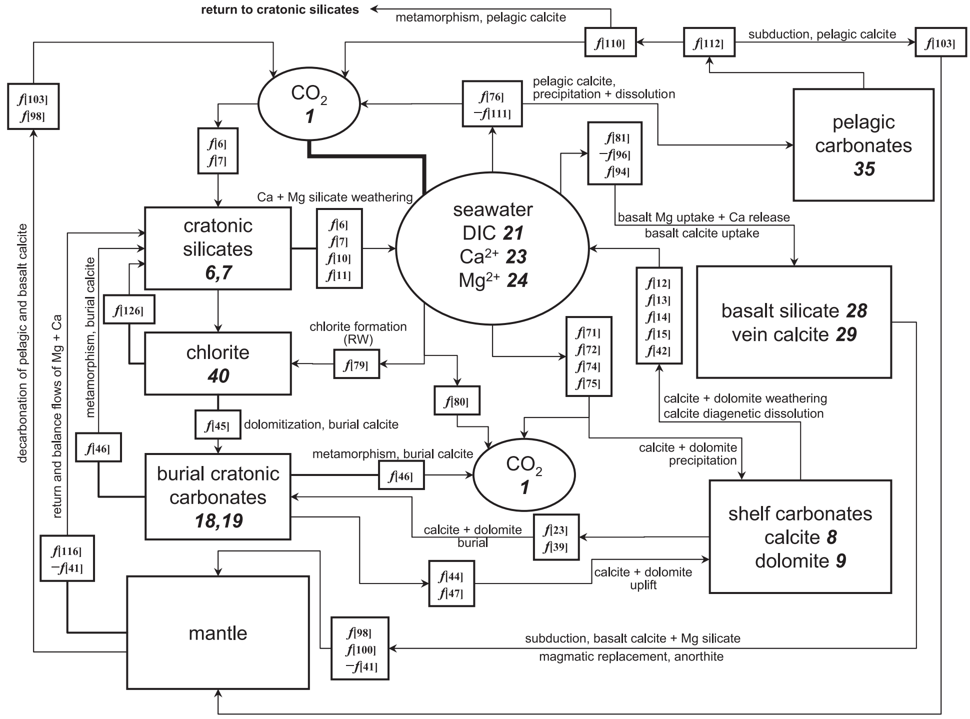

Fig. 1. Calcium-Magnesium-Silicate-Carbonate-$CO_2$ Subcycle. Numbered labels refer to either reservoir index (***identified by larger bold italic font***) or flux indices (denoted by $f[i]$, see table A1). *The sign of the flux* (for example, $-f[i]$) *indicates the direction of the flow with respect to the arrow,* and is positive unless so indicated; where fluxes are not labeled due to space constraints, a bold line indicates a bidirectional flow. Weathering of primary continental silicates, represented as normative anorthite (***6***) and Mg-pyroxene (***7***), and shelf carbonates calcite (***8***) and dolomite (***9***), occurs through attack by carbonic and sulfuric acids (see *Sulfur Subcycle* in fig. 4), and results in riverine fluxes of dissolved calcium ($f[6], f[10], f[12] - f[15]$), magnesium ($f[7], f[11], f[13], f[15]$), and associated bicarbonate. Dolomite deposition in shallow marine sediments is represented by a saturation state-driven flux ($f[75]$) and by a flux proportional to microbial sulfate reduction ($f[71]$). Calcite depositional fluxes are computed to be consistent with fluid inclusion data (Mg/Ca), and are associated with either shallow marine ($f[74] + f[72]$, the latter driven by sulfate reduction) and pelagic ($f[76]$, ***35***) reservoirs. Partitioning between shelf and pelagic calcite is governed by a time-dependent β parameter. Shelf calcite and dolomite are then either re-weathered or enter a deeper burial regime ($f[39], f[23]$). Basalt-seawater reactions consist of magnesium uptake ($f[81]$) and net calcium release ($f[96]$); some calcium is also consumed in the formation of basalt calcite ($f[94]$, ***29***); this carbon is eventually consumed during subduction ($f[98]$), returning $CO_2$ to the atmosphere. Diagenetic alteration of shelf ($f[42]$) and pelagic ($f[111]$) sediments results in calcium and bicarbonate fluxes to seawater, a "reverse weathering" magnesium flux to chlorite ($f[79]$), and $CO_2$ release ($f[80]$). Dolomite formed in the cratonic burial regime (***19***) consumes burial calcite (***18***), but is limited by magnesium supplied by the chlorite reservoir ($f[45]$, ***40***), and is eventually returned by uplift to the continental weathering regime ($f[44]$). Burial calcite not consumed by dolomitization is either uplifted ($f[47]$), or eventually returns $CO_2$ to the atmosphere and calcium to the silicate reservoir by metamorphic decarbonation ($f[46]$). Pelagic calcite is consumed through subduction ($f[103]$) and metamorphism ($f[110]$), with the partitioning between these targets controlled by a σ parameter. Steady state fluxes are also listed in table A1. Not all fluxes (for example, $CO_2$ exchanges associated precipitation and weathering) are shown.

These coefficients may themselves be held constant ($k = k_0$) or varied with time ($k = k(t)$). In the latter case, this variation is accommodated by application of one or more dimensionless parameters, for example,

$$k(t) = k_0 c_1(t) c_2(t) \tag{3}$$

These time-dependent parameters are used to amplify or attenuate various processes related to land mass exposure, $CO_2$ weathering feedbacks, seafloor spreading rate,

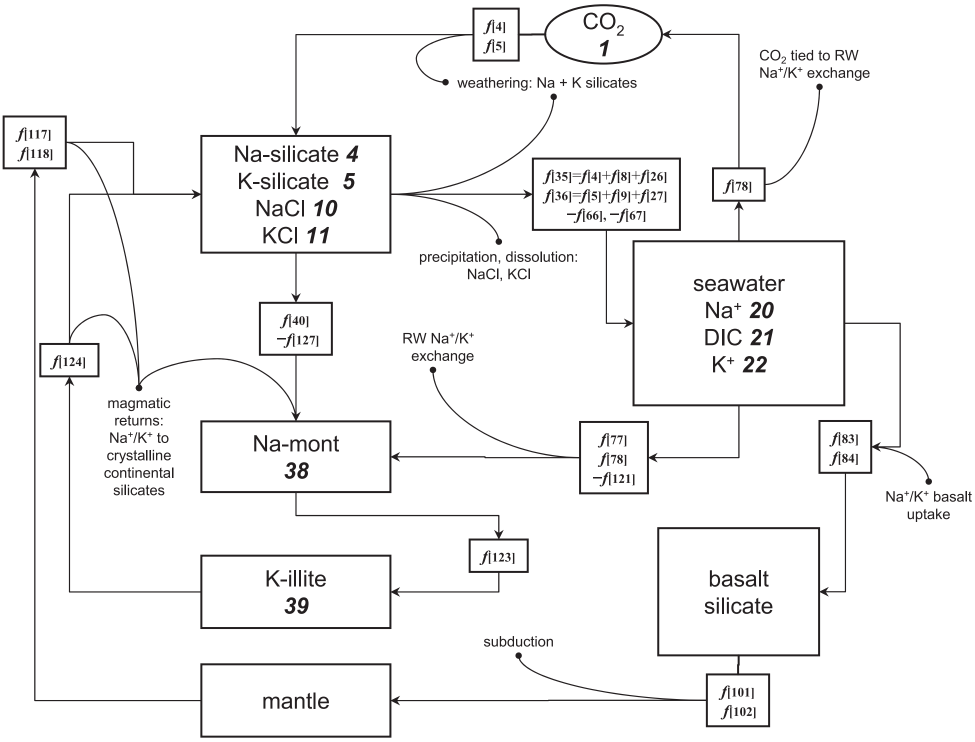

Fig. 2. Sodium-Potassium-Silicate-Carbonate-Chloride-CO$_2$ Subcycle. See figure 1 caption for description of index notation of reservoirs and fluxes. Bold lines indicate bidirectional flows. Sodium and potassium are derived from weathering of Na-silicates ($f[4], f[8]$, ***4***), K-silicates ($f[5], f[9]$, ***5***), NaCl ($f[26]$, ***10***) and KCl ($f[27]$, ***11***), and balanced by bicarbonate, pyrite-derived sulfate, and chloride ($f[35] = f[4] + f[8] + f[26], f[36] = f[5] + f[9] + f[27]$). In seawater, dissolved Na$^+$ (***20***) and K$^+$ (***22***) are either re-deposited as evaporites via simple precipitation reactions ($f[66], f[67]$), or abstracted by seafloor basalt to form altered silicates ($f[83], f[84]$). Seawater K$^+$ is also taken up by detrital silicates in reverse weathering reactions ($f[77]$), where it is exchanged for Na$^+$ ($f[78]$) as a flux of Na-montmorillonite ($f[123]$, ***38***) to form K-illite (***39***). Alteration products formed from reverse weathering and basalt uptake are ultimately returned to the craton ($f[117], f[118], f[124]$), where they are reincorporated in primary silicates to start a new weathering cycle.

sedimentary basin partitioning, *et cetera*, and are described where necessary in the sections below and summarized in table 4.

### *Continental Weathering Fluxes and CO$_2$*

Weathering fluxes are computed using equations similar to those in GEOCARB III (Berner and Kothavala, 2001), that is, by evaluating a feedback function sensitive to CO$_2$ and additional parameters reflecting the role of vascular land plant fertilization, runoff, paleogeography, and differential susceptibility of carbonate and silicate rock types to weathering. In addition, weathering rate constants were also calibrated (eq 3) by additional time-dependent terms for land area, runoff, relief, and land plants. These parameters are adapted directly from GEOCARB III, which in turn were derived from estimates of these terms in the geological literature. Discussion of these terms is available in the various GEOCARB papers (for example, Berner and others, 1983; Berner and Kothavala, 2001) and is not repeated here.

### *Diagenetic and Reverse Weathering Fluxes*

Reverse weathering as a sink for oceanic elements was proposed more than 40 years ago (Garrels, 1965; Mackenzie and Garrels, 1966a, 1996b). According to this

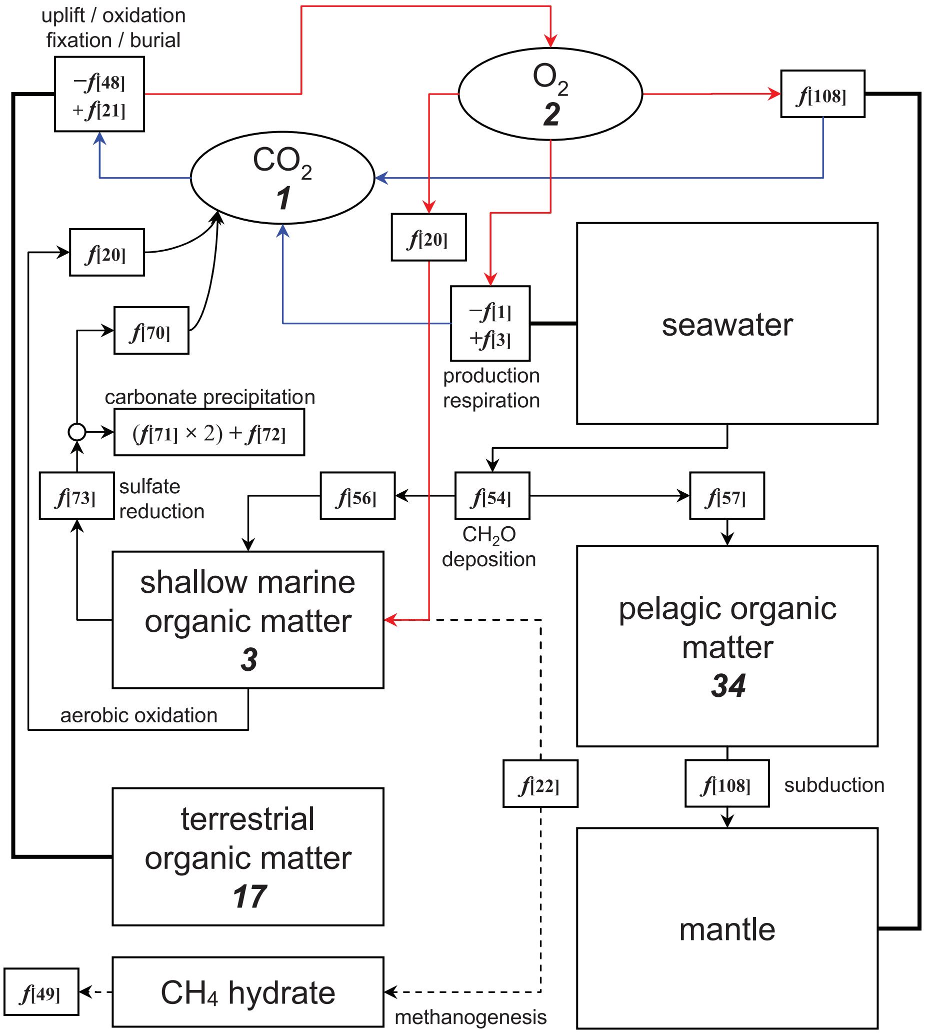

Fig. 3. Organic Carbon Subcycle. See figure 1 caption for description of index notation of reservoirs and fluxes. Bold lines indicate bidirectional flows. Red and blue arrows indicate flows of $O_2$ and $CO_2$, respectively. Marine organic carbon production is governed by relationships similar to those employed in the model of Van Cappellen and Ingall (1996), in which primary productivity ($f$[1]) is controlled by the availability of organic phosphorous (see *Iron and Phosphorous Subcycle*, fig. 5). A fraction ($f$[54]) of the marine productivity flux is then available for organic carbon sedimentation; the remainder is respired and returned as $CO_2$ ($f$[3]). Organic carbon sedimentation is then partitioned into shallow marine ($f$[56], ***3***) and pelagic environments ($f$[57], ***34***). Shallow marine organic matter is then respired by two routes. Anaerobic oxidation via microbial sulfate reduction and pyritization ($f[73] = \frac{15}{8} f[50]$, where $f$[50] is sulfate reduction flux, see fig. 4) results in carbonate mineral formation (carbon flux to dolomite = 2 × $f$[71] and calcite = $f$[72]) and $CO_2$ release ($f$[70]). Aerobic oxidation returns the remainder of shelf organic carbon as $CO_2$ during organic matter weathering ($f$[20]). Pelagic organic matter is subducted and also returned as $CO_2$ ($f$[108]). As in Berner and Canfield (1989), a terrestrial organic matter burial flux ($f$[21]) is computed from a record of sedimentary organic carbon (constraint curve $c_{BU}$). Subsequent uplift and oxidation flux of this material ($f$[48]) is first order with respect to reservoir mass (***17***). A gas hydrate shunt ($f$[22], $f$[49]) has not been implemented in the current version of the model.

hypothesis, the formation of clay minerals in marine sediments leads to the removal of soluble cations such as $Mg^{2+}$ and $K^+$, and the discharge of acidity ($CO_2$), the opposite pathway of the weathering reaction. Conclusive field tests of this hypothesis have been difficult because the quantity of authigenic minerals that form is small and the

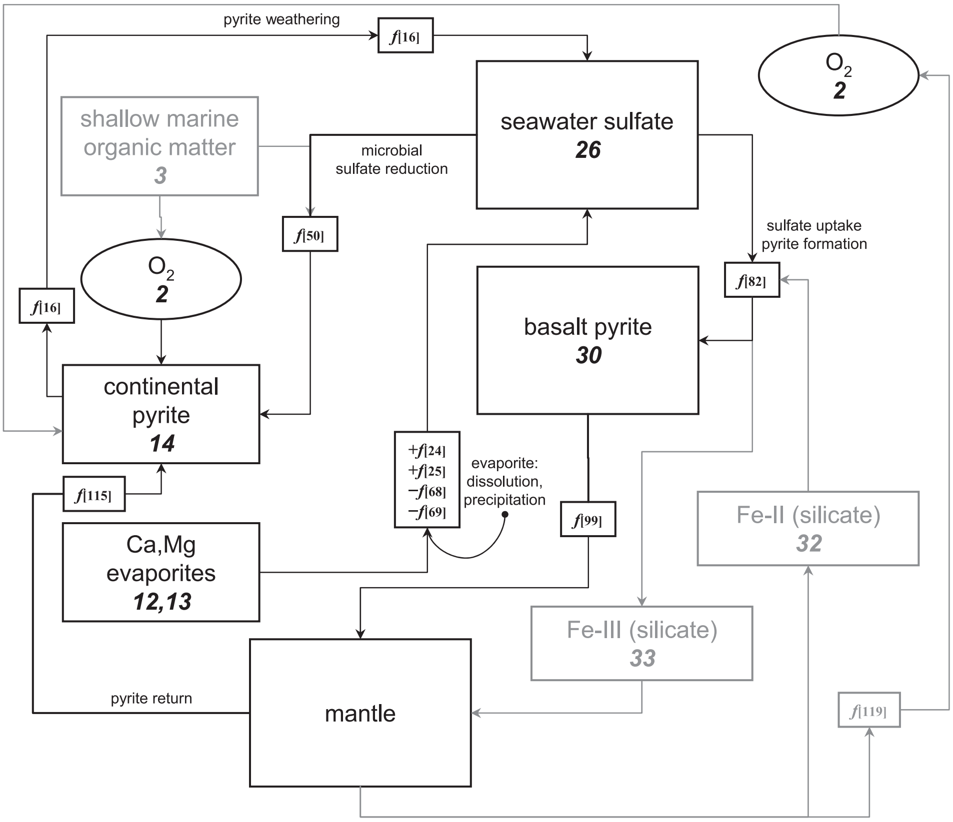

Fig. 4. Sulfur Subcycle. Labeling scheme is similar to figure 1. Grayed portions of the figure are examined in more detail in figures 5 and 15. Sulfur is delivered to the ocean as sulfate derived from the weathering of pyrite (*f* [16], ***14***) and dissolution of evaporite minerals $CaSO_4$ (*f* [24], ***12***) and $MgSO_4$ (*f* [25], ***13***). Seawater sulfate is consumed by precipitation of evaporites (*f* [68], *f* [69],), and during sulfate reduction and pyritization, both within shallow marine sediment (*f* [50]) and during hydrothermal reaction of seawater and basalt (*f* [82], ***30***). The rate of microbial sulfate reduction is tied to the availability of reactive (ferric) iron (see fig. 5). Sulfide formed by sulfate reduction is then returned and made available for oxidation and weathering. Oxidation of this sulfide (*f* [16]) consumes the oxygen initially liberated by organic matter production, and yields sulfuric acid for weathering. The reduction of sulfate to basalt pyrite also consumes ferrous iron (silicate) and produces ferric iron; subduction of this ferric iron yields a return oxygen flux (*f* [119]), explained in more detail in the text (see also figs. 5 and 15).

neoformed phases are generally found in the very fine-grained sizes of the sediment. Thus, it is extremely difficult to detect these phases in marine sediments without time-consuming and tedious sediment size separations and detailed determination of their mineralogy and chemistry. Early studies of nearshore muddy sediments did not confirm that reverse weathering reactions occur (Russell, 1970; Drever, 1971), possibly because the studies were insufficiently detailed to permit detection of the small quantities of neoformed minerals present in the fine-grained fractions of the sediment. More recently, work has demonstrated the rapid formation of aluminosilicates in marine sediments and the possibility that the formation of these phases is a potentially important sink of oceanic K and Mg (Mackenzie and others, 1981; Michalopoulos and Aller, 1995). In addition, early diagenetic reactions involving dissolved aluminum in sediments (for example, Stoffyn-Egli, 1982) suggest the involvement of aluminum, silicon, and cations in the formation of authigenic aluminosilicate phases in modern marine sediments.

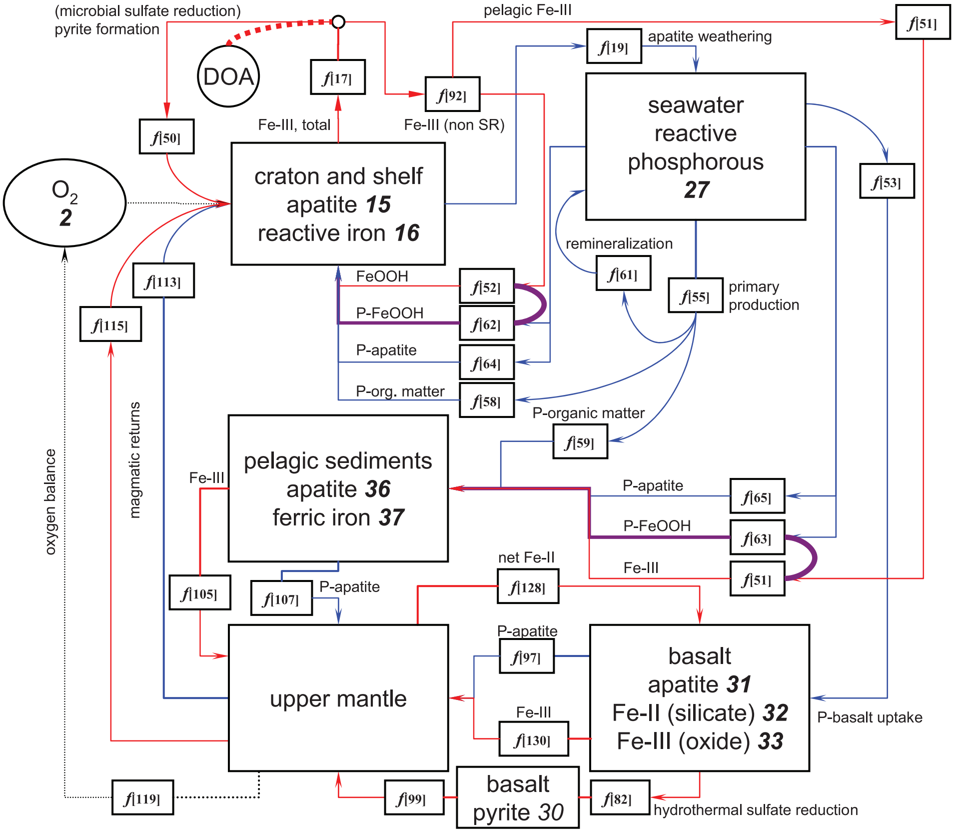

Fig. 5. Iron and Phosphorous Subcycle. Labeling scheme is similar to figure 1. Iron fluxes are shown in red, phosphorous in blue; P complexed with ferric iron is shown as magenta. The cycling of iron and phosphorous assimilates the approach of Van Cappellen and Ingall (1996), in which phosphorous availability exerts a fundamental control on long term ecosystem productivity. Phosphorous is delivered to seawater by apatite weathering (*f* [19]). The rate of organic phosphorous fixation, *f* [55], determines gross productivity (*f* [1], see fig. 3). The fixation rate is a first order function of the reactive phosphorous pool (***27***) and a constant parameter describing oceanic ventilation rate ($V_{MIX}$). The burial fluxes of organic phosphorous in shelf (*f* [58]) and pelagic (*f* [59]) regimes are computed from the respective organic carbon burial fluxes (*f* [56] and *f* [57]; see fig. 3) and the C/P ratio. The C/P ratio is calculated using the DOA function (degree of anoxicity), in turn dependent on atmospheric oxygen mass (*2*) and *f* [1] (see text for details). The fraction of organic phosphorous that is *not* buried is returned to the reactive phosphorous pool (*f* [61]). In addition to the burial flux of phosphorous incorporated in organic matter, reactive phosphorous is also consumed during basalt uptake (*f* [53]), sedimentary apatite precipitation (shelf *f* [64], pelagic *f* [65], both tied to *f* [61]), and by binding to sedimented ferric iron as Fe-P complexes (shelf *f* [62], pelagic *f* [63]). All phosphorous is ultimately recycled to the continents as apatite: P in subducted pelagic sediments and basalt is returned via a mantle flux (*f* [113]).

The link between ferric iron and phosphorous provides critical buffering of atmospheric oxygen. The ferric iron flux (*f* [17], which includes iron originally derived from pyrite oxidation on land) is the source of iron for subsequent pyrite formation and that bound as Fe-P complexes. Thus iron consumed in the formation of pyrite during microbial sulfate reduction (*f* [50]) comes at the expense of ferric iron available for complexation with phosphorous (this remainder = *f* [92]) in shelf (*f* [52]) and in pelagic sediments (*f* [51]). Moreover, this partitioning is in turn a function of DOA: as DOA tends toward unity (complete anoxia), the ferric iron fraction decreases to zero. This feedback thus returns reactive phosphorous to the water column and makes it available for fixation, ultimately increasing $O_2$ production, and restoring oxic conditions. Ferrous iron from iron silicate is used as the electron donor during hydrothermal sulfate reduction (*f* [82], see fig. 4). The oxide produced, together with pelagic ferric iron and basalt pyrite, is eventually subducted (*f* [130] + *f* [105] + *f* [99]). Pyrite iron is returned to the weathering cycle (*f* [115], fig. 4). The balance of the iron is returned to the basalt as reduced iron silicate (*f* [128]). Because iron is returned to the weathering cycle in a reduced state, the oxygen that will eventually be consumed must be supplied by a balancing flux (*f* [119]), possibly through consumption of a more reduced (and undefined) mantle component. Without this balancing flux, the mantle will act as an oxide sink.

TABLE 4

*Time-dependent dimensionless coefficients used in weathering and related equations ($c_{BU}$ computed from Budyko and others, 1987; others adapted from Berner, Lasaga, and Garrels, 1983; Berner and Kothavala, 2001)*

| **Variable** | **Description** |
|---|---|
| $c_{BU}$ | (d/dt) terrestrial organic matter |
| $c_{ADs}$ | area × runoff (silicates) |
| $c_{AD}$ | area × runoff (carbonates) |
| $c_{Ap}$ | shelf depositional area |
| $c_{Aw}$ | area available for weathering |
| $c_{Bs}$ | $CO_2$ weathering feedback (silicates) |
| $c_{Bc}$ | $CO_2$ weathering feedback (carbonates) |
| $c_{E}$ | terrestrial plant weathering |
| $c_{R}$ | uplift/relief |
| $c_{LA}$ | carbonate land area |
| $c_{D}$ | runoff |
| $c_{GEOG}$ | paleogeographic effect |
| $c_{G}$ | subduction/degassing rate |

Another diagenetic reaction of interest is the uptake of $Mg^{2+}$ in clay minerals during halmyrolysis and diagenesis in marine sediments that is balanced by the release of $Ca^{2+}$ (Martin and Sayles, 1994), subsequently precipitated as $CaCO_3$. This exchange reaction does not affect the $CO_2$ balance of the atmosphere-ocean system, as do reverse weathering reactions.

Wollast and Mackenzie (1983) found that the balance between dissolved constituents entering the ocean via rivers and submarine basalt-seawater reactions and oceanic sinks, as well as that for particulate materials, required uptake of $Mg^{2+}$ and $K^+$ in exchange and reverse weathering reactions involving clay minerals. They suggested that these reactions might be responsible for the removal of as much as 50 percent of the weathering inputs of $Mg^{2+}$, and 50 percent of the river input of $K^+$ from sediment-porewater systems. These findings lead to the conclusion that exchange and reverse weathering reactions involving clay minerals are viable processes in terms of cation removal, at least for $Mg^{2+}$ and $K^+$, and should be a part of any model that attempts to depict the behavior of the sedimentary cycle over geologic time.

### *Seawater Saturation State, Model Operation, and Notation*

Because of the potential for significant variation in composition over geologic time, seawater cannot be regarded as a constant ionic medium, and thus the expressions (apparent constants) commonly used to compute $CO_2$-carbonic acid-carbonate equilibria in seawater (for example, Dickson and Millero, 1987) are not appropriate. We have instead adopted Pitzer's approach in computing thermodynamic properties of seawater (Pitzer, 1973), extended with the parameters supplied by He and Morse (1993) for the carbonic acid system. At each time step, pH and carbonate mineral saturation state ($\Omega \equiv e^{G/RT} = \mathrm{IAP}/K$) are computed from temperature, $PCO_2$, the current vector of concentrations of $Ca^{2+}$, $Mg^{2+}$, $K^+$, $Na^+$, $Cl^-$, $SO_4^{2-}$, and total dissolved

C ($CO_{2\,(aq)} + HCO_3^- + CO_3^{2-}$). The ocean is thus considered to be perfectly mixed and in equilibrium with atmospheric $CO_2$, a valid assumption given the rapid mixing time of the ocean relative to the long time scale of our calculations. However, direct calculation of seawater activities introduces considerable complexity into the model, primarily in terms of potential depletion of the atmospheric $CO_2$ reservoir and valid evaluation of hydrogen ion activity by the iterative Pitzer routines at each time step. Because of this complexity, we discuss the calculation approach in more detail. The model operation consists of the following sequence:

1) Initialization and preliminary spin-up:
    a) Read initial ($t = t_0$) reservoir masses $y(t_0)$, iteration control parameters, runtime options.
    b) Compute steady state values for rate coefficients ($k_0$).
    c) Compute Pitzer parameters for dissolved seawater components.
    d) Compute time-dependent parameters and feedback functions.
    e) Initialize rate coefficients ($k$).
    f) Compute balance on function derivatives $y'(t_0)$.
    g) Hold $t$-dependent functions constant and iterate until $\Sigma_i(y_i' / y_i) < 2\%$ for atmosphere and seawater components.

2) Iteration from time $t = t_0$ to $t = 0$. At each time step $t_{i+1} = t_i + \Delta t_i$:
    a) Update time-dependent parameters, feedback functions, and rate coefficients.
    b) Compute saturation state from seawater composition and current $PCO_2$.
    c) Compute precipitation rates, weathering and exchange fluxes, fixation rates.
    d) Correct fluxes to be consistent with seawater ratio constraints.
    e) Take tentative step on $y$ and evaluate error: If error is within limits, update $y$, store results and begin new time step, otherwise revise step size $\Delta t_i$ and repeat.

Thus during model operation, the step size ($\Delta t_i$) is not fixed but varies according to the difficulty and constraints imposed by the equations described below. All time-dependent parameters ($c_i$) are available as smooth spline fits to the original data.

The general model, written in double precision FORTRAN 90, consists of forty coupled nonlinear ordinary differential equations, as well as over 100 fluxes, time-dependent rate constants, and associated parameters. It is solved as an explicit initial value problem using an Adams-Moulton predictor-corrector algorithm (DIVPAG, IMSL FORTRAN Numerical Library version 5.0, Visual Numerics, Inc.). With full compiler optimization and parallelization (INTEL VISUAL FORTRAN IA32), the model requires ~ 5 minutes for the complete 500 Ma run on a 2.1 GHz personal computer (dual AMD Athlon MP processors). To avoid confusion, model time ($t$) is negative in the past and has implicit units of Ma, thus $t_0 = -500$ Ma, and the time of Quaternary completion indicated by $t = 0$. The 40 differential equations and constituent fluxes that compose the overall model, organized by reservoir, are given in Appendix table A3.

The notation scheme in this paper was designed to minimize the confusion in referring to the large number of reservoirs, components, fluxes, and associated parameters. The mass of the $i^{th}$ reservoir component is denoted $y[i]$, for which steady state (Quaternary) masses in absolute units are listed in table A3; in the text these masses are usually expressed relative to these Quaternary values (that is, $y[2]|_{t=0} = 1$). Fluxes $f$ and their associated coefficients $k$ are indexed in square brackets ($f[1]$, $f[2]$, . . . $k[1]$, $k[2]$, and so on) according to their approximate order of appearance in the program. Fluxes not described in detail in the text appear instead in the figures and Appendix tables A1 and A2.

### *Calcium-Magnesium-Silicate-Carbonate-$CO_2$ Subcycle*

The geochemical cycle of calcium and magnesium (fig. 1, table A1) is the most important in terms of its interaction with carbon and the long-term maintenance of $CO_2$. It is also the most complex. Calcium and magnesium are initially weathered from continental silicates and carbonates by carbonic and sulfuric acids (fluxes $f[6]$, $f[7]$, $f[10]$, $f[11]$, $f[12]$, $f[13]$, $f[14]$, and $f[15]$, fig. 1, table A1; Ca-Mg evaporite weathering is described in the sulfur subcycle). These fluxes are computed as a function of time following the template of equations 1 – 3:

Ca silicate:

$$f[6] = k[6]y[6] \tag{4}$$

$$f[10] = \gamma[21]f[16] \tag{5}$$

Mg Silicate:

$$f[7] = k[7]y[7] \tag{6}$$

$$f[11] = \gamma[22]f[16] \tag{7}$$

Calcite:

$$f[12] = k[8]y[8] \tag{8}$$

$$f[14] = 2\gamma[19]f[16] \tag{9}$$

Dolomite:

$$f[13] = k[9]y[9] \tag{10}$$

$$f[15] = \gamma[20]f[16] \tag{11}$$

where

$$k[6] = k_0[6]c_{\mathrm{ADs}}c_{\mathrm{R}}c_{\mathrm{Bs}}c_{\mathrm{E}} \tag{12}$$

$$k[7] = k_0[7]c_{\mathrm{ADs}}c_{\mathrm{R}}c_{\mathrm{Bs}}c_{\mathrm{E}} \tag{13}$$

$$k[8] = k_0[8]c_{\mathrm{LA}}c_{\mathrm{Bc}}c_{\mathrm{E}} \tag{14}$$

$$k[9] = k_0[9]c_{\mathrm{LA}}c_{\mathrm{Bc}}c_{\mathrm{E}} \tag{15}$$

and $\gamma[i]$ is the fraction of the total pyrite weathering flux ($f[16]$) for each rock type, and $y[6]$, $y[7]$, $y[8]$, $y[9]$ are the masses of Ca- and Mg-silicate, calcite, and dolomite, respectively (see table A3). As an aside, the actions of GEOCARB dimensionless parameters in equations 12 – 15, reflecting the time-dependent forcing imposed by land area/runoff, relief, $CO_2$ feedbacks, land plants, and palegeography, exist for *most* of the coefficients ($k$) related to weathering presented in the remaining descriptions. In these cases, weathering parameters are used without change from Berner and Kothavala (2001), and thus will *not* appear explicitly except as warranted for clarity (see table 4). The trend of key forcing functions is shown in figure 6.

Once present in seawater, these components are redeposited in shelf environments as primary or secondary calcite ($f[74]$, $f[72]$), dolomite ($f[75]$, $f[71]$) and $CaSO_4$ and $MgSO_4$ evaporites ($f[68]$, $f[69]$). Subsequent to deposition, they either reenter the weathering cycle through uplift and exposure ($f[12]$, $f[13]$), ($f[14]$, and $f[15]$) or are removed to deeper burial regimes ($f[39]$, $f[23]$). Pelagic environments receive only calcium carbonate ($f[74]$), with the total $CaCO_3$ flux ($f[93]$) partitioned between shelf and pelagic regimes by a time-dependent ($\beta$) parameter:

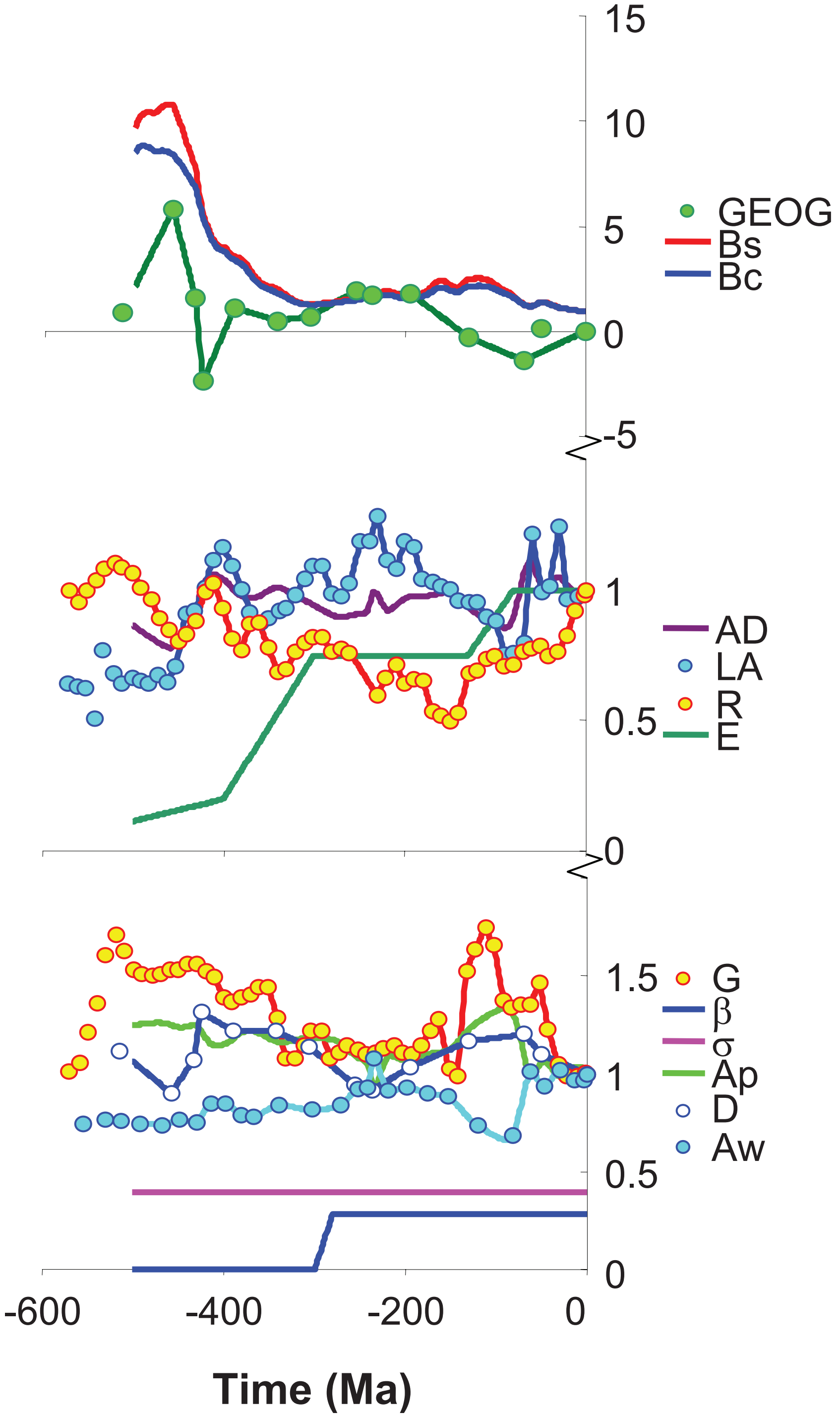

Fig. 6. Time variation of forcing parameters (see also table 4). GEOG = $c_{GEOG}$, paleogeographic effect; Bs = $c_{Bs}$, $CO_2$ weathering feedback (silicates); Bc = $c_{Bc}$, $CO_2$ weathering feedback (carbonates); AD = $c_{AD}$, area × runoff (carbonates); LA = $c_{LA}$, carbonate land area; R = $c_R$, uplift/relief; E = $c_E$, terrestrial plant weathering; G = $c_G$, degassing rate; Ap = $c_{Ap}$, shelf depositional area; D = $c_D$, runoff; Aw = $c_{Aw}$, weathering area. Data are from Berner and Kothavala (2001) and Berner and others (1983). β is shelf-pelagic partitioning factor (β = 0 constrains all precipitation to occur on the shelf). σ is partitioning the fate of pelagic carbonate sediment to subduction versus metamorphic regimes. Bs and Bc trends are taken from standard run (see fig. 7).

$$f[76] = \beta(t)f[93] \tag{16}$$

$$f[74] = (1 - \beta(t))f[93] \tag{17}$$

We should note here that our pelagic reservoir includes slope and rise sediments as well. The value of $\beta$ is varied to produce the observed increase in carbonate pelagic deposition during the Mesozoic (Garrels and Mackenzie, 1971; Wilkinson and Walker, 1989). At each time step, the total precipitation flux of calcite ($f\,[93]$) is calculated from the current values of seawater Mg ($y[24]$) and Ca masses ($y[23]$), their respective derivatives, and other fluxes involving calcium and magnesium (see table A3):

$$f[93] = (y[23]/y[24])(y[23]\boldsymbol{R}'(t) - (f[34] - f[69] - [79] - f[81] - f[75] - f[71])) \\ + f[33] - f[75] - f[72] - f[71] - f[68] + f[42] + f[111] + f[96] \tag{18}$$

where the derivative of the cation ratio ($\boldsymbol{R}'(t)$) is computed from the fluid inclusion data of Lowenstein and others (2001) and Hardie (1996).

Shelf dolomite precipitation rate ($f\,[75]$) is controlled by seawater saturation state; dolomite is also formed in the same environment during the oxidation of organic matter ("organogenic" dolomitization, $f\,[71]$), tied to the rate of microbial sulfate reduction ($f[50]$):

$$f[71] = (f[71]/f[50])|_{t=0}f[50] \tag{19}$$

$$f[75] = r(\Omega) \times c'_{\mathrm{Ap}}(t)(f[75]/r(\Omega))|_{t=0} \tag{20}$$

In equation (19), $(f\,[71]/f\,[50])_{|t\,=\,0}$ is the ratio of steady state Quaternary (preglacial) fluxes. In equation (20), $c'_{\mathrm{Ap}}(t)$ is a function describing the shelf area available for deposition of carbonate sediment. This function is estimated from Quaternary deposition fluxes in shallow water environments and the submerged shelf area as a function of time, and is normalized to its Quaternary value (thus $c'_{\mathrm{Ap}}(0) = 1$). Similarly, $r(\Omega) = k_{\mathrm{T}}\ (\Omega_{\mathrm{dol}} - 1)^n$, where $\Omega_{\mathrm{dol}}$ is the saturation state of seawater with respect to dolomite, $k_{\mathrm{T}}$ and $n$ are the rate constant and reaction order taken from experimental work (Arvidson and Mackenzie, 1999), and $(f\,[75]\ /\ r\ (\Omega))_{|t\,=\,0}$ is the ratio evaluated at their Quaternary steady state values.

After deposition, pelagic calcite is either subducted to the mantle ($f\,[103]$) or removed to a metamorphic regime ($f\,[110]$); partitioning of the total pelagic flux ($f\,[112]$) between these two paths is controlled by another time-dependent ($\sigma$) parameter (Volk, 1989):

$$f[103] = \sigma f[112] \tag{21}$$

$$f[110] = (1 - \sigma)f[112] \tag{22}$$

Both of these pathways lead to decarbonation reactions that serve to return material to the weathering cycle. We should note here that in the model the mantle does not constitute a reservoir *per se*, but simply a collection point for return fluxes to either the silicate (basaltic or continental crust) or atmospheric reservoirs. This simplification, although significant, was made to avoid the necessity of estimating mantle abundances and time-dependent fluxes that are not well known and would introduce additional uncertainty in the model. Basalt-seawater reactions result in magnesium uptake ($f[81]$) and calcium release ($f[96]$). Magnesium uptake is assumed to be first order with respect to the $Mg^{2+}$ concentration in seawater, $y[16]$; the rate coefficient for this uptake is modified by the time-dependent parameter reflecting seafloor spreading rate, $c_{\mathrm{G}}$, that is,

$$f[81] = c_G(t)k[44]y[16] \tag{23}$$

(see table 4). The $c_G$ parameter is identical to the $f_G$ parameter in GEOCARB III (Berner and Kothavala, 2001), using the curve concatenated from the data of Engebretson and others (1992) and Gaffin (1987).

The complementary release of $Ca^{2+}$ from basalt during seawater-basalt interaction ($f$[96]), although identical to the magnesium uptake flux ($f$[81]) in the steady state (Quaternary) condition, is allowed to otherwise vary to balance with the uptake fluxes, a description of which we will postpone to our later discussion of the standard run. In addition, diagenetic alteration of shelf ($f$[42]) and pelagic ($f$[111]) sediments also results in release of calcium to seawater that is first order with respect to sediment masses ($y$[3], $y$[4]):

$$f[42] = k[18]y[3] \tag{24}$$

$$f[111] = k[58]y[4] \tag{25}$$

Magnesium uptake ($f$[79]) by the sediment to form chlorite, a mineral composition representative of neoformed magnesium-rich silicates, is allowed to vary according to seawater $Mg^{2+}$ mass ($y$[16]):

$$f[79] = k[43]y[16] \tag{26}$$

The chlorite thus formed reacts with buried calcite to form burial dolomite. The rate of burial dolomite formation ($f$(45)) is thus limited by the size of the chlorite reservoir ($y$[35]):

$$f[45] = k[60]y[35] \tag{27}$$

This dolomite is eventually returned by uplift to the continental weathering regime, and burial calcite not consumed by dolomitization eventually returns $CO_2$ to the atmosphere and calcium to the silicate reservoir by metamorphic decarbonation ($f$[46]).

### *Sodium-Potassium-Silicate-Carbonate-Chloride-$CO_2$ Subcycle*

Sodium and potassium river fluxes are derived from the weathering of Na- and K-silicate masses ($y$[4], $y$[5]) by both $CO_2$ ($f$ [4], $f$ [5]) and $H_2SO_4$ derived from oxidation of $FeS_2$ ($f$[8], $f$[9]), and NaCl and KCl evaporites ($f$[26], $f$[27]), and are thus balanced by bicarbonate, pyrite-derived sulfate, and chloride (fig. 2 and table A1):

Na silicate:

$$f[4] = k[4]y[4] \tag{28}$$

$$f[8] = 2\gamma[23]f[16] \tag{29}$$

K silicate:

$$f[5] = k[5]y[5] \tag{30}$$

$$f[9] = 2\gamma[22]f[16] \tag{31}$$

In basalt-seawater reactions, the basalt uptake fluxes of $Na^+$, $K^+$, and $SO_4^{2-}$ ($f$[83], $f$[84], and $f$[82]) are first order with respect to their seawater masses ($y$[13], $y$[14], and $y$[26]); A basalt calcite flux ($f$ [94]) accounts for bicarbonate uptake and $CO_2$ release ($f$ [85]), described in detail in the MODEL RESULTS AND DISCUSSION section.

$$Na^+: f[83] = c_G(t)k[46]y[13] \tag{32}$$

$$K^{+}: f[84] = c_G(t)k[47]y[14] \tag{33}$$

$$SO_4^{2-}: f[82] = c_G(t)k[45]y[17] \tag{34}$$

$$HCO_3^{-}: f[85] = \tfrac{1}{2}f[94] \tag{35}$$

At steady state, these sulfate and bicarbonate fluxes balance the $H_2SO_4$-derived pyrite and $CO_2$ involved in the original weathering reactions. The bicarbonate reacts with Ca minerals within the basalt to form calcite (see Alt and Teagle, 1999; some calcium is derived from seawater itself but the amount is debatable) that is ultimately returned to the cratonic weathering cycle ($f$[98], fig. 2). $Na^+$ and $K^+$ taken up within the basalt are used to form silicate alteration products, and these are ultimately subducted ($f$[101], $f$ [102]) and returned to the craton ($f$ [117], $f$ [118]). Sulfate is reduced during oxidization of iron silicates in the basalt to form pyrite. We emphasize here that this is not the pyrite formed by low-temperature, diagenetic reactions in marine sediments in the model. The hematite or magnetite, produced by the reaction involving reduction of sulfate in the basalt, must itself be subsequently reduced after subduction of the oceanic crust to liberate the free oxygen necessary to weather pyrite returned to the craton (see table 3 and fig. 4). If this is not done, the mantle will act as an oxygen sink (Lécuyer and Ricard, 1999). The implications of this treatment of cation and anion seawater-basalt fluxes are also discussed below.

Steady state chloride balance is preserved through simple precipitation of NaCl and KCl ($f$ [66], $f$ [67])—no volcanic HCl component is currently included. These fluxes are varied during model operation in first order proportion to their respective ion activity products. In addition, $K^+$ is also exchanged for $Na^+$ during diagenetic reactions with Na-montmorillonite and formation of K-illite ($f$ [77]), a reaction that also consumes bicarbonate and releases acid as $CO_2$ ($f$ [78]). Steady state requirements also dictate that these Na- and K-phases ultimately be returned to the craton ($f$ [127], $f$ [124]), where they are reincorporated in primary silicates to start a new weathering cycle.

### *Organic Carbon Subcycle*

Organic matter cycling exerts a critical control on both long-term atmospheric $CO_2$ and $O_2$, and our model reflects our belief that net ecosystem production is ultimately limited by phosphorous availability (Smith and Mackenzie, 1987; Tyrrell, 1999). The controls on organic matter burial are also complex, and are described in the *Iron and Phosphorous Subcycle* (see below). Although the availability of organic matter in marine sediment also reflects the total sedimentation rate, primarily inputs of clastic detritus from terrestrial weathering (Canfield, 1991; Berner, 2004; Mackenzie and Lerman, 2006), the current model contains neither clastic weathering nor organic carbon inputs from land to the coastal ocean, and the primary influence of terrestrial weathering on the marine organic carbon cycle is through the supply of *inorganic* phosphorous (the apatite weathering flux, $f$ [19]). The control of the rate of marine organic matter fixation ($f$ [1]) closely follows the model of Van Cappellen and Ingall (1996), in which the rate is proportional (via $\gamma_{RR}$, the Redfield ratio) to $f$ [55], the rate of organic phosphorous uptake:

$$f[1] = \gamma_{RR} f[55] \tag{36}$$

The organic phosphorous flux is in turn a first order function of the mass of reactive inorganic phosphorous in the ocean ($y$[28]) and a rate function ($V_{MIX}$) that describes the ocean's ventilation rate:

$$f[55] = k[24]V_{MIX}y[28] \tag{37}$$

In all the runs described below, $V_{MIX}$ is fixed to a value of 3.0. In the steady state model, organic phosphorous fluxes are computed by dividing Quaternary organic carbon fluxes by 250 (table A1). This approach adopts Van Cappellen and Ingall's (1996) argument that C/P ratios vary from 200 for fully oxic to 4000 for completely anoxic sediments. The flux of organic material available for marine deposition, $f$ [54], is computed as

$$f[54] = k[24]f[1]^n \tag{38}$$

where $n = 2.5$ (Van Cappellen and Ingall, 1996), and the respiration flux ($f$ [3]) in turn is computed as the difference between ($f$ [1]) and ($f$ [54]). The net burial of organic material on the shelf ($f$ [56]) reflects the difference between $f$ [54], the flux of organic carbon oxidized in the formation of pyrite ( *viz.* $f$ [50]), in turn tied to reactive iron availability (described below), and the pelagic organic carbon flux, $f$ [57]. The partitioning of organic matter burial between shelf and pelagic regimes is currently fixed so that the shelf receives 95 percent of the total. Pelagic sedimentary organic carbon is eventually subducted and returned to the atmosphere ($f$ [108], ($f$ [114]).

The mass of organic carbon residing in shelf sediments ($y$[6]) may be rapidly recycled and returned as $CO_2$ ($f$ [20]):

$$f[20] = k[15]y[6] \tag{39}$$

In addition, we have provided for the development of burial of terrestrial organic matter in non marine basins ($f$ [21]) using an approach similar to that of Berner and Canfield (1989). We have used data derived from the organic carbon content of the rock record (Budyko and others, 1987) to calculate the total derivative ($c_{BU}(t)$) of this reservoir. This constraint and the assumption of a first order uplift-weathering flux ($f[48] = k[23]\ y[17]$) yield the required burial flux:

$$f[21] = c_{BU}(t) + f[48] \tag{40}$$

The cycling of organic carbon, coupled with sulfur and iron, results in large exchange fluxes involving atmospheric reservoirs of $CO_2$ and $O_2$ (table A2; eq A2, table A3). For purposes of clarity, we note that the balance of atmospheric oxygen reflects reactions in which it may not be directly involved as an oxidant. During photosynthesis, electrons lost during ATP and NADPH production are returned to chlorophyll via oxidation of water, yielding free oxygen; the chemical energy stored in ATP and NADPH is then used to convert $CO_2$ and water to sugars and carbohydrates (carbon fixation). A fraction of this organic carbon, after some transit through the food web, may ultimately be deposited as sedimentary organic matter. Subsequent consumption of this organic matter by aerobes will consume free oxygen, thus balancing the cycle. However, in anaerobic marine environments, this organic matter is commonly oxidized by bacterial sulfate reduction to yield dissolved $H_2S$. Over a complex subsequent reaction path(s) this dissolved sulfide will ultimately react to form pyrite, $FeS_2$. While the weathering of pyrite on land will consume oxygen, *burial* of pyrite actually represents oxygen accumulation in the atmosphere. However, this oxygen was originally produced during photosynthesis. This can be seen by recognizing that the sum of the *overall* reaction for sulfate reduction (eq 76′ is eq 76 (table 2) written on a per mol carbon basis without calcium),

$$\tfrac{2}{15}Fe_2O_3 + \tfrac{8}{15}SO_4^{2-} + (CH_2O) + \tfrac{16}{15}H^+ = \tfrac{4}{15}FeS_2 + CO_2 + \tfrac{23}{15}H_2O \tag{76$'$}$$

and pyrite oxidation (eq 78, table 2),

$$O_2 + \tfrac{4}{15}FeS_2 + \tfrac{8}{15}H_2O = \tfrac{2}{15}Fe_2O_3 + \tfrac{16}{15}H^+ + \tfrac{8}{15}SO_4^{2-} \tag{78$'$}$$

is oxidation of organic matter by oxygen:

$$O_2 + (CH_2O) = CO_2 + H_2O \quad (77)$$

Thus, there is no explicit term of pyrite burial in the oxygen balance (table A2 and eq A2), but the role of $FeS_2$ weathering in consuming oxygen and its formation representing oxygen accumulation in the atmosphere are an integral part of MAGic.

### *Sulfur Subcycle*

Sulfur is delivered to the ocean as sulfate derived from the weathering of pyrite

$$f[16] = k[14]y[14] \quad (41)$$

and the first order dissolution of evaporite minerals $CaSO_4$ and $MgSO_4$. Although the sulfuric acid released from pyrite oxidation participates in silicate and carbonate rock weathering reactions (eqs 5, 7, 9, 11, 29, and 31), the fluxes involved are minor compared to $CO_2$, and have no associated feedback functions. Sulfate reduction occurs both biogenically within shallow marine sediment and abiogenically during hydrothermal reaction between seawater and basalt, as mentioned above. The bicarbonate released in biogenic sulfate reduction is used to form calcite and dolomite. Reduced sulfur formed by these pathways is returned through uplift and exposure of marine sediments and through release of volcanic $H_2S$ and $SO_2$. Oxidation of this reduced sulfur thus completes the cycle, consuming the oxygen initially liberated by organic matter production, and yielding sulfuric acid for weathering.

### *Iron and Phosphorous Subcycle*

Iron and phosphorous cycling are closely linked to that of organic carbon and sulfur. Sedimentary phosphorous is represented as organic P, P bound with Fe oxyhydroxides, and apatite phases, and partitioned between shelf and pelagic environments. The rate of incorporation of P in organic matter, $f[55]$, is allowed to vary in proportion to the availability of so-called "reactive" phosphorous. The overall approach closely follows the model of Van Cappellen and Ingall (1996), which uses the ocean's overall oxidation state or "degree of anoxicity" (DOA) to represent the combined influence of the ocean's oxygen tension, primary production flux, and ventilation rate. DOA effectively parameterizes the coupling of iron and phosphorous governing the efficiency of sedimentary phosphorous release and recycling, the fraction of reactive iron present as reduced (pyrite) versus oxyhydroxide phases, and the C/P ratio of organic matter undergoing burial. This coupling yields a critical negative feedback control on atmospheric oxygen levels. If $PO_2$ becomes too high (as DOA approaches zero), then the phosphorous sorbed to reactive FeOOH undergoing deposition and burial will remain within the sediment, and its removal from seawater will limit productivity and allow $PO_2$ to fall. Conversely, if $PO_2$ becomes too low, for example, due to enhanced demand in the weathering of shelf organic matter, the increase in anoxia (as DOA approaches unity) will lead to a greater fraction of reactive iron being sulfidized. Loss of previously FeOOH-bound P to the water column will in turn increase productivity and $PO_2$.

## MODEL RESULTS AND DISCUSSION

Our MAGic model results and discussion are organized around a "standard" run. These standard run results have been achieved after considerable testing and variation of initial conditions and parameters, and come closest to returning agreement with the estimated masses of Quaternary reservoirs of the materials. However, we must stress that the *particular* solution to any model containing time-dependent coefficients and nonlinear interactions, despite guarantees of overall uniqueness and existence, is sensitive to the choice of initial conditions (Lasaga, 1981) and overall parameterization. In simple terms, we argue that it is difficult to use the recovery of modern conditions at $t = 0$ as an absolute criterion of the geologic relevance of a given solution. In addition, numerical instabilities or insufficient progress during iteration often prevented our obtaining a complete run from a given initial condition vector and parameter set, a reflection of the overall complexity and "stiffness" of the coupled differential equations in the initial value problem.

The standard run also contains basic assumptions concerning the partitioning between carbonate shelf and pelagic environments, the variation in seafloor spreading and other forcing functions, and the initial mass for pelagic carbonate at $t_0$ ($t = -514$ Ma). The parameter controlling pelagic/shelf sediment partitioning, $\beta(t)$, is set to vary with time according to the following rule:

$$\beta(t) = \{(0, t < -280), (0.282, -280 < \mathrm{t} < 0)\} \tag{42}$$

No initial pelagic carbonate is included in the standard run ($y[35] = 0$). The partitioning of pelagic carbonates between mantle subduction and metamorphic regimes is fixed at $\sigma = 0.393$, and seafloor spreading/degassing rate ($c_G(t)$) varies according to the same schedule as in GEOCARB III (Berner and Kothavala, 2001). The initial masses of atmospheric $CO_2$, seawater DIC and $PO_4$ were typically enhanced (relative $y[1]$, $y[21] > 1$; compare table A1) in all runs. These adjustments were found to be necessary to allow fast-cycling atmospheric carbon and seawater reservoirs to survive a "spin-up" period of rapid initial adjustment without depletion (see INTRODUCTION), during which time the model was permitted to essentially "cycle in place" (that is, no updating of $t$-dependent functions was performed), allowing an initial quasi-steady-state condition to develop. Note that these additions are trivial in comparison to the sedimentary masses (table A3). Initial masses of seawater magnesium and sulfate were chosen so as to yield molar ratios with respect to calcium consistent with the data of Lowenstein and others (2001). The results of the standard run are shown in figure 7.

### *Atmospheric $CO_2$ and the Basalt Carbonate Buffer*

Although formation of calcium carbonate within submarine basalt during basalt-seawater interaction has been recognized for years, most geochemical models of the ocean-atmosphere system have not dealt quantitatively with the role of these reactions in buffering atmospheric $CO_2$ through geologic time. Here we investigate this issue in some detail and conclude that the formation and subduction of this $CaCO_3$ is important to the long-term $CO_2$ balance of the atmosphere.

*MAGic standard run.*—The small mass and rapid cycling of atmospheric $CO_2$ make it sensitive to the combined fluctuations in the intensity of continental weathering, precipitation, dissolution, and decomposition of marine carbonates, reverse weathering reactions, seafloor basalt-seawater exchange, and fluxes associated with the production and remineralization of organic matter. Despite this composite signal, the overall pattern of atmospheric $CO_2$ distribution (fig. 7A), characterized by values that are broadly elevated throughout the early (pre-Carboniferous) Paleozoic and substantially reduced thereafter, is similar to that of GEOCARB III (for example, Berner and Kothavala, 2001, their fig. 5, p. 194). This pattern is an expected but not required outcome of the model, given the similar representation of chemical weathering in GEOCARB and MAGic, and most strongly reflects weakened weathering feedbacks imposed by the $c_E$ parameter. This parameter controls the effect of land plants on weathering and varies from zero to unity, with zero values representing no weathering feedback. In the MAGic model $c_E$ increases from an initial value of 0.1 to 0.2 during the initial appearance of land plants in the Devonian, from 0.2 to 0.75 during the

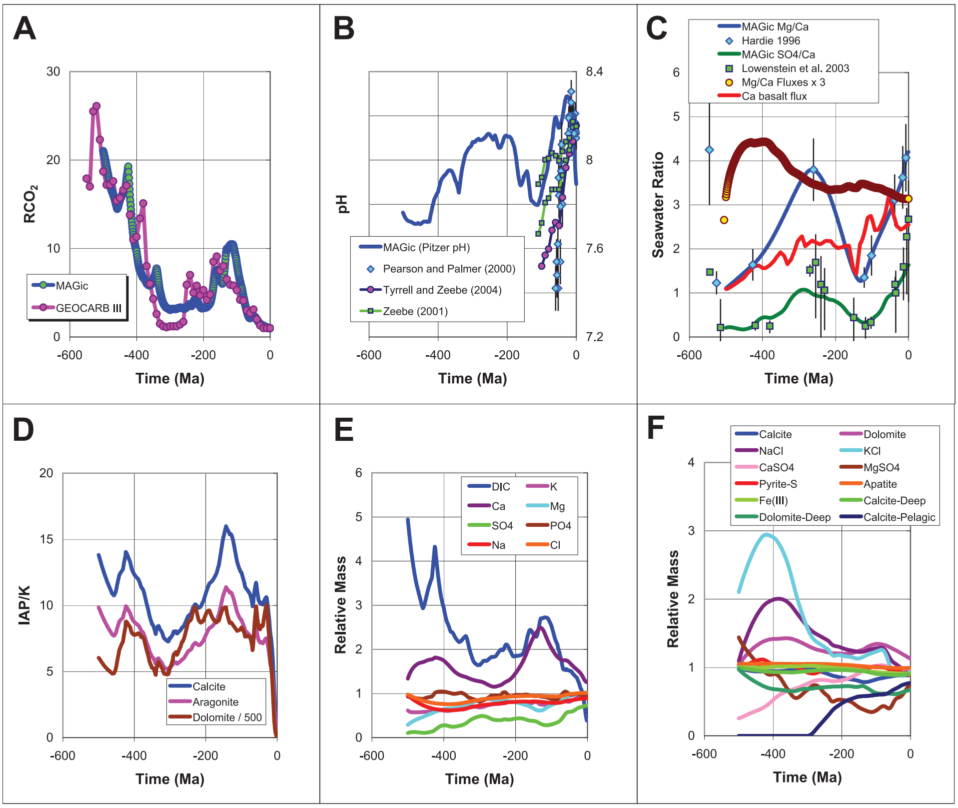

Fig. 7. MAGic standard run. (A) $RCO_2$ is $CO_2$ relative to steady state Quaternary concentrations, shown for MAGic (blue) versus GEOCARB (magenta; Berner and Kothavala, 2001) standard results. (B) MAGic (blue, no symbols) pH curve, computed using Pitzer routines from model DIC and $PCO_2$ data, compared with results from boron isotope proxy (published curve from Pearson and Palmer, 2000), and pH computed from paleoceanographic reconstructions (Tyrrell and Zeebe, 2004), and $\delta^{18}O$ data (Zeebe, 2001). (C) Model major ion seawater ratios Mg/Ca (blue) and $SO_4$/Ca (green) compared with published ratios from fluid inclusion data of Hardie (1996, blue diamonds) and Lowenstein and others (2003, green squares). Also shown are the ratio of model fluxes of magnesium uptake and calcium release from basalt (yellow-brown filled circles); net flux of calcium shown separately (red line). Note that ratio of fluxes is weakly out-of-phase with the concentration trends. (D) Saturation indices for carbonate minerals calcite (blue), aragonite (magenta), and dolomite (brown). Because $CO_2$-enforced temperature changes are relatively small, these changes primarily reflect trends in concentration. (E) Mass of seawater components, expressed relative to steady state values. Note stable behavior of potassium, large change in DIC, and trends in calcium versus magnesium. (F) Mass of sedimentary components, expressed relative to steady state values. Note evolution of pelagic calcite, as well as significant changes in the distribution of evaporites and dolomite.

Carboniferous, and from 0.75 to 1.0 during the rise of the angiosperms in the Cretaceous (Berner, 1991, 1994; Berner and Kothavala, 2001). Small $c_E$ values effectively dampen the hydrologic system's feedback response to elevated atmospheric $CO_2$ via weathering, and in turn permit further atmospheric $CO_2$ accumulations. This relationship is also clearly shown in figure 8A, which plots the value of the overall $CO_2$ feedback function ($fCO_2$), the land plant parameter ($c_E$), and the product of these terms as they appear in weathering rate constants. This latter product term remains below modern values until late in the Mesozoic. The total bicarbonate flux derived from weathering (expressed relative to Quaternary steady state) is also plotted, and although weathering rate coefficients reflect the action of other parameters (for

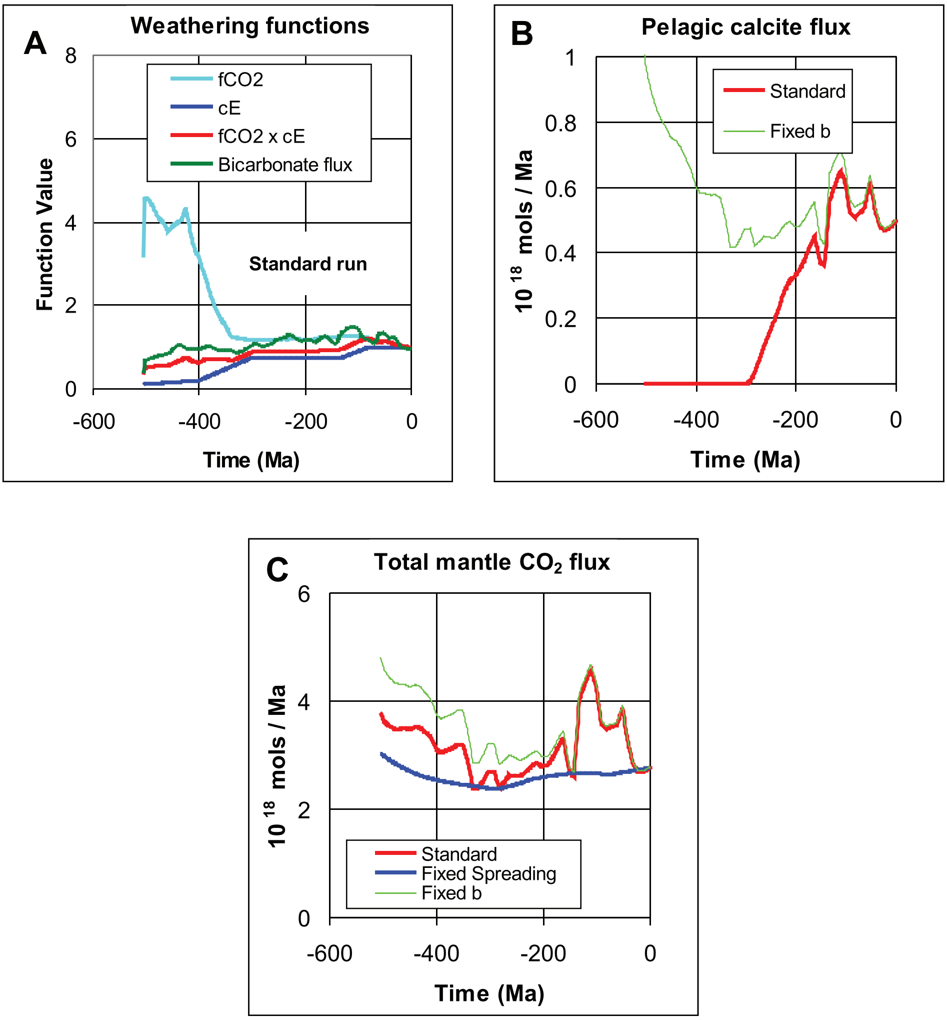

Fig. 8. Atmospheric trends, fluxes, and feedbacks. (A) Weathering feedbacks: $fCO_2$ (light blue curve) is a nonlinear function of atmospheric $CO_2$ that appears in all weathering fluxes for which carbonic acid is the titrant, without the additional explicit enhancements provided by temperature, runoff, and paleogeography, land plants, etc., computed from expressions described in Berner and Kothavala (2001); $fCO_2 \times c_E$ (red curve) is the product of this feedback function and $c_E$, the parameter representing the effect of land plants (dark blue curve); green curve is the total bicarbonate flux from weathering, expressed relative to its steady state value. Note that despite $fCO_2$ values that reflect the elevated $CO_2$ early in the Paleozoic, there is little actual enhancement of weathering due to strong suppression of this feedback by small values of land plant parameter ($c_E$). After $t \sim -300$ Ma, with $c_E$ at 75% of its present value, bicarbonate fluxes do increase substantially, reaching a maximum coinciding with high $CO_2$ degassing rates during the Cretaceous ($t \sim -100$ Ma). (B & C). Sensitivity comparison of pelagic (B) and total (C) fluxes for the standard run versus scenarios involved fixed spreading rates, and fixed partitioning (constant $\beta = \beta_0$ assumes pelagic carbonate has always been present). Note difference in *y*-scales between (B) and (C): although the pelagic subduction flux does become significant in the Mesozoic, this flux is relatively minor compared to that from subducted basaltic carbon. The distribution of basaltic carbon is controlled by the stoichiometry of major ion seawater-basalt uptake fluxes.

example, degassing, land area) as well, pre-Devonian weathering fluxes are on average less than those that follow.

A major result of our modeling effort is an enhanced insight into the relationship between atmospheric $CO_2$ and basalt-seawater exchange reactions involving calcium, magnesium, sodium, potassium, sulfate, and carbon. In our standard model run, we have represented the system such that the total flux of seawater calcium was apportioned as the sum of weathering, sulfate reduction, basalt fluxes, and net precipitation of carbonates and evaporites (that is, the difference between gross precipitation and diagenetic return fluxes). The total shelf + pelagic $CaCO_3$ precipitation flux, $f[93]$, is computed to be consistent with the *change* in the seawater concentration ratio $\boldsymbol{R}(t) \equiv \boldsymbol{c}_{Mg2+}/\boldsymbol{c}_{Ca2+}$, by using its derivative ($\boldsymbol{R}'$) (eq 18). In preliminary modeling efforts, we found it practical to either fix the basalt output flux of dissolved calcium equal to the uptake flux of dissolved magnesium, or to compute calcium output as proportional only to alkali uptake (Arvidson and others, 2006; see below). This is no longer the case: the implication that these fluxes represent a simple exchange reaction is problematic. The following discussion addresses this issue.

Mass balance constraints permit some simplifying assumptions. Submarine basalts are composed primarily of clinopyroxene and calcic plagioclase, and we shall assume that the free calcium introduced during hydrothermal basalt-seawater interaction reflects a reaction involving normative anorthite altering to a clay mineral, generically represented by the composition of the mineral kaolinite:

$$CaAl_2Si_2O_8 + 2H^+ + H_2O = Ca^{2+} + Al_2Si_2O_5(OH)_4 \tag{43}$$

Secondly, we shall assume that the net release of free $Ca^{2+}$ ion to seawater reflects a balance of the following reactions:

$$\tfrac{1}{2}Al_2Si_2O_5(OH)_4 + (Na^+, K^+) + 2SiO_2 = (K, Na)AlSi_3O_8 + \tfrac{1}{2}H_2O + H^+ \tag{44}$$

$$Mg^{2+} + \tfrac{1}{5}Al_2Si_2O_5(OH)_4 + \tfrac{1}{5}SiO_2 + \tfrac{7}{5}H_2O = \tfrac{1}{5}Mg_5Al_2Si_3O_{10}(OH)_8 + 2H^+ \tag{45}$$

$$SO_4^{2-} + 2H^+ + \tfrac{11}{2}Fe_2SiO_4 = \tfrac{1}{2}FeS_2 + \tfrac{7}{2}Fe_3O_4 + \tfrac{11}{2}SiO_2 + H_2O \tag{46}$$

These reactions, that is, "albitization" driven by seawater-supplied $Na^+$, $K^+$, and silica, the uptake of $Mg^{2+}$ to produce chlorite, and sulfate reduction in which an iron silicate (written here as $Fe_2SiO_4$) is the electron donor in the production of magnetite (Mottl and Holland, 1978), together determine the flux of calcium from anorthite decomposition.

Equations 43–46 combine below to form a master equation for the model basalt-seawater reaction, with their individual contributions proportional to the seawater concentrations of $Na^+$, $K^+$, $Mg^{2+}$, and $SO_4{}^{2-}$. These reactions differ most fundamentally in terms of consumption or production of protons. Scaling the last three reactions by the appropriate fluxes (for reference, $f_{Mg} = f[81]$, $f_{SO4} = f[82]$, and $f_{Na,K} = f[83,84]$),

$$f_{Na,K} \times (\tfrac{1}{2}Al_2Si_2O_5(OH)_4 + (Na^+, K^+) + 2SiO_2 \rightarrow (Na, K)AlSi_3O_8 + \tfrac{1}{2}H_2O + H^+) \tag{44$'$}$$

$$f_{Mg} \times (Mg^{2+} + \tfrac{1}{5}Al_2Si_2O_5(OH)_4 + \tfrac{1}{5}SiO_2 + \tfrac{7}{5}H_2O \rightarrow \tfrac{1}{5}Mg_5Al_2Si_3O_{10}(OH)_8 + 2H^+) \tag{45$'$}$$

$$f_{SO_4} \times (SO_4^{2-} + 2H^+ + \tfrac{11}{2}Fe_2SiO_4 \rightarrow \tfrac{1}{2}FeS_2 + \tfrac{7}{2}Fe_3O_4 + \tfrac{11}{2}SiO_2 + H_2O) \tag{46$'$}$$

and summing eqs 44′, 45′ and 46′ produces

$$\begin{aligned}
&f_{SO_4}SO_4^{2-} + f_{Mg}Mg^{2+} + f_{Na,K}(Na^+, K^+) + (\tfrac{7}{2}f_{Mg} - \tfrac{1}{2}f_{Na,K} - f_{SO_4})H_2O \\
&\quad + (\tfrac{1}{5}f_{Mg} + \tfrac{1}{2}f_{Na,K})Al_2Si_2O_5(OH)_4 + (2f_{Na,K} + \tfrac{1}{5}f_{Mg} - \tfrac{11}{2}f_{SO_4})SiO_2 \\
&\quad + \tfrac{11}{2}f_{SO_4}Fe_2SiO_4 = f_{Na,K}(Na,K)AlSi_3O_8 + f_{SO_4}(\tfrac{1}{2}FeS_2 + \tfrac{7}{2}Fe_3O_4) \\
&\quad + \tfrac{1}{5}f_{Mg}Mg_5Al_2Si_3O_{10}(OH)_8 + 2(f_{Mg} + \tfrac{1}{2}f_{Na,K} - f_{SO_4})H^+
\end{aligned} \tag{47a}$$

Writing anorthite decomposition using the acid produced above yields

$$\begin{aligned}
&2(f_{Mg} + \tfrac{1}{2}f_{Na,K} - f_{SO_4})H^+ + (f_{Mg} + \tfrac{1}{2}f_{Na,K} - f_{SO_4})CaAl_2Si_2O_8 + (f_{Mg} + \tfrac{1}{2}f_{Na,K} - f_{SO_4})H_2O \\
&\quad = (f_{Mg} + \tfrac{1}{2}f_{Na,K} - f_{SO_4})Ca^{2+} + (f_{Mg} + \tfrac{1}{2}f_{Na,K} - f_{SO_4})Al_2Si_2O_5(OH)_4
\end{aligned} \tag{47b}$$

The sum of these reactions (eqs 47a and 47b) yields

$$\begin{aligned}
&f_{SO_4}SO_4^{2-} + f_{Mg}Mg^{2+} + f_{Na,K}(Na^+, K^+) + (\tfrac{12}{5}f_{Mg} - 2f_{SO_4})H_2O \\
&\quad + (f_{Mg} + \tfrac{1}{2}f_{Na,K} - f_{SO_4})CaAl_2Si_2O_8 + (2f_{Na,K} + \tfrac{1}{5}f_{Mg} - \tfrac{11}{2}f_{SO_4})SiO_2 + \tfrac{11}{2}f_{SO_4}Fe_2SiO_4 \\
&\quad = (f_{Mg} + \tfrac{1}{2}f_{Na,K} - f_{SO_4})Ca^{2+} + f_{Na,K}(Na, K)AlSi_3O_8 + f_{SO_4}(\tfrac{1}{2}FeS_2 + \tfrac{7}{2}Fe_3O_4) \\
&\quad + \tfrac{1}{5}f_{Mg}Mg_5Al_2Si_3O_{10}(OH)_8 + (\tfrac{4}{5}f_{Mg} - f_{SO_4})Al_2Si_2O_5(OH)_4
\end{aligned} \tag{48}$$

It is clear from equation (48) that regardless of independent variations in the fluxes of sulfate, magnesium, sodium, and potassium, all of the acid required for anorthite decomposition is produced internally within the basalt. It is also clear that for magnesium and calcium uptake and release fluxes to be identical, the difference of $\frac{1}{2}$ $f_{Na,K}$ and $f_{SO4}$ must be zero. Such a condition would be entirely fortuitous, given that the uptake fluxes of sodium, potassium, magnesium, and sulfate, at least as they have been modeled, are independently proportional to their respective concentrations in seawater. Our steady state balance indicates that this is not currently the case ($\frac{1}{2}f_{Na,K} > f_{SO4}$), and the "excess" calcium released by anorthite decomposition must be returned to the basalt as a flux of (vein) calcite, $f_{BCC}$ ( $= f\,[94]$). To allow for the steady state balance of seawater magnesium and basalt calcium in the reaction above we must also add the scaled reaction,

$$f_{BCC} \times (Ca^{2+} + 2HCO_{3-} = CaCO_3 + H_2O + CO_2) \tag{49}$$

where the flux under the present-day steady state condition is $f_{BCC} = \frac{1}{2}f_{Na,K} - f_{SO4}$. These fluxes of $CO_2$ and bicarbonate are thus used as a way of accounting for proton exchange during albitization, chloritization, hydrothermal sulfate reduction, and anorthite decomposition reactions. The overall master basalt-seawater exchange reaction is thus,

$$\begin{aligned}
&f_{SO_4}SO_4^{2-} + f_{Mg}Mg^{2+} + f_{Na,K}(Na^+, K^+) + (\tfrac{12}{5}f_{Mg} - 2f_{SO_4} - f_{BCC})H_2O + 2f_{BCC}HCO_{3-} \\
&\quad + (f_{Mg} + \tfrac{1}{2}f_{Na,K} - f_{SO_4})CaAl_2Si_2O_8 + (2f_{Na,K} + \tfrac{1}{5}f_{Mg} - \tfrac{11}{2}f_{SO_4})SiO_2 + \tfrac{11}{2}f_{SO_4}Fe_2SiO_4 \\
&\quad = (f_{Mg} + \tfrac{1}{2}f_{Na,K} - f_{SO_4} - f_{BCC})Ca^{2+} + f_{Na,K}(Na, K)AlSi_3O_8 + f_{SO_4}(\tfrac{1}{2}FeS_2 + \tfrac{7}{2}Fe_3O_4) \\
&\quad + \tfrac{1}{5}f_{Mg}Mg_5Al_2Si_3O_{10}(OH)_8 + (\tfrac{4}{5}f_{Mg} - f_{SO_4})Al_2Si_2O_5(OH)_4 + f_{BCC}CaCO_3 + f_{BCC}CO_2
\end{aligned} \tag{50}$$

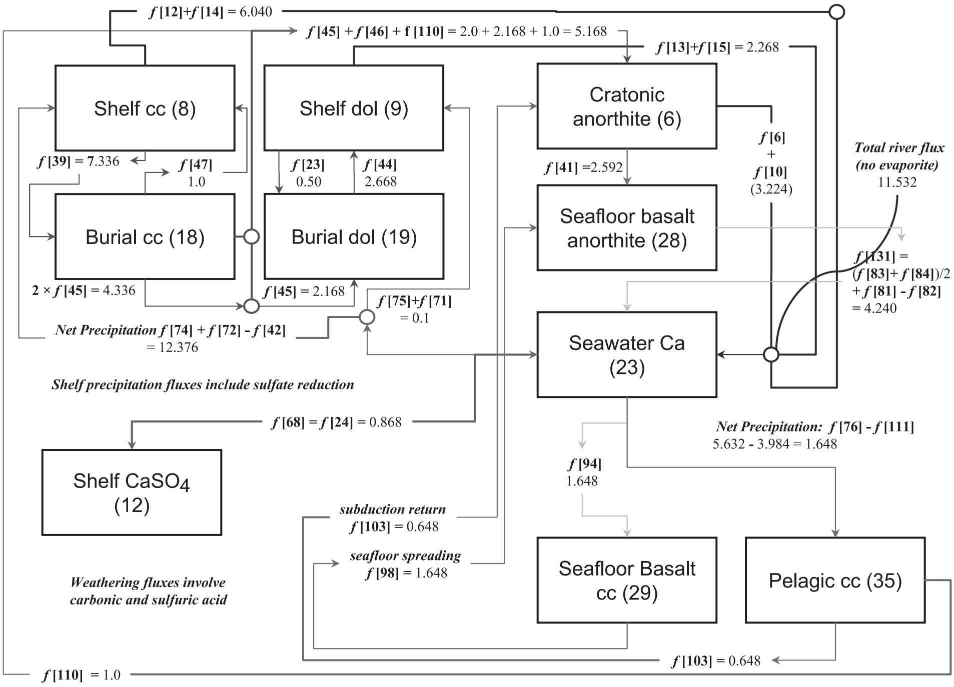

Fig. 9. Model topology and steady state fluxes for calcium, showing detailed exchanges between seawater calcium, basalt silicate and carbon reservoirs.

Calcite present within seafloor basalts has been previously recognized as an important carbon sink (Alt and Teagle, 1999); however, the strontium isotopic composition of the Sr in the $CaCO_3$ suggests some poorly known calcium contribution from the circulating seawater in the hydrothermal solution. The basalt calcite flux ($f_{BCC}$) thus links the ratio of Mg and Ca "exchange" fluxes to the seawater-atmosphere carbon system. The remaining issue is constraint of the basalt calcite flux as a function of time. For the time being, we have chosen to leave this flux at zero$^{th}$ order, thus scaling the rate coefficient ($k[48]$) in proportion to spreading rate, as has been done with the other uptake fluxes, but with no explicit concentration dependency. The net calcium flux to seawater ($f[96]$) can thus be taken directly from equation (50):

$$f[96] = f[81] + \tfrac{1}{2} \times (f[83] + f[84]) - f[82] - f[94] \qquad (51)$$

A detailed summary of steady state calcium fluxes for this system is provided in figure 9.

The observed variation in the ratio of these fluxes over time (fig. 7C) is not large and well within the uncertainty regarding their present day value. The ratio of fluxes appears to be weakly out-of-phase with the concentration ratio ($c_{Mg2+}/c_{Ca2+}$), showing its highest value during the early Phanerozoic and dipping during the concentration maxima of the late Paleozoic and present day. The small change in the ratio of fluxes reflects the relatively weak dependency noted above and constant mass of the basalt carbon reservoir. Attempts to provide greater forcing by making the basalt carbon flux dependent on seawater bicarbonate concentration led to large model instabilities, and further work is required to evaluate this sensitivity. As high spreading rates increase anorthite decomposition and calcium release, they also promote higher rates of basalt calcite formation, which in turn act to buffer excess calcium concentrations. Increases in spreading rate would also increase the $CO_2$ released by basalt calcite formation, as well as the $CO_2$ flux from subducted pelagic carbonate.

*Relationship to sulfate.*—In the extremely simplified reaction scheme suggested above, modulation of the basalt's calcium production comes about through sulfate as well as magnesium uptake. This suggests that the ratio of sulfate to calcium should bear a similar relationship to that of the ratio of magnesium to calcium. We can show this explicitly. At any time *t*, mass balance demands that

$$\begin{aligned}
&f\text{Mg},\mathit{weath} - f\text{Mg},\mathit{evap} - f\text{Mg},\mathit{basalt} - f\text{Mg},\mathit{dol} - (c_{\text{Mg}^{2+}}/\boldsymbol{c}_{\text{Ca}^{2+}}) \\
&\quad \times (f\text{Ca},\mathit{weath} - f\text{Ca},\mathit{evap} - f\text{Ca},\mathit{dol} - f\text{Ca},\mathit{shelf\ cc} - f\text{Ca},\mathit{pel\ cc} - f\text{Ca},\mathit{diag} \\
&\qquad - f\text{Ca},\mathit{basalt}) - \boldsymbol{c}_{\text{Ca}^{2+}} \times \boldsymbol{R}'(t) = 0. \qquad (52)
\end{aligned}$$

To clarify what are fluxes versus concentrations in this discussion, we note here that $\boldsymbol{c}_{\text{Mg2}+}$, $\boldsymbol{c}_{\text{Ca2}+}$, and $\boldsymbol{c}_{\text{SO4}^{2-}}$ are seawater concentration terms, the subscripts *cc, dol, evap, diag, pel, py, mSR,* and *weath* are shorthand for calcite, dolomite, evaporite, diagenetic, pelagic, pyrite, microbial sulfate reduction, and weathering fluxes, respectively, and the following identities prevail: $f\text{S-SO}_4\text{+S-pyr},\mathit{weath} = f\,[31]$, $f\text{SO}_4,\mathit{mSR} = f\,[50]$, $f\text{SO}_4,\mathit{basalt} = f\,[82]$, $f\text{Mg},\mathit{weath} = f\,[34]$, $f\text{Mg},\mathit{evap} = f\,[69]$, $f\text{Mg},\mathit{basalt} = f\,[81]$, $f\text{Mg},\mathit{dol} = f\text{Ca},\mathit{dol} = f[71] + f[75]$, $f\text{Mg},\mathit{RW} = f[79]$, $f\text{Ca},\mathit{weath} = f[33]$, $f\text{Ca},\mathit{shelf\,cc} = f\,[72] + f\,[74]$, $f\text{Ca},\mathit{pel\ cc} = f\,[76]$, $f\text{Ca},\mathit{diag} = f\,[42] + f\,[111]$, $f\text{Ca},\mathit{evap} = f\,[68]$; $f\text{Ca},\mathit{basalt} = f\,[96]$ refers to the *net* calcium flux from basalt-seawater interaction (see table A1). In the same way we have defined $\boldsymbol{R} \equiv \boldsymbol{c}_{\text{Mg2}+}/\boldsymbol{c}_{\text{Ca2}+}$ seawater ratio, we define $\boldsymbol{Q} \equiv \boldsymbol{c}_{\text{SO4}^{2-}}/\boldsymbol{c}_{\text{Ca2}+}$. Differentiating this ratio as a function of time and introducing this derivative in the balance of fluxes provides,

$$\begin{aligned}
&f\text{S-SO}_4 + \text{S-pyr},\mathit{weath} - f\text{SO}_4,\mathit{mSR} - f\text{Mg},\mathit{evap} - f\text{Ca},\mathit{evap} - f\text{SO}_4,\mathit{basalt} - (\boldsymbol{c}_{\text{SO}_4^{2-}}/\boldsymbol{c}_{\text{Ca}^{2+}}) \\
&\quad \times (f\text{Ca},\mathit{weath} - f\text{Ca},\mathit{dol} - f\text{Ca},\mathit{evap} - f\text{Ca},\mathit{shelf\ cc} - f\text{Ca},\mathit{pel\ cc} + f\text{Ca},\mathit{diag} \\
&\qquad + f\text{Ca},\mathit{basalt}) - \boldsymbol{c}_{\text{Ca}^{2+}} \times \boldsymbol{Q}'(t) = 0. \qquad (53)
\end{aligned}$$

For the basalt flux of calcium (expressed as a positive, input flux to seawater) to be consistent with the above expressions, the following must also be true:

$$\begin{aligned}
&f\text{Ca},\mathit{basalt} = (\boldsymbol{c}_{\text{Ca}^{2+}}/\boldsymbol{c}_{\text{Mg}^{2+}}) - (f\text{Mg},\mathit{weath} - f\text{Mg},\mathit{evap} - f\text{Mg},\mathit{basalt} - f\text{Mg},\mathit{RW} \\
&\quad - f\text{Mg},\mathit{dol}) - (f\text{Ca},\mathit{weath} - f\text{Ca},\mathit{dol} - f\text{Ca},\mathit{evap} - f\text{Ca},\mathit{shelf\ cc} - f\text{Ca},\mathit{pel\ cc} + f\text{Ca},\mathit{diag}) \\
&\quad - (\boldsymbol{c}_{\text{Ca}^{2+}}/\boldsymbol{c}_{\text{Mg}^{2+}}) \times \boldsymbol{c}_{\text{Ca}^{2+}}\boldsymbol{R}'(t) = (\boldsymbol{c}_{\text{Ca}^{2+}}/\boldsymbol{c}_{\text{SO}_4^{2-}}) \times (\boldsymbol{f}\text{S-SO}_4 + \text{S-pyr},\mathit{weath} - f\text{SO}_4,\mathit{mSR} \\
&\quad - f\text{Mg},\mathit{evap} - f\text{Ca},\mathit{evap} - f\text{SO}_4,\mathit{basalt}) - (f\text{Ca},\mathit{weath} - f\text{Ca},\mathit{dol} - f\text{Ca},\mathit{evap} \\
&\quad - f\text{Ca},\mathit{shelf\ cc} - f\text{Ca},\mathit{pel\ cc} + f\text{Ca},\mathit{diag}) - (\boldsymbol{c}_{\text{Ca}^{2+}}/\boldsymbol{c}_{\text{SO}_4^{2-}}) \times \boldsymbol{C}_{\text{Ca}^{2+}} \times \boldsymbol{Q}'(t) \qquad (54)
\end{aligned}$$

Combining these equations, canceling cross terms and simplifying provides the following relationship:

$$\begin{aligned}
&(\boldsymbol{c}_{\text{SO}_4^{2-}}/\boldsymbol{c}_{\text{Ca}^{2+}})(\boldsymbol{f}\text{Mg},\mathit{weath} - f\text{Mg},\mathit{evap} - f\text{Mg},\mathit{RW} - f\text{Mg},\mathit{basalt} - f\text{Mg},\mathit{dol} - \boldsymbol{c}_{\text{Ca}^{2+}} \times \boldsymbol{R}'(t)) \\
&\quad = (\boldsymbol{c}_{\text{Mg}^{2+}}/\boldsymbol{c}_{\text{Ca}^{2+}})(f\text{S-SO}_4 + \text{S-pyr},\mathit{weath} - f\text{SO}_2,\mathit{mSR} - f\text{Mg},\mathit{evap} \\
&\qquad - f\text{Ca},\mathit{evap} - f\text{SO}_4\mathit{basalt} - \boldsymbol{c}_{\text{Ca}^{2+}} \times \boldsymbol{Q}'(t)) \qquad (55)
\end{aligned}$$

The derivative terms vanish at steady state, and because masses must be positive, the balance of fluxes for both right and left hand sides of the above equation must have the same sign. Our point here is that exchange reactions with the basalt, at least as they have been described above, coupled with the various weathering and precipitation fluxes link these observable ratios in a simple proportionality, and suggest that they should track one another. This conclusion is indeed borne out by figure 7C, which shows that the variation in $\boldsymbol{c}_{\mathrm{Mg2+}}/\boldsymbol{c}_{\mathrm{Ca2+}}$ and $\boldsymbol{c}_{\mathrm{SO_4}^{2-}}/\boldsymbol{c}_{\mathrm{Ca2+}}$ are roughly comparable, and in good agreement with the $\boldsymbol{c}_{\mathrm{SO4^{2-}}}$ / $\boldsymbol{c}_{\mathrm{Ca2+}}$ ratio taken from the fluid inclusion data of Lowenstein and others (2001).

In the standard run (fig. 7), precipitation fluxes to the evaporite reservoirs (NaCl, KCl, $CaSO_4$, $MgSO_4$) are computed to be proportional to their ion concentration products and scaled by the extent of continental flooding. In the current state of the model's development, we have not provided for the fact that major evaporite deposits may reflect episodic and exceedingly rapid rates of accumulation (Holser, 1984). In this respect, Quaternary environments may provide few model analogs for past episodes of large scale evaporite formation. In this case, the $(\boldsymbol{c}_{\mathrm{SO_4}^{2-}}/\ \boldsymbol{c}_{\mathrm{Ca2+}})'$ term provides a means of solving for the evaporative flux to the $CaSO_4$ reservoir ($f$Ca,*evap* = $f$[68]) consistent with other constraints:

$$
\begin{aligned}
f[68] = {} & (f\text{S-SO}_4 + \text{S-pyr},\mathit{weath} - f\text{SO}_4,\mathit{mSR} - f\text{Mg},\mathit{evap} - f\text{SO}_4,\mathit{basalt}) - \boldsymbol{c}_{\mathrm{Ca}^{2+}} \times \boldsymbol{Q}'(t) \\
& + (\boldsymbol{c}_{\mathrm{SO}_4^{2-}}/\boldsymbol{c}_{\mathrm{Mg}^{2+}}) \times \boldsymbol{c}_{\mathrm{Ca}^{2+}} \times \boldsymbol{R}'(t) - (f\text{Mg},\mathit{weath} - f\text{Mg},\mathit{basalt} - f\text{Mg},\mathit{dol} - f\text{Mg},\mathit{evap} \\
& - f\text{Mg},\mathit{RW}) = (f[31] - f[50] - f[69] - f[82]) - y[23] \times \boldsymbol{Q}'(t) + (y[26]/y[24]) \times y[23] \\
& \times \boldsymbol{R}'(t) - (f[34] - f[81] - f[75] - f[71] - f[69] - f[79]) \qquad (56)
\end{aligned}
$$

Although the model produces the expected close agreement between the data of Lowenstein and others (2001) with equation (55), the strong tandem increases in $\boldsymbol{c}_{\mathrm{Mg2+}}/\boldsymbol{c}_{\mathrm{Ca2+}}$ and $\boldsymbol{c}_{\mathrm{SO_4}^{2-}}/\boldsymbol{c}_{\mathrm{Ca2+}}$ at $t > -100$ Ma are apparently inconsistent with the remaining matrix of constraints, to the extent that the system imposes a sufficiently strong demand on DIC to deplete this component by $t \sim -30$ Ma (fig. 10C).

This model instability may signify a possible mismatch in the balance of calculated fluxes (eq 55), for example, an overestimate of the strength of dolomitization or reverse weathering. More importantly, this result underscores the linkage between seafloor-mediated fluxes and the carbon budget, and in general also goes to the issue of consistency between fluid inclusion and other constraint data, a notion that was a central motivation for the model itself. Tandem increases in $\boldsymbol{c}_{\mathrm{Mg2+}}/\boldsymbol{c}_{\mathrm{Ca2+}}$ and $\boldsymbol{c}_{\mathrm{SO_4}^{2-}}/\boldsymbol{c}_{\mathrm{Ca2+}}$ concentration ratios are generally tied to reciprocal *decreases* in DIC (compare figs. 7C and 7E). For example, in figure 7E DIC decreases from a maximum during the rise in $\boldsymbol{c}_{\mathrm{Mg2+}}/\boldsymbol{c}_{\mathrm{Ca2+}}$ and $\boldsymbol{c}_{\mathrm{SO_4}^{2-}}/\boldsymbol{c}_{\mathrm{Ca2+}}$ over the period −430 Ma to −260 Ma. Although DIC also decreases from a maximum during the later rise in $\boldsymbol{c}_{\mathrm{Mg2+}}/\boldsymbol{c}_{\mathrm{Ca2+}}$ and $\boldsymbol{c}_{\mathrm{SO_4}^{2-}}/\boldsymbol{c}_{\mathrm{Ca2+}}$ during −120 Ma to present, the starting maximum for this leg is substantially less than the earlier one.

The variations in the $CaSO_4$-$MgSO_4$ system in many ways resemble the trends in the calcite-dolomite system (described below), and the formation of both are also proportional to the extent of continental flooding. Increasing sulfate concentrations (required to satisfy the ratio constraint) also decrease the calcium output from the basalt (eq 50), an effect that should in turn reduce the demand for total sedimentary calcite precipitation (eq 18), and place less demand on DIC. However, these relationships are weakened by the concomitant decrease in seafloor spreading rates from $t = -100$ Ma to present. In addition, the changes in evaporite flux required by the constraint are large and rapid (fig. 11), which becomes negative at $t > -20$ Ma ($CaSO_4$ dissolution). Once evaporite dissolution begins, the increase in seawater calcium concentration drives $CaCO_3$ precipitation rates (eq 18), rapidly depleting DIC at a time when concentrations are relatively low compared to average Phanerozoic values. This instability may also reflect a competition for alkalinity imposed by Mesozoic-Cenozoic pelagic biogenic carbonate formation, a competition that is minimally

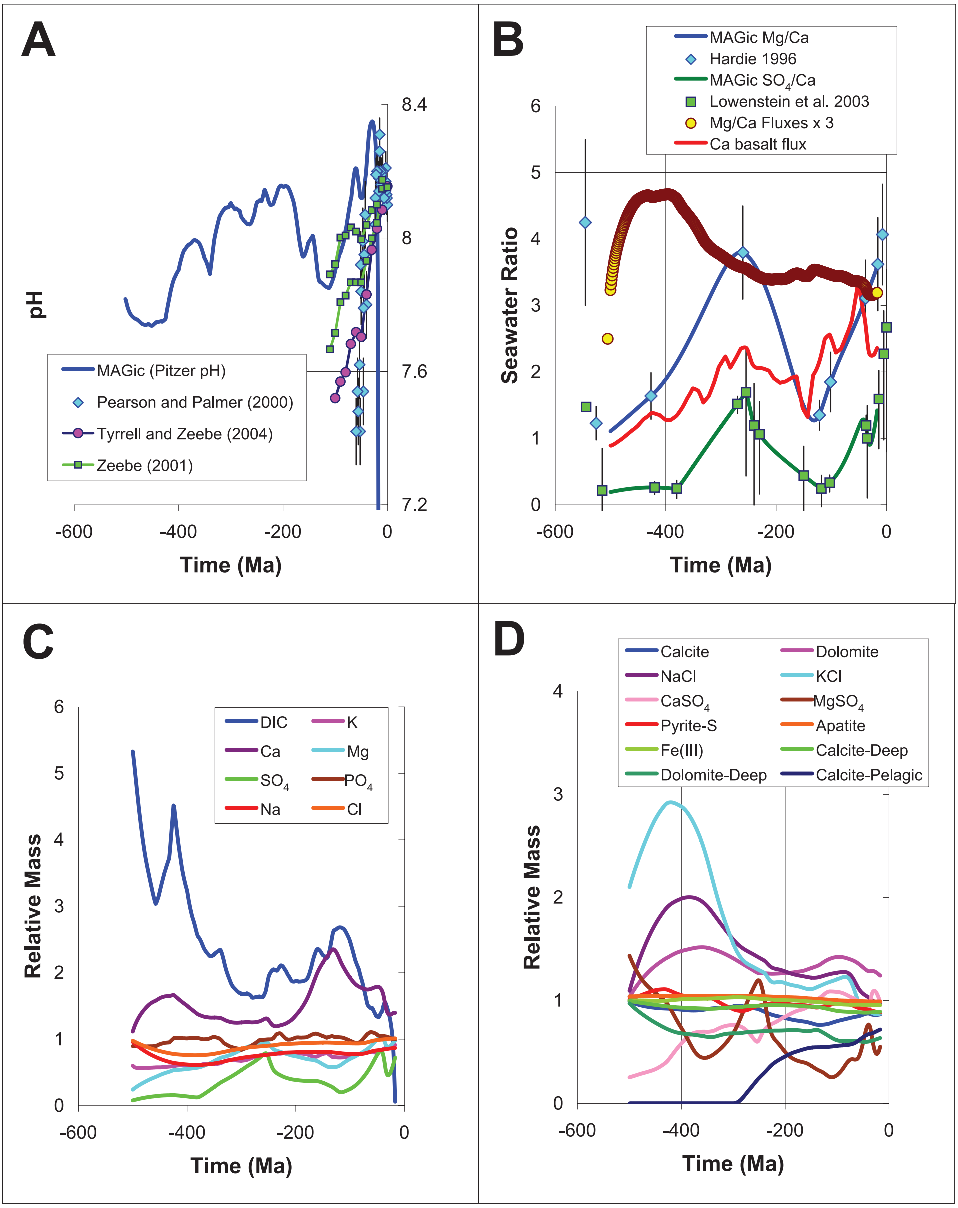

Fig. 10. Model results using fluid inclusion constraint curves to compute $CaSO_4$ fluxes. Results in (A) pH, (B) major ion ratios, (C) seawater, and (D) sedimentary components are similar to those of the standard run (fig. 7). Introduction of this constraint induces a large model instability, resulting in rapid depletion of DIC at $t > \sim -20$ Ma.

present or absent entirely during the Paleozoic. Clearly, this result suggests the need for a more detailed treatment of these fluxes.

Equation (55) suggests that times of high $\boldsymbol{c}_{Mg2+}/\boldsymbol{c}_{Ca2+}$ ratio should also be times of high sulfate as well. However, the response of the carbon system is dependent on the balance between magnesium and alkali uptake, both of which produce acid and drive

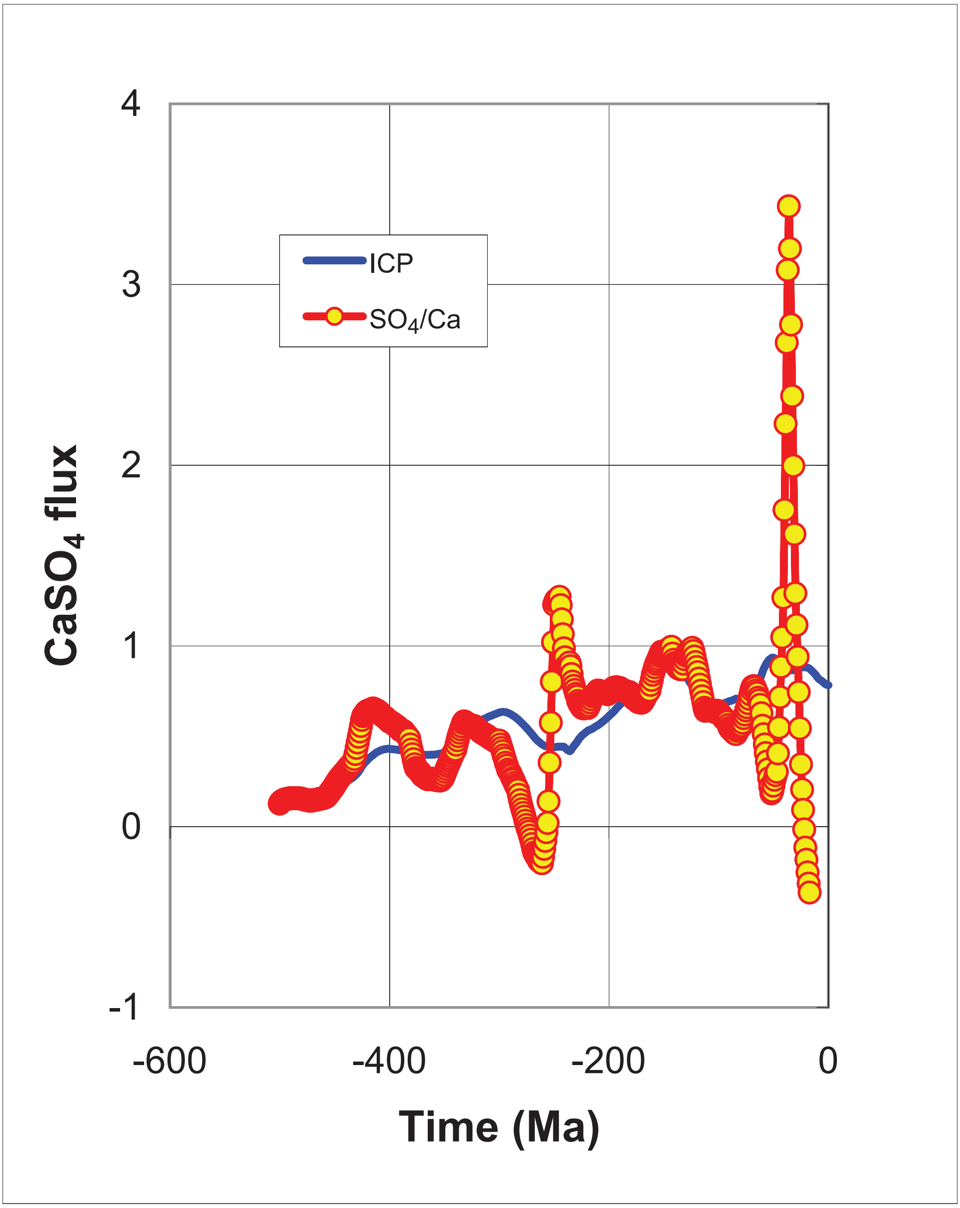

Fig. 11. $CaSO_4$ fluxes. Comparison of fluxes computed via the standard model formulation (blue line, where precipitation rate varies as the ion concentration product ICP $\equiv [Ca^{2+}] \times [SO_4{}^{2-}]$) versus an explicit dependence on the variation in the $SO_4$/Ca ratio of fluid inclusions (filled circles).

anorthite decomposition, and sulfate uptake, which produces bicarbonate. If at some time $t$, $c_{Mg2+}(t)/c_{Mg2+}(t = 0) >> c_{SO_4{}^{2-}}(t)/c_{SO_4{}^{2-}}(t = 0)$, then "excess" magnesium uptake will result in acid ($CO_2$) production in excess of that balanced by bicarbonate production. Conversely, if $c_{Mg2+}(t)/c_{Mg2+}(t = 0) << c_{SO_4{}^{2-}}(t)/c_{SO_4{}^{2-}}(t = 0)$, then $CO_2$ would be consumed and seawater pH should increase as a result. Moreover, these relationships are reinforced by links to the oxidation of organic carbon. Because total seawater sulfate is consumed in both the hydrothermal production of basalt pyrite and its low-temperature microbial equivalent during the anaerobic oxidation of organic matter, periods of high productivity ($CO_2$ consumption), organic matter burial, and biogenic sulfate reduction would also tend to limit sulfate uptake by the basalt, and thus lower $CO_2$ demand at the ridge itself. These relationships are complicated by the exchange of sodium for potassium and demands for seawater magnesium made during reverse weathering reactions, discussed below.

*The role of spreading rate.*—Spreading rate (accretion rate) has recently been brought into contention as a major control on ocean and atmospheric composition, at last during the past 150 Ma (Rowley, 2002). Here we investigate the role of spreading rate on various parameters of the ocean-atmosphere system. In general, the MAGic model runs highlight the sensitivity of the overall atmosphere-seawater carbon system to seawater-basalt exchange reactions. This sensitivity can also be evaluated by examining the influence of seafloor spreading rate variability, as the balance of fluxes of major ions to which carbon is tied is also controlled by the extent to which the coefficients $k[i]$ that scale these fluxes are enhanced (eq. 3). The "degassing" rate was a major control on atmospheric $CO_2$ in the original BLAG model (Berner and others, 1983; Lasaga and others, 1985), and to a lesser extent in the later GEOCARB models (Berner and Kothavala, 2001). A fixed spreading rate is achieved simply by holding the degassing parameter constant ($c_G = 1$) for the entire run. All other initial conditions and parameters are the same as in previous runs. The results of this sensitivity analysis are shown in figure 12. Although the overall pattern of $CO_2$ change is somewhat similar to previous runs in which $c_G$ is allowed to vary as a function of time, it is clear that fixed spreading rates result in lower $PCO_2$ values. The reduction in atmospheric $CO_2$ results in higher seawater pH, suppressed feedback, lower rates of chemical weathering, and thus lower DIC, alkalinity, and carbonate mineral saturation states. However, this difference is limited to the Paleozoic, as the differences between variable versus fixed $c_G$ are negligible during the Mesozoic, that is, after $c_E$ has reached 75 percent of its modern value.

In a steady state system, subduction of pelagic calcium carbonate and release of $CO_2$ replaces the carbonic acid consumed in the weathering of primary silicate minerals. However, this supply of pelagic carbonate may not have been constant with respect to time. A transition in the locus of carbonate sediment deposition would have important implications for carbon cycling. Prior to the advent of significant pelagic carbonate accumulation in the late Mesozoic (Boss and Wilkinson, 1991), the only return route for $CO_2$ to the atmosphere may have been through burial of carbonate sediments and eventual release during metamorphic decarbonation reactions. The absence of this return route may have partially decoupled climate regulation by $CO_2$ (for example, Veizer and others, 2000; Shaviv and Veizer, 2003). In addition, Schrag (2002) has argued that the current large mismatch in carbonate burial and $CO_2$ volcanic fluxes suggests that they may only be in phase during certain periods, and that the periodicity in the record reflects oscillatory cycling of sediment between the shelf and pelagic environments. We have examined this effect by holding $\beta(t)$, the parameter that controls whether carbonate sediment is precipitated in shelf versus pelagic environments, constant, using an initial pelagic mass equivalent to the present day (fig. 12, "Fixed $\beta$").

However, our model results also suggest that carbonate residing within the basalt as a result of the reactions described above is at least of equal importance compared to the pelagic calcite reservoir as a control on atmospheric $CO_2$. $CO_2$ derived from the subduction of pelagic carbonate sediment alone contributes less than a quarter of the total mantle flux of carbon returned to the atmosphere (the sum of pelagic and

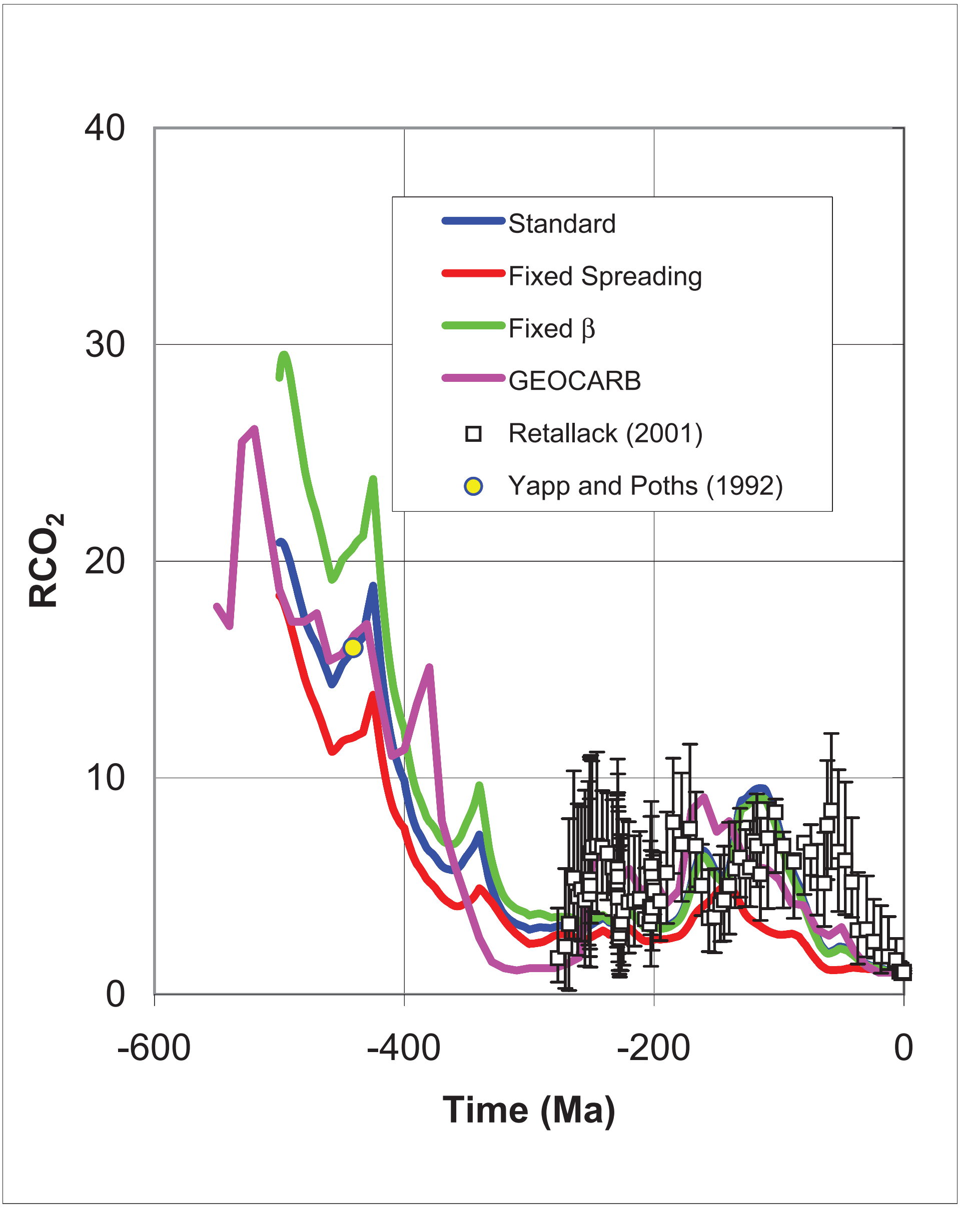

Fig. 12. Comparison of model atmospheric $CO_2$ concentrations (expressed as relative concentrations) in the standard run with scenarios involved fixed spreading rate and fixed partitioning between shelf and pelagic regimes. Also shown for comparison are model data from GEOCARB III (Berner and Kothavala, 2001), and proxy concentrations from Retallack (2001, open squares) and Yapp and Poths (1992, blue-yellow circle).

basaltic carbonate and organic matter). This relationship holds regardless of whether spreading rate or partitioning is varied or held constant (figs. 8B and 8C).

Holding spreading rate constant also results in a significant reduction in the variation in atmospheric oxygen during the Cretaceous (fig. 8D). This result reflects reduction in the weathering flux of inorganic phosphorous, and a reduction in primary productivity. This effect may be partially offset by the fact that a co-reduction in the weathering flux of ferric iron to the sediment requires that less phosphorous be sequestered in iron oxyhydroxide phases, and thus more phosphorous will be released back to the water column and be available for organic matter production. Oxygen and productivity relationships are discussed in more detail below.

### *Dolomite Distribution and Reverse Weathering*

As noted in Arvidson and Mackenzie (1999), part of the original motivation for this model was to develop a more quantitative understanding of long term geochemical controls on dolomite distribution. In MAGic, dolomite can form in one of two localities: in shallow water sediments that are also available for weathering, and in higher temperature burial environments where magnesium is supplied by the reaction of Mg-bearing clays with $CaCO_3$ (Hutcheon and others, 1980; Mackenzie and Pigott, 1981; also table 3, compare eq 66):

$$\mathrm{Mg_5Al_2Si_3O_{10}(OH)_8 + 5CaCO_3 + 5CO_2} \\ \mathrm{= 5CaMg(CO_3)_2 + Al_2Si_2O_5(OH)_4 + SiO_2 + 2H_2O} \quad (57)$$

To minimize complexity, we chose to ignore certain aspects of dolomite formation for which understanding is poor. For example, it is possible that precipitation rate of shallow water dolomite, although driven by changes in saturation state, may actually be favored by conditions that in turn limit the growth of other carbonates that compete for carbonate alkalinity. Such conditions could arise for example through undersaturation with respect to these competing phases, or during periods of elevated magnesium to calcium ratios. At the same time, we also wanted to evaluate the potential for reverse weathering as a sink for magnesium relative to basalt uptake and dolomite precipitation.

The results are summarized for the standard run in figure 13. Dolomite distribution shows an overall cyclic pattern, in which magnesium uptake to the shelf dolomite reservoir is actually favored during periods of elevated seafloor spreading, when absolute magnesium concentrations are simultaneously moderately depressed (low $\boldsymbol{c}_{\mathrm{Mg2+}}/\ \boldsymbol{c}_{\mathrm{Ca2+}}$, figs. 7C and 7E). This complementary pattern must reflect the stronger negative feedback on magnesium removal to the silicate sink, which both limits basalt uptake as concentrations drop, while at the same time leading to elevated carbonate alkalinity and carbonate mineral saturation indices as a result of enhanced continental weathering. Herein the MAGic model demonstrates the strong influence of both weathering and basalt-seawater reactions on ocean chemistry. Shallow water dolomite is thus favored during periods of fast spreading, with precipitation fluxes apparently superseding basalt uptake. Conversely, periods of slow spreading (associated with lower $CO_2$ and global temperatures) produce attenuated weathering inputs, allowing seawater magnesium to accumulate and thus drive enhanced basalt uptake, but at the same time produce meager dolomite accumulation rates due to relative suppression of saturation indices (fig. 7D). This general result, however, hinges on the correctness of our treatment of the weak or absent dependency of basalt-carbon uptake to bicarbonate itself, in other words that this uptake is dependent only on the concentrations of the remaining major electrolytes.

There are also important environmental controls on dolomite formation that the model in its current form does not accommodate. For example, Arvidson and Mackenzie (1997) and Arvidson and others (2000) showed that the abundance of dolomite as a sedimentary phase over time was highly sensitive to coupled variations in temperature and the expansion of shallow seafloor during periods of epeiric invasions of inland seas. Invasion of low-relief marginal basins appropriately situated in subtropical latitudes during periods of sustained higher temperatures, low humidity, and anti-estuarine circulation, could easily form restricted environments similar to modern, dolomite "factories" such as the Persian Gulf sabkha or the Coorong of South

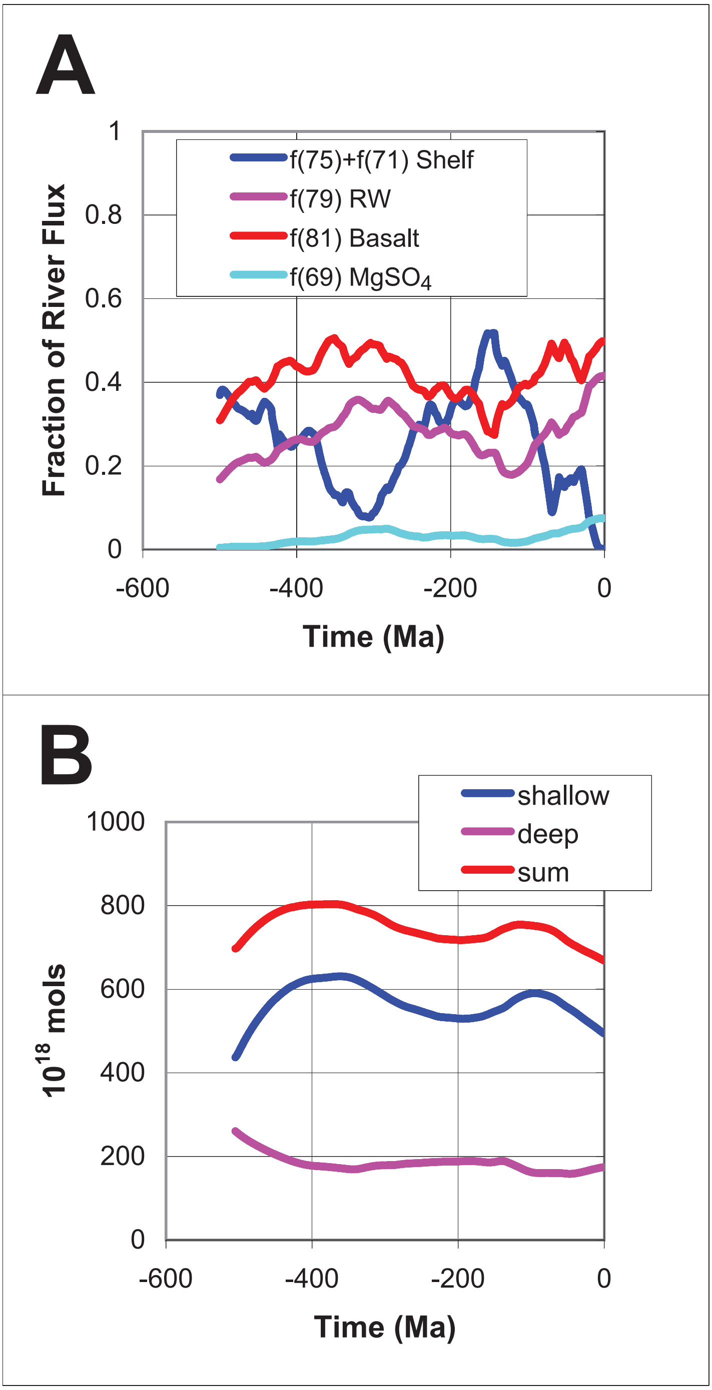

Fig. 13. Trends in magnesium fluxes and dolomite distribution. (A) Magnesium fluxes as a function of total river input. Note variation in shallow marine dolomite fluxes (*f*[75] + *f*[71], blue) is antithetic to that expressed by silicate uptake fluxes, both with respect to basalt (*f*[81], red) and reverse weathering sinks (*f*[79], magenta). (B) Variation in dolomite mass between the shallow marine (blue) versus deep burial dolomite reservoir (magenta).

Australia. Low latitude, shallow water environments prevailing from the early Paleozoic through late Mesozoic, where dolomite may have formed as a syndepositional or early diagenetic precipitate, have also largely disappeared in post-Tertiary time. In its current form, the model lacks sufficient detail to evaluate these factors. Lastly, it should be recognized that Phanerozoic changes in $\boldsymbol{c}_{\mathrm{Mg2+}}/\boldsymbol{c}_{\mathrm{Ca2+}}$ are expressions of relative variations in *calcium* much more than magnesium (fig. 7E).

With these important caveats in mind, the results of figure 13 are nonetheless entirely consistent with the observed mass-age relationships of sedimentary carbonate rocks (Given and Wilkinson, 1987; Wilkinson and Walker, 1989; Mackenzie and Morse, 1992; Walker and others, 2002). However, our findings are also inconsistent with the interpretation of the dolomite mass-age curve put forth by Holland and Zimmermann (2000), who suggest, based mainly on the Russian Platform dolomite distribution with depth (age), that dolomite abundance increases monotonically with increasing rock age in the Phanerozoic. Burial dolomite is also driven by seawater magnesium uptake, but via reverse weathering reactions that limit the production of Mg-bearing chlorite at low temperature. Burial dolomite thus tends to vary inversely with shallow shelf dolomite distribution, forming as a result of transfer from the shallow shelf reservoir as well as reaction of $CaCO_3$ with mafic silicates. Because magnesium (and potassium) uptake in reverse weathering reactions are assumed to be free of dependencies on bicarbonate concentrations, these low temperature fluxes have trends similar to their high temperature counterparts involving basalt. The lack of variation in potassium over time is unique (fig. 7E). Overall variations in basalt, reverse weathering ($Na^+/K^+$ exchange), and evaporite fluxes as a fraction of the river flux of dissolved potassium are small: 6 percent, 0.5 percent, and 0.6 percent, respectively. This stability indicates that potassium concentrations in seawater are extremely well buffered by both "albitization" reactions with basalt as well as lower temperature reverse weathering exchange.

### *Productivity, Phosphorus, and Carbon Burial*

Our standard run model shows that long term marine productivity has a strong dependence on the flux of phosphorous (apatite) weathering. This is shown in figure 14A, which indicates that the net flux of fixed marine organic carbon ($f[54]$) varies in close concert with the total phosphorous weathering flux ($f\,[19]$) throughout the Mesozoic and Cenozoic. This increase in productivity and marine organic carbon burial also gives rise to an increase in free oxygen (fig. 14B). As described in the section on the *Organic Carbon Subcycle*, net oxygen production ( $f\,[1] - f\,[3]$ ) is ultimately a power function of the mass of the reactive phosphorous pool. As shown in figure 14A, the DOA function (Van Cappellen and Ingall, 1996), which controls the C/P ratio of buried organic matter and the fraction of the reactive iron pool to be sulfidized,

$$\mathrm{DOA} = 1 - k[1] \times \mathrm{V_{MIX}} \times y[2]/f[1] \tag{58}$$

is inversely tied to atmospheric oxygen ($y\,[2]$), and thus acts as a strong brake on the growth of this reservoir during periods of high marine productivity and carbon burial.

In general, we found a progressive increase in oxygen over the entire model run, consistent with the overall growth over the Phanerozoic in size and diversity of plant biomass and storage of organic carbon in sediments (for example, Martin, 1996; Rothman, 2001). Although we found the buffering on atmospheric oxygen, as described above, to be quite strong, our total oxygen curve is within the error limits of Berner and Canfield's (1989) curve for the period $t > \sim -100$ Ma (fig. 14B), albeit somewhat higher than the model results of Berner (2001) and Hansen and Wallmann (2003). In the model of Berner and Canfield (1989; see also Berner and others, 2000, 2003), atmospheric oxygen was calculated by solving equations for the burial and oxidation fluxes of organic carbon and sulfur. Data describing the Phanerozoic

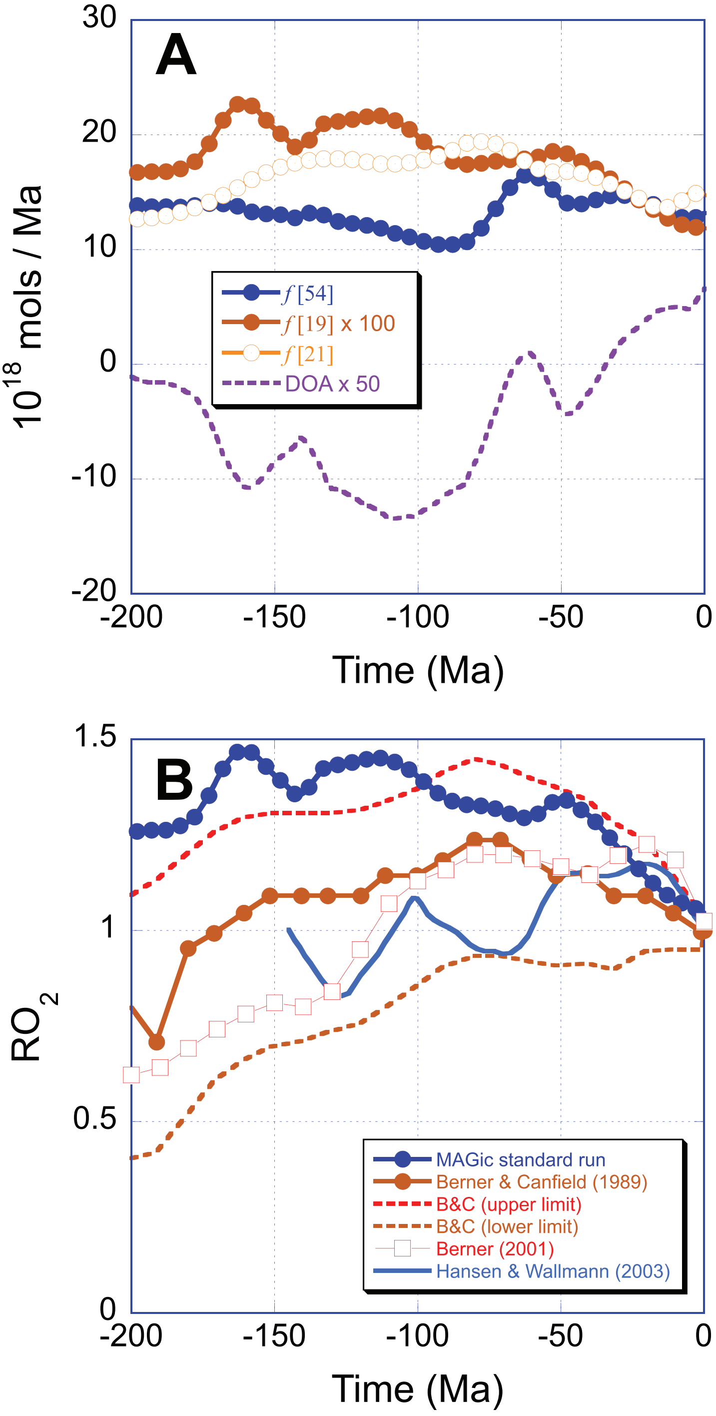

Fig. 14. Fluxes and mass-age relationships of organic matter and oxygen for $t > -200$ Ma. (A) Fluxes shown for marine organic matter burial (*f*[54], blue filled circles), total P weathering × 100 (*f*[19], brown filled circles), terrestrial organic carbon burial (*f*[21], open orange circles); DOA parameter (degree of anoxicity × 50, dashed magenta line) is also shown for comparison. (B) Mass of atmospheric oxygen relative to steady state value (RO$_2$, blue filled circles). Also shown for comparison are oxygen curves from Berner and Canfield (1989, filled brown circles, dashed lines indicate upper and lower limits), RROD ($J = 3$, $n = 1$) isotope model of Berner (2001, open squares), and Hansen and Wallmann (2003, solid blue line).

mass-age distribution and composition of clastic sediments were used to constrain fluxes, and negative feedbacks maintained through organization of material on the basis of reactivity ("rapid recycling"). This model showed a significant variation in atmospheric oxygen over the Phanerozoic, most distinctively as a large pulse over the Carboniferous associated with the enhanced production and burial of organic carbon as coal and associated disseminated organic matter during the rise of vascular land plants. For the time of the Mesozoic and later shown in figure 14, atmospheric oxygen reflects not only an increase in marine productivity, but also the burial of organic matter on land during the development of Cretaceous coals (*f* [21], fig. 14A). However, in the current state of the model development the description of organic weathering of organic matter on land produces only an exchange of $CO_2$ for $O_2$, and yields no flux of organic matter from land to ocean, nor (as mentioned earlier) is the sedimentation of organic matter tied in any quantitative way to clastic sedimentation rate. The strength of the land flux can be appreciated from values for the late pre-industrial land to sea river total organic carbon flux of approximately $30 \times 10^{12}$ mol C $y^{-1}$ and the burial rate of organic carbon on land on the order of $25 \times 10^{12}$ mol $y^{-1}$ as total organic carbon. Unfortunately, these simplifications also yielded model instabilities, discovered in sensitivity runs, that are particularly acute for the key period of large-scale expansion of vascular land plants during the late Paleozoic. MAGic derives a coal burial flux (*f* [21]) from the dataset of Budyko and others (1987). However, we found that use of this dataset as an *exact* constraint destabilized MAGic's carbonic acid system to the point that we could not compute a reasonable pH based on DIC and $PCO_2$ during the latter Permo-Carboniferous, a time of rapidly falling $PCO_2$ resulting from enhanced $CO_2$ uptake in weathering processes, soil formation, and fixation by land plants. To compute a solution, we were thus forced to dampen the terrestrial organic carbon burial flux to a small fraction of the value indicated by the data of Budyko and others (1987). These simplifications thus currently limit our ability to correctly model terrestrial processes independent of marine cycling, and moreover may create apparent feedbacks between land and open ocean processes that in fact do not exist. Because of difficulties in fully accounting for the large changes in terrestrial productivity over the earlier Paleozoic, we have thus chosen to restrict the time domain of the model results to $t > -200$ Ma (fig. 14), and defer complete presentation of this cycle until the next version of the model.

In our description of the subcycles of *Sodium-Potassium-Silicate-Carbonate-Chloride-$CO_2$* and *Sulfur,* we noted that free oxygen is returned to the atmosphere via the reduction of iron oxide (magnetite). This oxide formed originally as a product of an overall reaction involving ferrous silicate oxidation, sulfate reduction, and formation of basalt pyrite (eq 86 (table 3) without $CaCO_3$):

$$2SO_4^{2-} + 11Fe_2SiO_4 + 4H^+ = FeS_2 + 7Fe_3O_4 + 11SiO_2 + H_2O \qquad (86')$$

However, the input of sulfate to seawater is through pyrite weathering, and thus at least part of the sulfate-oxygen represents original atmospheric oxygen. Some of this sulfate is stored in marine sediments as pyrite (fig. 4) and represents oxygen accumulation in the atmosphere. During uplift this oxygen is removed by oxidation of the uplifted pyrite. In the reaction above, iron oxide, if subducted and sequestered in the mantle, represents oxygen that is not returned to the atmosphere. In the current model, this oxide is simply reduced to produce molecular oxygen. The details of how this reduction reaction occurs are, of course, problematic. The return flux (see fig. 15, *f* [119]) was introduced only to balance the oxygen cycle and allow us to examine the history of atmospheric oxygen without the complication of a mantle sink; in addition, the flux is also relatively small in comparison to the other oxygen fluxes. This issue has been discussed elsewhere in the literature, and subduction of ferric iron may indeed represent a long term oxygen sink

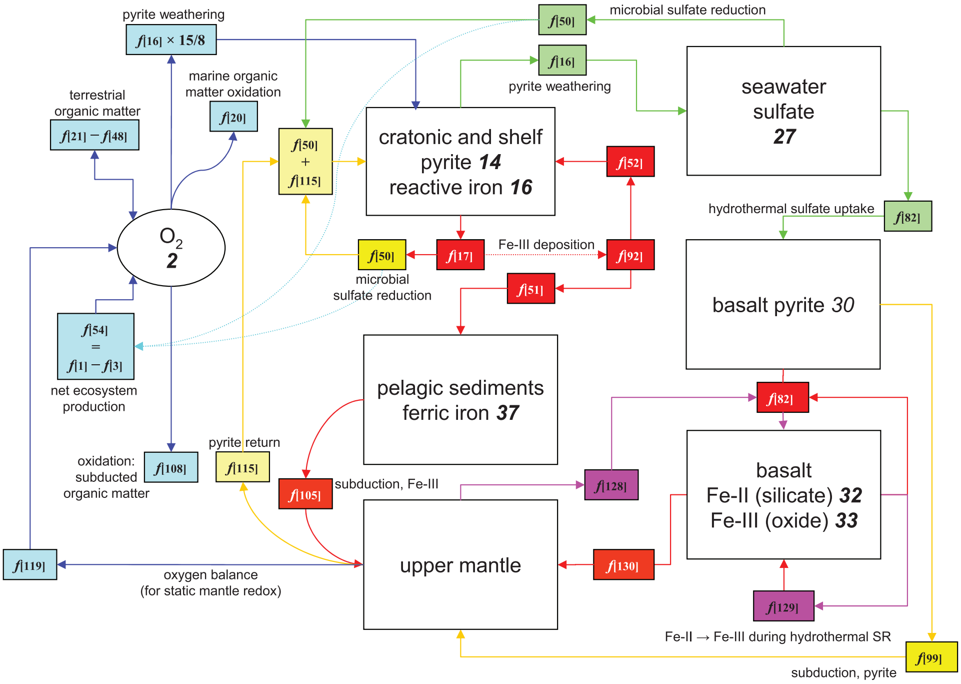

Fig. 15. Interaction of iron and atmospheric oxygen cycles. Flows of oxygen are shown in blue, sulfate in green, ferric iron in red, pyrite in gold, and reduced iron silicate as magenta. In addition to terrestrial organic matter cycling (burial – oxidation = *f* [21] – *f* [48]), oxidation of marine-derived organic matter on land (*f* [20]), and oxidation of pelagic organic matter, atmospheric oxygen is also controlled by the partitioning of iron between reduced and oxidized phases. Pyrite is produced both by microbial sulfate reduction (*f* [50]) and by hydrothermal sulfate reduction within seafloor basalt (*f* [82]). Pyrite oxidation (*f* [16]) consumes oxygen, and although part of this oxygen is balanced by primary production, hydrothermal pyrite formation involves production of ferric iron (*f* [129]). Although its flux is small, for purposes of steady state maintenance of $O_2$, the oxygen bound within this phase is ultimately returned to the atmosphere in the model (*f* [119]), although the precise mechanism for this return flux is problematic and not understood.

(Lécuyer and Ricard, 1999). In the MAGic model, return of molecular oxygen ultimately requires consumption of a reducing component. We speculate that the electrons required for the half-reaction (written for hematite reduction)

$$Fe_2O_3 + 2e- \; + SiO_2 + 2H^+ = Fe_2SiO_4 + H_2O \qquad (86'')$$

could be supplied by oxidation of hydrogen generated during serpentinization reactions, or alternatively, oxidation of organic matter, methane, or other hydrocarbons. Effectively, the model uses electrolysis of water to balance the overall reaction, supplying hydrogen to reduce ferric iron, and thus supplying molecular oxygen necessary to balance that consumed in pyrite weathering. Although this simplification may be of dubious validity, we feel its employment is warranted here, as we did not intend for output of the model in its current development to address the ongoing debate surrounding the evolution of mantle redox state.

## CONCLUSIONS

In a dynamical model describing the basic exchanges of the exogenic and shallow endogenic system, standard runs over the past 500 Ma generally show an increase in the mass of pelagic calcite. Transfers of magnesium between the carbonate and silicate reservoirs are mediated by variations in the rate of seafloor spreading, in which increases in dolomite mass are favored during periods of accelerating spreading that also yield increases in carbonate alkalinity. Model results indicate that reverse weathering is potentially a significant sink for magnesium and potassium, and together with basalt uptake is responsible for strong buffering of potassium over the Phanerozoic. Model results also include a general increase in atmospheric oxygen mediated largely by changes in the availability of phosphorous, that in turn may have arisen through progressive increase in the efficiency of continental apatite weathering.

Like the previous BLAG and GEOCARB models, MAGic is driven primarily by variations in (1) chemical weathering fluxes as mediated by time-dependent terms reflecting paleogeographic distributions, $CO_2$ feedback strength, lithology, land area, runoff, relief, and the agency of land plants, (2) formation of sedimentary carbonate minerals, (3) hydrothermal and magmatic fluxes related to basalt-seawater interaction, subduction, and metamorphism of sedimentary carbonate and aluminosilicates, and (4) production, sequestration, and oxidation of organic matter. MAGic also supplies additional detail in terms of major elemental fluxes involving sodium, potassium, calcium, magnesium, chloride, sulfur, phosphorous, iron, $CO_2$, and $O_2$, organized among the principal atmospheric, oceanic, and terrestrial reservoirs.

These results are constrained by the record of seawater $Mg^{2+}/Ca^{2+}$ as derived from fluid inclusion and evaporite distribution data, and show fair consistency with the limited proxy data available for paleo$CO_2$ and paleo-pH. The overall results for Phanerozoic $CO_2$ are also within the uncertainties of the current version of GEOCARB model. Like the initial versions of the BLAG and GEOCARB models, we regard this effort not as a definitive, static result but as a work in progress. Many simplifications were made in the interests of model stability, such as holding $V_{MIX}$ to a constant value despite our intuition that this term should probably vary in response to the vigor of thermohaline circulation and ocean ventilation. Future improvements will include the addition of isotopic constraints ($\delta^{34}S$, $\delta^{13}C$, and $^{87}Sr/^{86}Sr$), a more robust numerical solver routine, as well as more extensive treatment of the relationships between the paleogeographic distribution of carbonate platforms and pelagic sediments, seafloor spreading rates, volcanism, and carbon cycling. In addition, we point out that the variations in ocean-atmosphere composition during the Phanerozoic exert a strong control on the mass-age distribution of both inorganic and biogenic carbonate mineralogy and chemistry (Mackenzie and Pigott, 1981; Stanley and Hardie, 1998, 1999; Veizer and Mackenzie, 2004; Guidry and others, 2006). Models such as MAGic allow an integrated description of coupled system behavior, thus helping to constrain the important variables governing the sedimentation and accumulation of carbonates through time.

## ACKNOWLEDGMENTS

The authors wish to acknowledge the effort of those who took the time to read and comment on a lengthy and complex manuscript. We owe a considerable debt to Bob Berner for his careful review of the paper, substantially improving its clarity and precision, as well as for numerous discussions concerning the MAGic model itself. The authors express their sincere thanks to Klaus Wallmann, Lee Kump, and an anonymous reviewer, who formally reviewed and improved earlier versions of this work. RSA wishes to extend personal thanks to Professor John W. Morse at Texas A&M University for his comments on an earlier version of this paper, and to Professor Andreas Luttge of Rice University for his support of the work. RSA also thanks several students at Rice University, including Kevin J. Davis and Carter A. Sturm, who participated in thoughtful discussions involving MAGic results. FTM would like to recognize his colleagues, Robert M. Garrels and Roland Wollast, now both deceased, and Abraham Lerman of Northwestern University for their many years of exciting discussion involving the geochemical cycles that has led to a number of the ideas expressed in this paper and laid the foundation for much future work in geochemical cycling. FTM gratefully acknowledges the National Science Foundation (Grants No. ATM04-39051 and EAR02-23509) for support of this work.

### Appendix A

Table A1

*Principal Fluxes*

| Component | Symbol | $10^{18}$ mol / Ma | Description of Flux and Supporting Equations |
|---|---|---|---|
| $C_{org}$,$CO_2$, $O_2$ | $f[1]$ | 2500 | Primary Production (per mol C) |
| | | | $f[1] = \gamma_{RR} \times f[55]$ |
| | | | $\gamma_{RR} = 106$ = Redfield C:P ratio |
| | $f[2]_{Ca\text{-}Mg}$ | 19.154 | Ca-Mg silicates |
| | $f[2]_{Na\text{-}K}$ | 3.327 | Na-K silicates |
| $CO_2$ | $f[2]_{Total}$ | 22.481 | Total weathering uptake, all silicates |
| | | | $f[2] = 2 \times (f[6] + f[7]) + f[12] + 2 \times f[13] + f[4] + f[5]$ |
| $C_{org}$,$CO_2$, $O_2$ | $f[3]$ | 2485 | Respiration (per mol C) |
| | | | $f[3] = f[1] - f[54]$ |
| $NaAlSi_3O_8$ | $f[4]$ | 2.261 | Na-silicate (normative albite) $H_2CO_3$ weathering, per mol of $Na^+$ produced |
| | | | $f[4] = k\,[4] \times y\,[4]$ |
| | | | $k\,[4] \sim 3.8 \times 10^{-4}$ |
| $KAlSi_3O_8$ | $f[5]$ | 1.065 | K-silicate (normative anorthite) $H_2CO_3$ weathering, per mol of $K^+$ produced |
| | | | $f[5] = k\,[5] \times y\,[5]$ |
| | | | $k\,[5] \sim 2.6 \times 10^{-4}$ |
| $CaAl_2Si_2O_8$ | $f[6]$ | 2.781 | Ca-silicate (normative anorthite) $H_2CO_3$ weathering |
| | | | $f[6] = k\,[6] \times y\,[6]$ |
| | | | $k\,[6] \sim 6.0 \times 10^{-4}$ |
| $MgSiO_3$ | $f[7]$ | 2.236 | Mg-silicate (normative pyroxene) $H_2CO_3$ weathering |
| | | | $f[7] = k\,[7] \times y\,[7]$ |
| | | | $k\,[7] \sim 4.5 \times 10^{-4}$ |
| $NaAlSi_3O_8$ | $f[8]$ | 0.361 (0.180) | Na-silicate (normative albite) $H_2SO_4$ weathering, per mol of $Na^+$ ($H_2SO_4$) produced |
| | | | $f[8] = \gamma\,[23] \times f[16] \times 2$ |
| | | | $\gamma\,[23] \sim 0.1$ |

TABLE A1

*(continued)*

| Component | Symbol | $10^{18}$ mol / Ma | Description of Flux and Supporting Equations |
|---|---|---|---|
| $KAlSi_3O_8$ | $f[9]$ | 0.170 (0.085) | K-silicate (normative orthoclase) $H_2SO_4$ weathering, per mol of $K^+$ ($H_2SO_4$) produced<br>$f[9] = \gamma\,[24] \times f[16] \times 2$<br>$\gamma\,[24] \sim 4.7 \times 10^{-2}$ |
| $CaAl_2Si_2O_8$ | $f[10]$ | 0.442 | Ca-silicate (normative anorthite) $H_2SO_4$ weathering<br>$f[10] = \gamma\,[21] \times f[16]$<br>$\gamma\,[21] \sim 0.25$ |
| $MgSiO_3$ | $f[11]$ | 0.356 | Mg-silicate (normative pyroxene) $H_2SO_4$ weathering<br>$f[11] = \gamma\,[22] \times f[16]$<br>$\gamma\,[22] \sim 0.20$ |
| $CaCO_3$ | $f[12]$ | 5.209 | Calcite $H_2CO_3$ weathering<br>$f[12] = k\,[8] \times y\,[8]$<br>$k\,[8] \sim 3.8 \times 10^{-3}$ |
| $CaMg(CO_3)_2$ | $f[13]$ | 1.956 | Dolomite $H_2CO_3$ weathering<br>$f[13] = k\,[9] \times y\,[9]$<br>$k\,[9] \sim 4.5 \times 10^{-3}$ |
| $CaCO_3$ | $f[14]$ | 0.831 (0.415) | Calcite $H_2SO_4$ weathering, per mol $Ca^{2+}$ ($H_2SO_4$) produced<br>$f[14] = \gamma\,[19] \times f[16] \times 2$<br>$\gamma\,[19] \sim 0.23$ |
| $CaMg(CO_3)_2$ | $f[15]$ | 0.312 | Dolomite $H_2SO_4$ weathering<br>$f[15] = \gamma\,[20] \times f[16]$<br>$\gamma\,[20] \sim 0.17$ |
| $FeS_2$ | $f[16]$ | 1.792 | Pyrite weathering, per mol S<br>$f[16] = k\,[14] \times y\,[14]$<br>$k\,[14] \sim 1.9 \times 10^{-2}$ |
| Fe-III | $f[17]$ | 1.388 | Total reactive Fe flux<br>$f[17] = k\,[3] \times y\,[16]$<br>$k\,[3] \sim 4.2 \times 10^{-3}$ |
| Apatite | $f[19]$ | 0.123 | Total weathering, per mol P<br>$f[19] = k\,[2] \times y\,[15]$<br>$k\,[2] \sim 7.7 \times 10^{-3}$ |

TABLE A1

*(continued)*

| Component | Symbol | $10^{18}$ mol / Ma | Description of Flux and Supporting Equations |
|---|---|---|---|
| Corg | $f[20]$ | 11.384 | Organic matter oxidation<br>$f[20] = k\,[15] \times y\,[3]$<br>$k\,[15] \sim 2.3 \times 10^{-2}$ |
| $C_{org}$ | $f[21]$ | 0.16 | Terrestrial organic carbon burial<br>$f[21] = c_{BU} + f[48]$<br>$c_{BU} = y'\,[17] = 0$ at steady state |
| $C_{org}$ | $f[22]$ | — | Methane hydrate |
| $CaMg(CO_3)_2$ | $f[23]$ | 0.5 | Burial of shelf dolomite<br>$f[23] = k\,[64] \times y\,[9]$<br>$k\,[64] \sim 1.1 \times 10^{-3}$ |
| $CaSO_4$ | $f[24]$ | 0.868 | Evaporite weathering<br>$f[24] = k\,[10] \times y\,[12]$<br>$k\,[10] \sim 1.0 \times 10^{-2}$ |
| $MgSO_4$ | $f[25]$ | 0.54 | Evaporite weathering<br>$f[25] = k\,[11] \times y\,[13]$<br>$k\,[11] \sim 0.12$ |
| NaCl | $f[26]$ | 3.078 | Evaporite weathering<br>$f[26] = k\,[12] \times y\,[10]$<br>$k\,[12] \sim 1.7 \times 10^{-2}$ |
| KCl | $f[27]$ | 0.065 | Evaporite weathering<br>$f[27] = k\,[13] \times y\,[11]$<br>$k\,[13] \sim 3.3 \times 10^{-2}$ |
| $HCO_3^-$ | $f[28]$ | 31.603 | Bicarbonate flux from rock weathering by carbonic acid<br>$f[28] = 2 \times (f[6] + f[7]) + 2 \times f[12] + 4 \times f[13] + f[4] + f[5]$ |
| $HCO_3^-$ | $f[29]$ | 1.454 | Bicarbonate flux from rock weathering by sulfuric acid<br>$f[29] = f[14] + f[15] \times 2$ |
| $HCO_3^-$ | $f[30]$ | 33.057 | Total bicarbonate flux, weathering<br>$f[30] = f[28] + f[29]$ |
| $SO_4^{2-}$ | $f[31]$ | 3.200 | Sulfate flux, pyrite + evaporite weathering<br>$f[31] = f[16] + f[24] + f[25]$ |

TABLE A1

*(continued)*

| Component | Symbol | $10^{18}$ mol / Ma | Description of Flux and Supporting Equations |
|---|---|---|---|
| $Cl^-$ | $f[32]$ | 3.143 | Chloride flux, evaporite weathering<br>$f[32] = f[26] + f[27]$ |
| Ca2+ | $f[33]$ | 12.4 | Calcium flux, silicate, carbonate, and evaporite weathering<br>$f[33] = f[12] + f[14] + f[13] + f[15] + f[6] + f[10] + f[24]$ |
| $Mg^{2+}$ | $f[34]$ | 5.4 | Magnesium flux, silicate, carbonate, and evaporite weathering<br>$f[34] = f[13] + f[15] + f[7] + f[11] + f[25]$ |
| $Na^+$ | $f[35]$ | 5.7 | Sodium flux, silicate + evaporite weathering<br>$f[35] = f[4] + f[8] + f[26]$ |
| $K^+$ | $f[36]$ | 1.3 | Potassium flux, silicate + evaporite weathering<br>$f[36] = f[5] + f[9] + f[27]$ |
| $CaCO_3$ | $f[37]$ | 15.926 | Normative $CaCO_3$ shelf flux, steady state (constant parameter) |
| $MgCO_3$ | $f[38]$ | 0.1 | Normative $MgCO_3$ shelf flux, steady state (constant parameter) |
| $CaCO_3$ | $f[39]$ | 7.336 | Calcite shelf burial flux<br>$f[39] = k[19] \times y[8]$<br>$k[19] \sim 5.3 \times 10^{-3}$ |
| albite | $f[40]$ | 0.655 | Montmorillonite production from Na-silicate weathering<br>$f[40] = 0.25 \times (f[4] + f[8])$ |
| anorthite | $f[41]$ | 2.592 | Mantle flux, Ca<br>$f[41] = f[96]$ |
| $CaCO_3$ | $f[42]$ | 3.450 | Diagenetic dissolution of shelf $CaCO_3$<br>$f[42] = k[18] \times y[8]$<br>$k[18] \sim 2.5 \times 10^{-3}$ |
| $CaMg(CO_3)_2$ | $f[44]$ | 2.668 | Uplift of burial dolomite<br>$f[44] = k[20] \times y[19]$<br>$k[20] \sim 1.0 \times 10^{-2}$ |
| $CaMg(CO_3)_2$ | $f[45]$ | 2.168 | Calcite dolomitization by Mg-chlorite<br>$f[45] = k[60] \times y[40]$<br>$k[60] \sim 6.0 \times 10^{-3}$ |
| $CaCO_3$ | $f[46]$ | 2.000 | Metamorphism of burial calcite<br>$f[46] = k[21] \times y[18]$<br>$k[21] \sim 1.2 \times 10^{-3}$ |

TABLE A1

*(continued)*

| Component | Symbol | $10^{18}$ mol / Ma | Description of Flux and Supporting Equations |
|---|---|---|---|
| CaCO3 | $f[47]$ | 1.000 | Uplift of burial calcite<br>$f[47] = k\,[22] \times y\,[18]$<br>$k\,[22] \sim 5.8 \times 10{-}4$ |
| Corg | $f[48]$ | 0.16 | Terrestrial organic carbon uplift and oxidative weathering<br>$f[48] = k\,[23] \times y\,[17]$<br>$k\,[23] \sim 2.8 \times 10{-}1$ |
| $CH_4$ | $f[49]$ | — | Hydrate decomposition/oxidation |
| $SO_4^{2-}$ ($C_{org}$) | $f[50]$ | 1.527 (2.863) | $FeS_2$ formation by shelf $C_{org}$ oxidation, per mol S (per mol C)<br>$f[50] = (a + b \times \mathrm{DOA}) \times f[17] \times 2$<br>$a = 0.43$<br>$b = 0.57$<br>$\mathrm{DOA(t)} = 1 - k\,[1] \times V_{MIX} \times y\,[2] \,/\, f[1]$<br>$\mathrm{DOA(0)} \sim 0.21$<br>$k\,[1] \sim 17.3$<br>$V_{MIX} = 3$ |
| Fe-III | $f[51]$ | 0.133 | Pelagic deposition<br>$f[51] = f[92] \times 0.21$ |
| Fe-III | $f[52]$ | 0.492 | Shelf deposition<br>$f[52] = f[92] \times 0.79$ |
| $PO_4^{3-}$ | $f[53]$ | 0.007 | Basalt uptake<br>$f[53] = k\,[30] \times y\,[27]$<br>$k\,[30] \sim 2.3$ |
| $C_{org}$ | $f[54]$ | 15 | Net production<br>$f[54] = k\,[25] \times f[1]^{2.5}$ |
| $PO_4^{3-}$ | $f[55]$ | 23.585 | Primary Production<br>$f[55] = k\,[24] \times V_{MIX} \times y\,[27]$<br>$V_{MIX} = 3$<br>$k\,[24] \sim 2620.5$ |
| $C_{org}$ | $f[56]$ | 14.263 | Shelf deposition/burial<br>$f[56] = 0.951 \times f[54]$ |

TABLE A1

*(continued)*

| Component | Symbol | $10^{18}$ mol / Ma | Description of Flux and Supporting Equations |
|---|---|---|---|
| Corg | $f[57]$ | 0.737 | Pelagic deposition/burial<br>$f[57] = 0.049 \times f[54]$ |
| Porg | $f[58]$ | 0.057 | P of shelf organic matter burial<br>$f[58] = f[56] / 250$ |
| Porg | $f[59]$ | 0.003 | P of pelagic organic matter burial<br>$f[59] = f[57] / 250$ |
| Porg | $f[60]$ | 0.06 | P burial<br>$f[60] = f[58] + f[59]$ |
| $PO_4^{3-}$ | $f[61]$ | 23.525 | Remineralization<br>$f[61] = f[55] + f[54] / 250$ |
| P | $f[62]$ | 0.045 | Shelf Fe-oxyhydroxide-bound P deposition<br>$f[62] = k[26] \times f[52]$<br>$k[26] \sim 9.1 \times 10^{-2}$ |
| P | $f[63]$ | 0.005 | Pelagic Fe-oxyhydroxide-bound P deposition<br>$f[63] = k[27] \times f[51]$<br>$k[27] \sim 4.1 \times 10^{-2}$ |
| Apatite | $f[64]$ | 0.005 | Apatite shelf deposition, per mol P<br>$f[64] = k[28] \times f[61]^{2.5}$<br>$k[28] \sim 1.9 \times 10^{-6}$ |
| Apatite | $f[65]$ | 0.0006 | Apatite pelagic deposition, per mol P<br>$f[65] = k[29] \times f[61]^{2.5}$<br>$k[29] \sim 2.2 \times 10^{-7}$ |
| NaCl | $f[66]$ | 3.078 | Evaporite deposition<br>$f[66] = k[31] \times y[20] \times y[25]$<br>$k[31] \sim 6.0 \times 10^{-6}$ |
| KCl | $f[67]$ | 0.065 | Evaporite deposition<br>$f[67] = k[32] \times y[22] \times y[25]$<br>$k[32] \sim 5.9 \times 10^{-6}$ |

Table A1

*(continued)*

| Component | Symbol | $10^{18}$ mol / Ma | Description of Flux and Supporting Equations |
|---|---|---|---|
| $CaSO_4$ | $f[68]$ | 0.868 | Evaporite formation<br>Computed from ion concentration product:<br>$f[68] = k\,[33] \times y\,[23] \times y\,[26]$<br>$k\,[33] \sim 1.5 \times 10^{-3}$<br><br>Alternatively, computed using concentration ratio constraint:<br>$f[68] = (f[31] - f[50] - f[69] - f[82])$<br>$- y[23] \times \boldsymbol{Q}'(t) + (y\,[26] / y\,[24]) \times \boldsymbol{R}'(t)$<br>$- (f[34] - f[81] - f[75] - f[71] - f[69] - f[79])$ |
| $MgSO_4$ | $f[69]$ | 0.540 | Evaporite formation<br>$f[69] = k\,[34] \times y\,[24] \times y\,[26]$<br>$k\,[34] \sim 1.8 \times 10^{-4}$ |
| $CO_2$ | $f[70]$ | 1.336 | $CO_2$ associated with microbial sulfate reduction<br>$f[70] = f[50] \times 0.875$ |
| $CaMg(CO_3)_2$ | $f[71]$ | 0.010 | Dolomite formation associated with microbial sulfate reduction<br>$f[71] = f[50] \times 6.2\ 4\times 10^{-3}$ |
| $CaCO_3$ | $f[72]$ | 1.508 | Calcite formation associated with microbial sulfate reduction<br>$f[72] = f[50] \times 0.9875$ |
| $C_{org}$ | $f[73]$ | 2.863 | Organic matter consumed during microbial sulfate reduction<br>$f[73] = f[50] \times 0.875$ |
| $CaCO_3$ | $f[74]$ | 14.318 | Shelf precipitation (non-SR)<br>$f[74] = f[93] - f[76]$ |
| $CaMg(CO_3)_2$ | $f[75]$ | 0.090 | Shelf precipitation (non-SR)<br>$f[75] = c'_{\mathrm{Ap}}(t) \times k_{\mathrm{T}} \times (1 - \Omega_{\mathrm{dol}})^{n}$ |
| $CaCO_3$ | $f[76]$ | 5.632 | Pelagic precipitation (non-SR)<br>$f[76] = \beta(t) \times f[93] / c_{\mathrm{Ap}}(t)$ |
| $Na^+,K^+$ | $f[77]$ | 0.061 | Cation exchange, RW K-illite formation<br>$f[77] = k\,[42] \times y\,[22]$<br>$k\,[42] \sim 4.2 \times 10^{-3}$ |
| $HCO_3^-,CO_2$ | $f[78]$ | 0.030 | $HCO_3 \rightarrow CO_2$ transfer tied to $f[77]$<br>$f[78] = f[77] \times 0.5$ |

Table A1

(*continued*)

| Component | Symbol | $10^{18}$ mol / Ma | Description of Flux and Supporting Equations |
|---|---|---|---|
| $Mg^{2+}$ | $f[79]$ | 2.168 | RW Mg-chlorite, per mol Mg<br>$f[79] = k[43] \times y[24]$<br>$k[43] \sim 2.9 \times 10^{-2}$ |
| $HCO_3^-$,$CO_2$ | $f[80]$ | 4.336 | $HCO_3 \rightarrow CO_2$ transfer tied to $f[79]$<br>$f[80] = f[79] \times 2$ |
| $Mg^{2+}$ | $f[81]$ | 2.592 | Basalt uptake<br>$f[81] = k[44] \times y[24]$<br>$k[44] \sim 3.5 \times 10^{-2}$ |
| $SO_4^{2-}$ | $f[82]$ | 0.265 | SR (hydrothermal SR, per mol S)<br>$f[82] = k[45] \times y[26]$<br>$k[44] \sim 6.7 \times 10^{-3}$ |
| $Na^+$ | $f[83]$ | 2.652 | Basalt uptake<br>$f[83] = k[46] \times y[20]$<br>$k[46] \sim 4.0 \times 10^{-3}$ |
| $K^+$ | $f[84]$ | 1.174 | Basalt uptake<br>$f[84] = k[47] \times y[22]$<br>$k[47] \sim 8.2 \times 10^{-2}$ |
| $CO_2/HCO_3^-$ | $f[85]$ | 3.296 | Exchange from basalt calcite formation<br>$f[85] = f[94] \times 2$ |
| $CO_2$ | $f[89]$ | 20.131 | $CO_2$ evasion upon calcite + dolomite precipitation<br>$f[89] = f[75] \times 2 + f[74] + f[76]$ |
| Fe-III | $f[92]$ | 0.6246 | Fe-III available for shelf + pelagic deposition after SR<br>$f[92] = f[17] - f[50] / 2$ |
| $CaCO_3$ | $f[93]$ | 19.950 | Total $CaCO_3$ precipitation (non-SR, shelf + pelagic)<br>$f[93] = y[23] / y[24] \times (y[23] \times \boldsymbol{R}'(t) - (f[34] - f[69] - f[79]$<br>$- f[75] - f[71])) + f[33] - f[75] - f[71] - f[72] - f[68]$<br>$+ f[42] + f[111] + f[96]$ |
| $CaCO_3$ | $f[94]$ | 1.648 | Basalt $CaCO_3$<br>$f[94] = k[48]$<br>$k[48] \sim 1.65$ |

TABLE A1
*(continued)*

| Component | Symbol | $10^{18}$ mol / Ma | Description of Flux and Supporting Equations |
|---|---|---|---|
| $Ca^{2+}$ | $f[96]$ | 2.592 | Basalt release to seawater<br>$f[96] = f[81] + 0.5 \times (f[83] + f[84]) - f[94] - f[82]$ |
| Apatite | $f[97]$ | 0.007 | Basalt → Mantle<br>$f[97] = k\,[50] \times y\,[31]$<br>$k\,[50] \sim 4.2 \times 10^{-5}$ |
| $CaCO_3$ | $f[98]$ | 1.648 | Basalt $CaCO_3 \rightarrow$ Mantle<br>$f[98] = k\,[49] \times y\,[29]$<br>$k\,[49] \sim 5.1 \times 10^{-3}$ |
| $FeS_2$ | $f[99]$ | 0.265 | Basalt pyrite → Mantle, per mol S<br>$f[99] = k\,[51] \times y\,[30]$<br>$k\,[49] \sim 1.3 \times 10^{-3}$ |
| $Mg^{2+}$ | $f[100]$ | 2.592 | Basalt → Mantle<br>$f[100] = f[81]$ |
| $Na^{+}$ | $f[101]$ | 2.652 | Basalt → Mantle<br>$f[101] = f[83]$ |
| $K^{+}$ | $f[102]$ | 1.174 | Basalt → Mantle<br>$f[102] = f[84]$ |
| $CaCO_3$ | $f[103]$ | 0.648 | Transfer to mantle, pelagic calcite<br>$f[103] = \sigma(t) \times f[112]$ |
| Fe-III | $f[105]$ | 0.1326 | Mantle uptake from subducted pelagic Fe-III<br>$f[105] = k\,[57] \times y\,[37]$<br>$k\,[57] \sim 6.6 \times 10^{-3}$ |
| Apatite | $f[107]$ | 0.009 | Transfer to mantle from subducted pelagic P<br>$f[107] = k\,[52] \times y\,[36]$<br>$k\,[52] \sim 2.2 \times 10^{-3}$ |
| $C_{org}$ | $f[108]$ | 0.737 | Subduction and oxidation of pelagic organic matter<br>$f[108] = k\,[54] \times y\,[34]$<br>$k\,[54] \sim 4.3 \times 10^{-3}$ |
| $CaCO_3$ | $f[110]$ | 1.000 | Metamorphism, pelagic calcite<br>$f[110] = (1 - \sigma(t)) \times f[112]$ |

TABLE A1

*(continued)*

| Component | Symbol | $10^{18}$ mol / Ma | Description of Flux and Supporting Equations |
|---|---|---|---|
| $CaCO_3$ | $f[111]$ | 3.984 | Diagenetic dissolution, pelagic calcite<br>$f[111] = k\ [58] \times y\ [35]$<br>$k\ [58] \sim 7.4 \times 10^{-3}$ |
| $CaCO_3$ | $f[112]$ | 1.648 | Pelagic calcite for $f[103] + f[110]$<br>$f[112] = k\ [53] \times y\ [35]$<br>$k\ [53] \sim 3.0 \times 10^{-3}$ |
| Apatite | $f[113]$ | 0.016 | Cratonic return<br>$f[113] = f[97] + f[107]$ |
| $CO_2$ | $f[114]$ | 3.033 | Volcanism (continental and submarine)<br>$f[114] = f[98] + f[103] + f[108]$ |
| $FeS_2$ | $f[115]$ | 0.265 | Return to craton<br>$f[115] = f[99]$ |
| Mg | $f[116]$ | 2.592 | Return to craton<br>$f[116] = f[100]$ |
| Na | $f[117]$ | 2.652 | Return to craton<br>$f[117] = f[101]$ |
| K | $f[118]$ | 1.174 | Return to craton<br>$f[118] = f[102]$ |
| Fe-III | $f[119]$ | 1.989 | Reduced to Fe-II<br>$f[119] = f[130] + f[105]$ |
| Na-mont<br>K-illite | $f[121]$ | 0.030 | Na-mont/K-illite exchange during reverse weathering (RW), $Na^+$ flux to seawater<br>$f[121] = f[77] / 2$ |
| Kaolinite | $f[122]$ | 0.015 | "Kaolinite" → illite (magmatic)<br>$f[122] = f[77] / 4$ |
| Montmorillonite | $f[123]$ | 0.030 | "Montmorillonite" → "illite" (magmatic)<br>$f[123] = f[77] / 2$ |
| K-illite | $f[124]$ | 0.060 | "K-illite" → "orthoclase" (magmatic)<br>$f[124] = k\ [62] \times y\ [39]$<br>$k\ [53] \sim 1.7 \times 10^{-4}$ |
| Kaolinite | $f[125]$ | 0.4336 | "Kaolinite" → "chlorite" (magmatic)<br>$f[125] = f[79] / 5$ |

Table A1

*(continued)*

| Component | Symbol | $10^{18}$ mol / Ma | Description of Flux and Supporting Equations |
|---|---|---|---|
| Chlorite | $f[126]$ | 0 | "Chlorite" → "pyroxene" (magmatic)<br>$f[126] = f[79] - f[45]$ |
| Montmorillonite | $f[127]$ | 0.625 | "Montmorillonite" → "albite" (magmatic)<br>$f[127] = f[40] - f[123]$ |
| Fe-II | $f[128]$ | 1.988 | Net Fe-II from hydrothermal SR → Mantle<br>$f[128] = f[130] + f[105] + (f[99] - f[115])/2$ |
| Fe-II, Fe-III | $f[129]$ | 1.856 | Fe-II → Fe-III during hydrothermal SR<br>$f[129] = f[82] \times 7$ |
| Fe-III | $f[130]$ | 1.856 | Fe-III mantle uptake<br>$f[130] = k[63] \times y[33]$<br>$k[63] \sim 2.2 \times 10^{-4}$ |
| Anorthite | $f[131]$ | 4.240 | Basaltic anorthite decomposition<br>$f[131] = f[81] + (f[83] + f[84])/2 - f[82]$ |
| Fe-II | $f[132]$ | 1.988 | Fe-II return to basalt silicate<br>$f[132] = f[128]$ |

Fluxes are tabulated to a precision far exceeding their absolute certainty in order to minimize rounding errors in the presentation and permit simple mass balance checks. Flux coefficients ($k_{[i]}$) have units of $Ma^{-1}$. Stoichiometric coefficients (γ) are dimensionless. Unless otherwise indicated, fluxes are given on a per mol basis of component consumed or produced, and all values represent steady-state (Quaternary, pre-anthropogenic) estimates. SR = sulfate reduction, RW = reverse weathering. Not all fluxes are shown (gaps in index sequence), as some variables are used simply for intermediate storage.

TABLE A2

*Net Atmospheric Fluxes*

| Component | $10^{18}$ mol / Ma | Description |
|---|---|---|
| $CO_2$ (net) | | |
| $-f[12] - (f[13]+f[6]+f[7]) \times 2$ | $-19.154$ | Ca-Mg carbonate weathering |
| $-f[4] - f[5]$ | $-3.327$ | K-Na silicates weathering |
| $+f[20]$ | $+11.400$ | Organic carbon oxidation on land |
| $+f[3]$ | $+2485$ | Net respiration |
| $-f[1]$ | $-2500$ | Net fixation |
| $+f[70]$ | $+1.336$ | Sulfate reduction |
| $+f[108]$ | $+0.737$ | Subduction-oxidation of pelagic organic matter |
| $+f[103]$ | $+0.648$ | Decarbonation from pelagic $CaCO_3$ subduction |
| $+f[110]$ | $+1.000$ | Decarbonation from pelagic $CaCO_3$ metamorphism |
| $+f[46]$ | $+2.000$ | Decarbonation from burial metamorphism of shelf $CaCO_3$ |
| $+f[94]$ | $+1.648$ | Release during basalt-calcite formation |
| $+f[98]$ | $+1.648$ | Decarbonation from basalt-calcite subduction |
| $+f[89]$ | $+20.131$ | $CaCO_3 - MgCO_3$ precipitation |
| $+f[80]$ | $+4.336$ | RW Mg-chlorite |
| $+f[78]$ | $+0.030$ | RW K-illite/Na-montmorillonite |
| $-f[111]$ | $-3.984$ | $CaCO_3$ diagenetic dissolution, pelagic |
| $-f[42]$ | $-3.450$ | $CaCO_3$ diagenetic dissolution, shelf |
| $-f[48]$ | $-0.16$ | Terrestrial organic matter oxidation |
| $+f[21]$ | $+0.16$ | Terrestrial organic matter, net fixation |
| $O_2$ (net) | | |
| $-f[16] \times 1.875 + f[119] \times 0.25$ | $-2.863$ | Pyrite oxidation/weathering |
| $-f[20]$ | $-11.400$ | Shelf/marine organic matter oxidation (by oxygen) |
| $-f[108]$ | $-0.737$ | Pelagic organic matter oxidation (post subduction) |
| $-f[3]$ | $-2485$ | Marine organic matter, net respiration |
| $+f[1]$ | $+2500$ | Marine organic matter, net fixation |
| $+f[21]$ | $+0.16$ | Terrestrial organic matter, net fixation |
| $-f[48]$ | $-0.16$ | Terrestrial organic matter oxidation |

SR = sulfate reduction. RW = reverse weathering

TABLE A3

*Model Differential Equations and Steady State Values*

| $y'[i]$ | Reservoir component | $y[i]\|_{t\to\infty}$ | Balance of fluxes ($y'[i] \sim 0\|_{t\to\infty}$) | |
|---|---|---|---|---|
| *Atmosphere —* | | | | |
| $y'[1]$ | $CO_2$ | 0.055 | $-f[1]-f[2]-f[42]-f[111]+f[20]+f[46]+f[70]+f[89]+f[48]+f[78]+f[80]+f[3]+f[110]+f[114]+f[94]-f[21]$ | (A1) |
| $y'[2]$ | $O_2$ | 38.0 | $+f[1]-f[3]-f[20]-f[48]-f[108]+{}^{15}/_{8}\times(-f[16])+(f[119])/4+f[21]$ | (A2) |
| *Marine organic matter (excluding pelagic) —* | | | | |
| $y'[3]$ | "$CH_2O$" | 503 | $-f[20]-f[73]+f[56]$ | (A3) |
| *Crystalline continental rocks —* | | | | |
| $y'[4]$ | Na-silicate ("$NaAlSi_3O_8$") | 5950 | $-{}^{5}/_{4}\times(f[4]+f[8])+f[117]+f[127]$ | (A4) |
| $y'[5]$ | K-silicate ("$KAlSi_3O_8$") | 4175 | $-f[5]-f[9]+f[118]+f[124]$ | (A5) |
| $y'[6]$ | Ca-silicate ("$CaAl_2Si_2O_8$") | 4598 | $-f[6]-f[41]-f[10]+f[45]+f[46]+f[103]+f[110]$ | (A6) |
| $y'[7]$ | Mg-silicate ("$MgSiO_3$") | 4997 | $-f[7]-f[11]+f[116]+f[126]$ | (A7) |
| *Shelf and shallow continental sediments and sedimentary rocks —* | | | | |
| $y'[8]$ | Calcite | 1371 | $-f[12]-f[14]-f[39]+f[74]+f[72]-f[42]+f[47]$ | (A8) |
| $y'[9]$ | Dolomite | 437 | $-f[23]-f[15]-f[13]+f[44]+f[75]+f[71]$ | (A9) |
| $y'[10]$ | NaCl | 183 | $-f[26]+f[66]$ | (A10) |
| $y'[11]$ | KCl | 2.0 | $-f[27]+f[67]$ | (A11) |
| $y'[12]$ | $CaSO_4$ | 85 | $-f[24]+f[68]$ | (A12) |
| $y'[13]$ | $MgSO_4$ | 4.6 | $-f[25]+f[69]$ | (A13) |
| $y'[14]$ | Pyrite-S | 96 | $-f[16]+2\times f[71]+f[72]+f[115]$ | (A14) |

Table A3

*(continued)*

| $y'[i]$ | Reservoir component | $y[i]\|_{t\rightarrow\infty}$ | Balance of fluxes ($y'[i] \sim 0\|_{t\rightarrow\infty}$) | |
|---|---|---|---|---|
| $y'[15]$ | Apatite | 16 | $-f[19]+f[113]+f[64]+f[62]+f[58]$ | (A15) |
| $y'[16]$ | $Fe_2O_3$ | 328 | $-f[17]+{}^1/_2\times f[16]+f[52]$ | (A16) |
| *Deep cratonic burial sediments and sedimentary rocks —* | | | | |
| $y'[17]$ | Organic carbon | 0.57 | $-f[48]+f[21]$ | (A17) |
| $y'[18]$ | Calcite | 1720 | $-2\times f[45]-f[46]-f[47]+f[39]$ | (A18) |
| $y'[19]$ | Dolomite | 260 | $-f[44]+f[45]+f[23]$ | (A19) |
| *Seawater components —* | | | | |
| $y'[20]$ | $Na^+$ | 658 | $-f[66]-f[83]+f[35]+f[121]$ | (A20) |
| $y'[21]$ | $HCO_3^-$ (total DIC) | 2.85 | $-4\times f[75]-2\times f[74]-2\times f[76]-f[78]-f[80]-f[85]+f[30]+2\times(f[111]+f[42])$ | (A21) |
| $y'[22]$ | $K^+$ | 14.3 | $-f[67]-f[84]-f[77]+f[36]$ | (A22) |
| $y'[23]$ | $Ca^{2+}$ | 14.4 | $-f[68]-f[71]-f[72]-f[74]-f[75]-f[76]+f[33]+f[42]+f[111]+f[96]$ | (A23) |
| $y'[24]$ | $Mg^{2+}$ | 74.1 | $-f[81]-f[75]-f[71]-f[69]-f[79]+f[34]$ | (A24) |
| $y'[25]$ | $Cl^-$ | 765 | $-f[66]-f[67]+f[32]$ | (A25) |
| $y'[26]$ | $SO_4^{2-}$ | 39.6 | $-f[82]-f[50]-f[68]-f[69]+f[31]$ | (A26) |
| $y'[27]$ | "reactive" $PO_4^{3-}$ | 0.003 | $-f[55]-f[62]-f[63]-f[64]-f[65]-f[53]+f[19]+f[61]$ | (A27) |
| *Seafloor basalt components —* | | | | |
| $y'[28]$ | Anorthite | 16907 | $-f[131]+f[41]+f[98]$ | (A28) |
| $y'[29]$ | Calcite | 326 | $-f[98]+f[94]$ | (A29) |
| $y'[30]$ | Pyrite-S | 209 | $-f[99]+f[82]$ | (A30) |
| $y'[31]$ | Apatite-P | 165 | $-f[97]+f[53]$ | (A31) |
| $y'[32]$ | Fe-II | 2310 | $-{}^{15}/_2\times f[82]+f[128]$ | (A32) |
| $y'[33]$ | Fe-III | 8252 | $-f[130]+f[129]$ | (A33) |

TABLE A3

*(continued)*

| **y'[*i*]** | **Reservoir component** | **$y[i]\|_{t \to \infty}$** | **Balance of fluxes ($y'[i] \sim 0\|_{t \to \infty}$)** | |
|---|---|---|---|---|
| *Pelagic sediments —* | | | | |
| y'[34] | Organic matter | 172 | $-f[108]+f[57]$ | (A34) |
| y'[35] | Calcite | 541 | $-f[103]-f[110]-f[111]+f[76]$ | (A35) |
| y'[36] | Apatite | 4.0 | $-f[107]+f[65]+f[63]+f[59]$ | (A36) |
| y'[37] | Fe-III | 20 | $-f[105]+f[51]$ | (A37) |
| *Clays —* | | | | |
| y'[38] | Na-montmorillonite | 107 | $-f[127]-f[123]+f[40]$ | (A38) |
| y'[39] | K-illite | 351 | $-f[124]+f[77]$ | (A39) |
| y'[40] | Mg-chlorite | 364 | $-f[45]-f[126]+f[79]$ | (A40) |

Vector of ODEs (y′[i]), absolute steady state mass values (yA[i], in $10^{18}$ mol), and constituent fluxes composing the overall model. Small differences in the balance of fluxes taken from table A1 reflect truncation not present in the internal model calculation.

## References

Alt, J. C., and Teagle, D. A. H., 1999, The uptake of $CO_2$ during alteration of ocean crust: Geochimica et Cosmochimica Acta, v. 63, p. 1527–1535.

Arvidson, R. S., and Mackenzie, F. T., 1997, Tentative kinetic model for dolomite precipitation rate: Aquatic Geochemistry, v. 2, p. 273–298.

——— 1999, The dolomite problem: control of precipitation kinetics by temperature and saturation state: American Journal of Science, v. 299, p. 257–288.

Arvidson, R. S., Mackenzie, F. T., and Guidry, M. W., 2000, Ocean/atmosphere history and carbonate precipitation rates: a solution to the "dolomite problem"?, *in* Glenn, C. R., Prévôt-Lucas, L., and Lucas, J., editors, Marine Authigenesis: From Global to Microbial: S.E.P.M. Special Publication No. 65, p. 1–5.

——— 2006, The control of Phanerozoic atmosphere and seawater composition by basalt–seawater exchange reactions: Journal of Geochemical Exploration, v. 88, p. 412–415.

Berner, R. A., 1991, A model for atmospheric $CO_2$ over Phanerozoic time: American Journal of Science, v. 291, p. 339–376.

——— 1994, GEOCARB II: a revised model of atmospheric $CO_2$ over Phanerozoic time: American Journal of Science, v. 294, p. 56–91.

——— 1998, The carbon cycle and $CO_2$ over Phanerozoic time: the role of land plants: Philosophical Transactions of the Royal Society of London, Series B, v. 353, p. 75–82.

——— 1999, A new look at the long term carbon cycle: GSA Today, v. 9, p. 1–6.

——— 2001, Modeling atmospheric oxygen over Phanerozoic time: Geochimica et Cosmochimica Acta, v. 65, p. 685–694.

——— 2004, The Phanerozoic carbon cycle: $CO_2$ and $O_2$: New York, Oxford University Press, 158 p.

Berner, R. A., and Canfield, D. E., 1989, A new model for atmospheric oxygen over Phanerozoic time: American Journal of Science, v. 289, p. 333–361.

Berner, R. A., and Kothavala, Z., 2001, GEOCARB III: a revised model of atmospheric $CO_2$ over Phanerozoic time: American Journal of Science, v. 301, p. 182–204.

Berner, R. A., Lasaga, A. C., and Garrels, R. M., 1983, The carbonate-silicate geochemical cycle and its effect on atmospheric carbon dioxide over the past 100 million years: American Journal of Science, v. 283, p. 641–683.

Berner, R. A., Petsch, S. T., Lake, J. A., Beerling, D. J., Popp, B. N., Lane, R. S., Laws, E. A., Westley, M. B., Cassar, N., Woodward, F. I., and Quick, W. P., 2000, Isotope fractionation and atmospheric oxygen: Implications for Phanerozoic $O_2$ evolution: Science, v. 287, p. 1630–1633.

Berner, R. A., Beerling, D. J., Dudley, R., Robinson, J. M., and Wildman, R. A., Jr., 2003, Phanerozoic atmospheric oxygen: Annual Review of Earth and Planetary Sciences, v. 31, p. 105–134.

Boss, S. K., and Wilkinson, B. H., 1991, Planktogenic/eustatic control of cratonic/oceanic carbonate accumulation: Journal of Geology, v. 99, p. 497–513.

Budyko, O. M. I., Ronov, A. B., and Yanshin, A. L., 1987, History of the Earth's Atmosphere, translated from Russian by Lemeshko, S. F., and Yanuta, V. G.: Berlin, Springer-Verlag, 139 p.

Canfield, D. E., 1991, Sulfate reduction in deep-sea sediments: American Journal of Science, v. 291, p. 177–188.

Compton, J. S., Mallinson, D. J., Glenn, C. R., Filippelli, G., Follmi, K., Shields, G., and Zanin, Y., 2000, Variations in the global phosphorus cycle, *in* Glenn, C. R., Prévôt-Lucas, L., and Lucas, J., editors, Marine Authigenesis: From global to microbial: Society of Sedimentary Geology, v. 66, p. 21–33.

Dickson, A. G., and Millero, F. J., 1987, A comparison of the equilibrium constants for the dissociation of carbonic acid in seawater media: Deep-Sea Research, v. 34, p. 1733–43.

Dickson, J. A. D., 2002, Fossil echinoderms as monitor of the Mg/Ca Ratio of Phanerozoic oceans: Science, v. 298, p. 1222–1224.

Drever, J. I., 1971, Magnesium-Iron replacement in clay minerals in anoxic marine sediments: Science, v. 172, p. 1334–1336.

Engebretson, D. C., Kelley, K. P., Cashman, H. J., and Richards, M. R., 1992, 180 Million years of subduction: GSA Today, v. 2, p. 93–95.

Gaffin, S., 1987, Ridge volume dependence on sea-floor generation rate and inversion using long-term sea-level change: American Journal of Science, v. 287, p. 596–611.

Garrels, R. M., 1965, Silica: Role in buffering of natural waters: Science, v. 148, p. 69.

Garrels, R. M., and Mackenzie, F. T., 1971, Evolution of Sedimentary Rocks: New York, W.W. Norton and Company, 397 p.

——— 1972, A quantitative model for the sedimentary rock cycle: Marine Chemistry, v. 1, p. 27–41.

Garrels, R. M., and Perry, E. A., Jr., 1974, Cycling of carbon, sulfur and oxygen through geologic time, *in* Goldberg, E. D., editor, The Sea: New York, Wiley-Interscience, v. 5, p. 303–316.

Given, R. K., and Wilkinson, B. H., 1987, Dolomite abundance and stratigraphic age-constraints on rates and mechanisms of dolomite formation: Journal of Sedimentary Petrology, v. 57, p. 1068–1078.

Gregor, C. B., Garrels, R. M., Mackenzie, F. T., and Maynard, J. B., 1988, Chemical Cycles in the Evolution of the Earth: New York, John Wiley and Sons, 276 p.

Guidry M. W., Arvidson, R. S., and Mackenzie, F. T., 2006, Carbonate-silicate biogeochemical cycle: Relevance to seawater, atmosphere and carbonate precipitate composition during the Phanerozoic, *in* Falkowski, P., and Knoll, A., editors, Evolution of Primary Producers of the Sea: San Diego, Academic Press.

Hansen, K. W., and Wallmann, K., 2003, Cretaceous and Cenozoic evolution of seawater composition, atmospheric $O_2$ and $CO_2$: A model perspective: American Journal of Science, v. 303, p. 94–148.

Hardie, L. A., 1996, Secular variations in seawater chemistry: An explanation for the coupled secular variation in the mineralogies of marine limestones and potash evaporites over the past 600 m.y.: Geology, v. 24, p. 279–283.

He, S., and Morse, J. W., 1993, The carbonic acid system and calcite solubility in aqueous Na-K-Ca-Mg-Cl-$SO_4$ solutions from 0 to 90°C: Geochimica et Cosmochimica Acta, v. 57, p. 3533–3555.

Holland, H. D., 1984, The geochemical evolution of atmosphere and oceans: Princeton, Princeton University Press, 582 p.

Holland, H. D., and Zimmerman, H., 2000, The dolomite problem revisited: International Geology Review, v. 42, p. 481–490.

Holser, W. T., 1984, Gradual and abrupt shifts in ocean chemistry during Phanerozoic time, *in* Holland, H. D., and Trendall, A. F., editors., Patterns of Change in Earth Evolution: Berlin, Dahlem Konferenzen, Springer-Verlag, p. 123–143.

Horita, J., Zimmermann, H., and Holland, H. D., 2002, Chemical evolution of seawater during the Phanerozoic – Implications from the record of marine evaporates: Geochimica et Cosmochimica Acta, v. 66, p. 3733–3756.

Hutcheon, I., Oldershaw, A., and Ghent, E. D., 1980, Diagenesis of Cretaceous sandstones of the Kootenay Formation at Elk Valley (southeastern British Columbia) and Mt. Allan (southwestern Alberta): Geochimica et Cosmochimica Acta, v. 44, p. 1425–35.

Lasaga, A. C., 1981, Dynamic treatment of geochemical cycles: Global Kinetics, *in* Lasaga, A. C., and Kirkpatrick, R. J., editors, Kinetics of Geochemical Processes: Mineralogical Society of America, Reviews in Mineralogy and Geochemistry, v. 8, p. 69–109.

Lasaga, A. C., Berner, R. A., and Garrels, R. M., 1985, An improved geochemical model of atmospheric $CO_2$ fluctuations over the past 100 million years, *in* Sundquist, E. T., and Broecker, W. S., editors, The Carbon Cycle and Atmospheric $CO_2$: Natural variations Archean to Present: American Geophysical Union, Geophysical Monograph, v. 32, p. 397–411.

Lécuyer, C., and Ricard, Y., 1999, Long-term fluxes and budget of ferric iron: implications for the redox state of Earth mantle and atmosphere: Earth and Planetary Science Letters, v. 165, p. 197–211.

Lowenstein, T. K., Timofeeff, M. N., Brennan, S. T., Hardie, L. A., and Demicco, R. V., 2001, Oscillations in Phanerozoic seawater chemistry: evidence from fluid inclusions: Science, v. 294, p. 1086–1088.

Lowenstein, T. K., Hardie, L. A., Timofeeff, M. N., and Demicco, R. V., 2003, Secular variation in seawater chemistry and the origin of calcium chloride basinal brines: Geology, v. 31, p. 857–860.

Mackenzie, F. T., 1992, Chemical mass balance between rivers and oceans: Encyclopedia of Earth System Science, v. 1: New York, Academic Press, p. 431–445.

Mackenzie, F. T., and Garrels, R. M., 1966a, Chemical mass balance between rivers and oceans: American Journal of Science, v. 264, p. 507–525.

——— 1966b, Silica-bicarbonate balance in the ocean and early diagenesis: Journal of Sedimentary Petrology, v. 36, p. 1075–1084.

Mackenzie, F. T., and Lerman, A., 2006, Carbon in the Geobiosphere—Earth's Outer Shell: Berlin, Springer, 325 p.

Mackenzie, F. T., and Morse, J. W., 1992, Sedimentary carbonates through Phanerozoic time: Geochimica et Cosmochimica Acta, v. 56, p. 3281–3295.

Mackenzie, F. T., and Pigott, J. D., 1981, Tectonic controls of Phanerozoic sedimentary rock cycling: Journal of the Geological Society, v. 138, p. 183–196.

Mackenzie, F. T., Ristvet, B. L., Thorsetenson, D. C., Lerman, A., and Leeper, R. H., 1981, Reverse weathering and chemical mass balance in a coastal environment, *in* Marten, J. M., Burton, J. D., and Eisma, D., editors, River Inputs to Ocean systems: Switzerland, UNEP and UNESCO, p. 152–187.

Martin, R. E., 1996, Secular increase in nutrient levels through the Phanerozoic: Implications for productivity, biomass, and diversity of the marine biosphere: Palaios, v. 11, p. 209–219.

Martin, W. R., and Sayles, F. L., 1994, Seafloor diagenetic fluxes: Material Fluxes on the Surface of the Earth, Board on Earth Sciences and Resources Commission on Geosciences, Environment, and Resources: National Resource Council, National Academy Press, p. 143–163.

Meybeck, M., 1979, Pathways of major elements from land to ocean through river: Rome, Food and Agricultural Organization of the United Nations, Review and Workshop on River Inputs to Ocean Systems, p. 18–30.

Michalopoulos, P., and Aller, R. C., 1995, Rapid clay mineral formation in Amazon delta sediments: reverse weathering and oceanic elemental cycles: Science, v. 270, p. 614–617.

Mottl, M. J., and Holland, H. D., 1978, Chemical exchange during hydrothermal alteration of basalt by seawater—I. Experimental results for major and minor components of seawater: Geochimica et Cosmochimica Acta, v. 42, p. 1103–1115.

Pearson, P. N., and Palmer, M. R., 2000, Atmospheric carbon dioxide concentrations over the past 60 million years: Nature, v. 406, p. 695–699.

Pitzer, K. S., 1973, Thermodynamics of electrolytes - I. Theoretical basis and general equations: Journal of Physical Chemistry, v. 77, p. 268–277.

Retallack, G. J., 2001, A 300-million-year record of atmospheric carbon dioxide from fossil plant cuticles: Nature, v. 411, p. 287–290.

Ronov, A. B., 1982, The Earth's Sedimentary Shell: Quantitative patterns of its structure, compositions, and evolution: The 20th Vernadskiy Lecture v. I, *in* Yaroshevskiy, A. A., editor, The Earth's Sedimentary Shell: Moscow, Nauka, p. 1–80; also, American Geological Institute Reprint Series, v. 5, p. 1–73.

Rothman, D. H., 2001, Global biodiversity and the ancient carbon cycle: Proceedings of the National Academy of Sciences, v. 98, p. 4305–4310.

——— 2002, Atmospheric carbon dioxide levels for the last 500 millions years: Proceedings of the National Academy of Sciences, v. 99, p. 4167–4171.

Rowley, D., 2002, Rate of plate creation and destruction: 180 Ma to present: GSA Bulletin, v. 114, p. 927–933.

Russell, K. L., 1970, Geochemistry and halmyrolysis of clay minerals, Rio Ameca, Mexico: Geochimica et Cosmochimica Acta, v. 34, p. 893–907.

Schrag, D., 2002, Control of atmospheric $CO_2$ and climate through Earth history: Goldschmidt Conference Abstracts, p. A688.

Shaviv, N. J., and Veizer, J., 2003, Celestial driver of Phanerozoic climate?: GSA Today, v. 13, p. 4–10.

Smith, S. V., and Hollibaugh, J. T., 1997, Annual cycle and interannual variability of ecosystem metabolism in a temperate climate embayment: Ecological Monographs, v. 67, p. 509–533.

Smith, S. V., and Mackenzie, F. T., 1987, The ocean as a net heterotrophic system: Implications from the carbon biogeochemical cycle: Global Biogeochemical Cycles, v. 1, p. 187–198.

Stanley, S. M., and Hardie, L. A., 1998, Secular oscillations in the carbonate mineralogy of reef-building and sediment-producing organisms driven by tectonically forced shifts in seawater chemistry: Palaeogeography, Palaeoclimatology, and Palaeoecology, v. 144, p. 3–19.

——— 1999, Hypercalcification: paleontology links plate tectonics and geochemistry to sedimentology: GSA Today, v. 9, p. 2–7.

Stoffyn-Egli, P., 1982, Dissolved aluminum in interstitial waters of recent terrigenous marine sediments from the North Atlantic Ocean: Geochimica et Cosmochimica Acta, v. 46, p. 1345–1352.

Tyrrell, T., 1999, The relative influence of nitrogen and phosphorus on oceanic primary production: Nature, v. 400, p. 525–531.

Tyrrell, T., and Zeebe, R. E., 2004, History of carbonate ion concentration over the last 100 million years: Geochimica et Cosmochimica Acta, v. 68, p. 3521–3530.

Van Cappellen, P., and Ingall, E. D., 1996, Redox stabilization of the atmosphere and oceans by phosphorous-limited marine productivity: Science, v. 271, p. 493–496.

Veizer, J., Goddéris, Y., and Francois, L. M., 2000, Evidence for decoupling of atmospheric $CO_2$ and global climate during the Phanerozoic eon: Nature, v. 408, p. 698–701.

Volk, T., 1989, Sensitivity of climate and atmospheric $CO_2$ to deep-ocean and shallow-ocean carbonate burial: Nature, v. 337, p. 637–640.

Walker, L. J., Wilkinson, B. H., and Ivany, L. C., 2002, Continental drift and Phanerozoic carbonate accumulation in shallow-shelf and deep-marine settings: Journal of Geology, v. 110, p. 75–87.

Wallmann, K., 2001, Controls on the Cretaceous and Cenozoic evolution of seawater composition, atmospheric $CO_2$ and climate: Geochimica et Cosmochimica Acta, v. 65, p. 3005–3025.

Wilkinson, B. H., and Walker, J. C. G., 1989, Phanerozoic cycling of sedimentary carbonate: American Journal of Science, v. 289, p. 525–548.

Wollast, R., and Mackenzie, F. T., 1983, The global cycle of silica, *in* Ashton, S. R., editor, Silicon Geochemistry and Biogeochemistry: New York, Academic Press, p. 39–76.

Veizer, J., and Mackenzie, F. T., 2004, Evolution of sedimentary rocks, *in* Mackenzie, F. T., editor, Sediments, Diagenesis, and Sedimentary Rocks: Oxford, Elsevier-Pergamon, Treatise on Geochemistry, v. 7, p. 369–407.

Yapp, C. J., and Poths, H., 1992, Ancient atmospheric $CO_2$ pressures inferred from natural goethites: Nature, v. 355, p. 342–244.

Zeebe, R. E., 2001, Seawater pH and isotopic paleotemperatures of Cretaceous oceans: Palaeogeography, Palaeoclimatology, Palaeoecology, v. 170, p. 49–57.